425

RTIASI-4, a new version of the ECMWF fast radiative transfer model for the infrared atmospheric sounding interferometer

Marco Matricardi

Research Department

October 2003

Series: ECMWF Technical Memoranda

A full list of ECMWF Publications can be found on our web site under:
http://www.ecmwf.int/publications/

Contact: library@ecmwf.int

European Centre for Medium Range Weather Forecasts
Shinfield Park, Reading, RG2 9AX, England

Abstract

An improved version of RTIASI, the ECMWF fast radiative transfer model for the Infrared Atmospheric Sounding Interferometer, has been developed. In the new version of RTIASI (RTIASI-4) the accuracy of the fast transmittance model has been improved by including 4 more molecules (HNO3, CCl4, CF4 and OCS) in the line-by-line computations and by using the year 2000 release of the HITRAN molecular database. By using a revised set of water vapour training profiles in the stratosphere, the condition of the regression has been improved so that unphysical oscillations observed in the stratospheric water vapour Jacobians have been virtually eliminated. RTIASI-4 features a revised vertical pressure grid that allows the integration of the radiative transfer equation to be performed with significantly increased accuracy. The water vapour transmittance model has been significantly improved by weighting the data prior to performing the regression and by introducing a dedicated transmittance model for the continuum absorption. Minor adjustments to the predictors for water vapour have also been made. A significant improvement to the previous versions of the model is the inclusion of CO, CH_4, N_2O and CO_2 as profile variables. Finally, a solar term has been introduced to evaluate the solar radiance reflected by a land or water surface in a non-scattering atmosphere.

1. Introduction

Radiances from the Advanced TIROS Operational Vertical Sounder (ATOVS) on the National Oceanic and Atmospheric Administration (NOAA) polar orbiting satellites are used at the European Centre for Medium-Range Weather Forecasts (ECMWF) by assimilation the radiances directly into the four-dimensional variational analysis scheme, 4-DVAR (Rabier et. al. 1998). A potentially useful addition to the current satellite sounders is the Infrared Atmospheric Sounding Interferometer (IASI) (Cayla 1993). In combination with the Advanced Microwave Sounding Unit (AMSU-A), the Microwave Humidity Sounder (MHS), and the Advanced Very High Resolution Radiometer (AVHRR/3), IASI is the core payload of the European Organisation for Exploitation of Meteorological Satellites (EUMETSAT) Meteorological Operational Satellite (METOP-1) (Klaes et al. 2000) and will contribute to the primary mission objective of METOP-1 that is the measurement of meteorological parameters for NWP and climate models.

A prerequisite for exploiting radiances from conventional and high-resolution sounders is the availability of a fast radiative transfer model (usually called the observation operator) to predict a first guess radiance from the model fields (temperature, water vapour, ozone, surface emissivity and perhaps clouds in the future).

As part of the preparations being made at ECMWF to exploit the IASI datasets, RTIASI, the ECMWF fast radiative transfer model for IASI, has been developed (Matricardi and Saunders, 1999). The original version of RTIASI has undergone a number of significant upgrades that has led to the release of a number of different versions of the model. The scope of this paper is to illustrate the work undertaken at ECMWF to develop the most recent versions of RTIASI, RTIASI-4.

In RTIASI-4 the number of gases included in the line-by-line computations has been increased to include HNO_3, CCL_4, OCS and CF_4. A sensitivity study has shown that the inclusion of these gas species gives rise to brightness temperature differences that in some regions of the spectrum can exceed the instrument noise. The database of line-by-line transmittances has been generated using the year 2000 version of the HITRAN molecular database (Rothman et al., 1998). This new version of HITRAN features an extensive updating of the water vapour and methane lines.

Radiance calculations in the previous versions of RTIASI were performed assuming that the atmosphere is divided into 43 layers of fixed pressure levels. To reduce the errors that are introduced in the radiative transfer calculations by limiting the number of layers to 43, RTIASI-4 uses a vertical pressure grid with increased number of levels. The new grid is made of 90 levels that extend from 1050 hPa to 0.005 hPa. The definition of the new grid is the result of sensitivity calculations performed to ensure that the optimum number of layers is being used for the desired accuracy and speed of computation.

To eliminate discontinuities in the water vapour Jacobians, the split algorithm used in the older versions of the code to model the water vapour absorption has been replaced in RTIASI-4 by a single algorithm with the data being weighted prior to performing the regression.

For the prediction of the water continuum absorption, a new scheme has been introduced in RTIASI-4 where the water continuum is handled separately from the other gases. A fast model for the water continuum has been developed based on a database of monochromatic transmittances generated using a water continuum model (CKD 2.4) (Clough et al, 1989). The advantage of having a separate fast model for the continuum is that any change in the continuum coefficients can be addressed without the need of generating a new line-by-line database.

A significant improvement to the previous versions of the model is the inclusion in RTIASI-4 of CO, CH_4, N_2O and CO_2 as profile variables.

Finally, RTIASI-4 features the inclusion of a solar term to evaluate the solar radiance reflected by a land or water surface in a non-scattering atmosphere.

2. The formulation of the fast radiative transfer model

The basic methods that were applied to develop RTIASI have been documented in Matricardi and Saunders (1999). In this section only the main components are discussed. Any major change to the model is documented in detail in the next sections.

RTIASI-4 contains a fast model of the transmittances of the atmospheric gases generated from accurate line-by-line (LBL) transmittances for a set of diverse atmospheric profiles over the IASI wave-number range. The monochromatic transmittances are convolved with the appropriate IASI spectral response function (ISRF) and are used to compute channel-specific regression coefficients by use of a selected set of predictors. These regression coefficients can then be used by the fast transmittance model to compute transmittances given any other input profile. This parameterization of the transmittances makes the model computationally efficient and in principle should not add significantly to the errors generated by uncertainties in the spectroscopic data used by the LBL model. Note that the ISRF used in RTIASI-4 is defined as the convolution of a 0.5 cm^{-1} full width at half-height (FWHH) Gaussian with a cardinal sine whose interferogram is a ± 1.96856- cm box function (level 1C spectrum).

In the RTIASI-4 fast transmittance model the computation of the optical depth for the layer from pressure level j to space along a path at angle θ involves a polynomial with terms that are functions of temperature, absorber amount, pressure, and viewing angle. The convolved optical depth at wave-number $\tilde{\nu}^*$ ($\tilde{\nu}^*$ is the central wave number of the IASI channel and the circumflex over the symbol denotes convolution) from level j to space can be written as:

$$\hat{\rho}_{j,\tilde{\nu}^*} = 0 \qquad j=1 \qquad (1)$$

$$\hat{\rho}_{j,\tilde{\nu}^*} = \hat{\rho}_{j-1,\tilde{\nu}^*} + \sum_{k=1}^{M} a_{j-1,\tilde{\nu}^*,k} X_{k,j-1} \qquad \text{j=2,90} \tag{2}$$

where M is the number of predictors and the functions $X_{k,j}$ constitute the profile-dependent predictors of the fast transmittance model. To compute the expansion coefficients $a_{j,\tilde{\nu}^*,k}$ (sometimes referred to as fast transmittance coefficients), one can use a set of diverse atmospheric profiles to compute, for each profile and for several viewing angles, accurate LBL level-to-space transmittances for each level defined by an atmospheric pressure layer grid. For each gas allowed to vary, the profiles used to compute the database of LBL transmittances are chosen to represent the range of variations in temperature and absorber amount found in the real atmosphere. For j>1 (note that $\tau_{1,\tilde{\nu}^*} = 1$) the convolved LBL level-to-space transmittances $\tau_{j,\tilde{\nu}^*}$ are used to compute the $a_{j-1,\tilde{\nu}^*,k}$ coefficients by linear regression of

$$\hat{\rho}_{j,\tilde{\nu}^*} - \hat{\rho}_{j-1,\tilde{\nu}^*} \tag{3}$$

or equivalently

$$-\ln[\hat{\tau}_{j,\tilde{\nu}^*} / \hat{\tau}_{j-1,\tilde{\nu}^*}]) \tag{4}$$

versus the predictor values $X_{k,j-1}$ calculated from the profile variables for each profile at each viewing angle. Regression coefficients are generated for H_2O, CO_2, O_3, N_2O, CO, CH_4 and for the so-called fixed gases and are used to compute the model transmittances $\hat{\tau}^{F\,model}_{j,\tilde{\nu}^*}$, $\hat{\tau}^{WV\,model}_{j,\tilde{\nu}^*}$, $\hat{\tau}^{O_3\,model}_{j,\tilde{\nu}^*}$, $\hat{\tau}^{CO_2\,model}_{j,\tilde{\nu}^*}$, $\hat{\tau}^{N_2O\,model}_{j,\tilde{\nu}^*}$, $\hat{\tau}^{CO\,model}_{j,\tilde{\nu}^*}$ and $\hat{\tau}^{CH_4\,model}_{j,\tilde{\nu}^*}$. The total model transmittance is then written as

$$\hat{\tau}^{T\,model}_{j,\tilde{\nu}^*} = \hat{\tau}^{F\,model}_{j,\tilde{\nu}^*} \hat{\tau}^{WV\,model}_{j,\tilde{\nu}^*} \hat{\tau}^{O_3\,model}_{j,\tilde{\nu}^*} \hat{\tau}^{CO_2\,model}_{j,\tilde{\nu}^*} \hat{\tau}^{N_2O\,model}_{j,\tilde{\nu}^*} \hat{\tau}^{CO}_{j,\tilde{\nu}^*} \hat{\tau}^{CH_4\,model}_{j,\tilde{\nu}^*} \tag{5}$$

Gases are considered as fixed if their spatial and temporal concentration variations do not contribute significantly to the observed radiance. In RTIASI-4 we define fixed gases as N_2, O_2, HNO_3, OCS, CCl_4, CF_4, CCl_3F (CFC-11) and CCl_2F_2 (CFC-12). The convolved level-to-space transmittances predicted by the fast model are used to estimate the radiance as viewed by the IASI assuming that the convolution of the monochromatic radiances can be approximated by the radiance computed using the convolved transmittances (polychromatic approximation). The accuracy of the polychromatic approximation was tested for a wide range of atmospheric profiles. The errors were found to be typically less than 0.12 K. Since the error introduced by the polychromatic approximation is less than the radiometric noise it was considered to be adequate for our purposes. The radiance calculation is performed assuming that the atmosphere is subdivided into M homogeneous layers of fixed pressure (the atmospheric layers are numbered from 1 (the layer bounded by pressure levels 1 and 2), to the first layer above the surface, layer M). The current formulation of RTIASI-4 assumes that, for a plane-parallel atmosphere in local thermodynamic equilibrium with no scattering, the upwelling radiance at the top of the atmosphere can be written as:

$$\hat{L}(\tilde{\nu}^*,\theta) = (1-N)\hat{L}^{Clr}(\tilde{\nu}^*,\theta) + N\hat{L}^{Cld}(\tilde{\nu}^*,\theta) \tag{6}$$

where $\hat{L}^{Clr}(\tilde{\nu}^*,\theta)$ and $\hat{L}^{Cld}(\tilde{\nu}^*,\theta)$ are the clear-column and overcast radiances at wave number $\tilde{\nu}^*$ and zenith angle θ and N is the fractional cloud cover, assumed here to be in a single layer with unit emissivity. If we assume specular reflection at the Earth's surface and ignore the contribution of solar radiation reflected by the surface, the clear-column radiance for a single viewing angle can be written as:

$$\hat{L}^{Clr}_{\tilde{v}^*} = \hat{\tau}_{s,\tilde{v}^*}\varepsilon_{s,\tilde{v}^*}B_{\tilde{v}^*}(T_s) + (\sum_{l=1}^{M}\hat{L}^{u}_{l,\tilde{v}^*}) + (1-\varepsilon_{s,\tilde{v}^*})[\sum_{l=1}^{M}\hat{L}^{u}_{l,\tilde{v}^*}\hat{\tau}^{2}_{s,\tilde{v}^*}/(\hat{\tau}_{l+1,\tilde{v}^*}\hat{\tau}_{l,\tilde{v}^*})] + \hat{L}^{l}_{\tilde{v}^*} \tag{7}$$

where $\hat{\tau}_{l,\tilde{v}^*}$ is the convolved transmittance from a given pressure level p_l to space, $\varepsilon_{s,\tilde{v}^*}$ is the surface emissivity and the subscript s refers to the surface. Here $\hat{L}^{u}_{j,\tilde{v}^*}$ is defined as:

$$\hat{L}^{u}_{l,\tilde{v}^*} = B_{\tilde{v}^*}(T_l)(\hat{\tau}_{l,\tilde{v}^*} - \hat{\tau}_{l+1,\tilde{v}^*}) \tag{8}$$

where $\hat{L}^{l}_{\tilde{v}^*}$ is a small atmospheric contribution from the surface to the first layer above the surface M. The first term on the right-hand side of Eq. (7) is the radiance from the surface, the second term is the radiance emitted from the atmosphere and the third term is the downwelling thermal radiance reflected from the surface. Note that in deriving Eq. (7) we implicitly assume that the total transmittance of an atmospheric path is the product of the transmittances of the constituent sub-paths. Although this is true for monochromatic radiation it can be considered a good approximation when the transmittance varies relatively slowly with wave number (note that the IASI ISRF is narrow and is essentially symmetric about its centroid). The scene temperature T_l is defined here as the layer mean temperature that was obtained by averaging the temperature at the top and the bottom of the layer.

For the sea surface emissivity $\varepsilon_{s,\tilde{v}^*}$ we developed a module to compute fast infrared emissivities over water for each IASI channel. Surface wind speed and zenith angle are used as predictors to compute channel specific regression coefficients by an analytical fit of the emissivities computed using the model by Masuda et. al. (1988). Two sets of regression coefficients have been generated that can be used to compute emissivities over fresh and salt water. The fit of the emissivity to the wind speed and the zenith angle is of the form:

$$\varepsilon_{s,\tilde{v}^*}(\theta) = A + (B - A)\exp((C_7 - 60)^2 - (\theta - C_7)^2)/(C_8 + C_9 w)) \tag{9}$$

where $\varepsilon_{s,\tilde{v}^*}(\theta)$ is the emissivity, w is the wind speed, θ is the zenith angle and

$$A = C_1 + C_2 w + C_3 w^2 \tag{10}$$

$$B = C_4 + C_5 w + C_6 w^2 \tag{11}$$

The coefficients C1, C2, C3 are obtained from a quadratic fit of the emissivities to the wind at 0 degrees whereas C4, C5, C6 are obtained from a quadratic fit of the emissivities at 60 degrees. The coefficients C7, C8, C9 are obtained from the non-linear fit of the emissivity to the wind speed and the zenith angle. The root-mean-square (rms) of the difference between exact and fast model emissivities ranges from 0.000055 to 0.00011.

For a cloud-top at standard pressure level J the top of atmosphere overcast cloudy radiance in discrete notation is defined as:

$$\hat{L}^{Cld}_{J,\tilde{v}^*} = \hat{\tau}_{Cld,\tilde{v}^*}B_{\tilde{v}^*}(T_{Cld}) + \sum_{j=1}^{J}\hat{L}^{u}_{j,\tilde{v}^*} \tag{12}$$

where $\hat{\tau}_{Cld,\tilde{v}^*}$ is the cloud-top to space transmittance and T_{Cld} the cloud-top temperature. Note that the emissivity of the cloud top is assumed to be unity, which is a tolerable assumption for optically thick water cloud at infrared radiances. If the cloud-top pressure p_c lies between standard pressure levels *J* and *J-1* then the overcast radiance at p_c is obtained by linear interpolation:

$$\hat{L}^{Cld}_{\tilde{\nu}^*} = \hat{L}^{Cld}_{J,\tilde{\nu}^*}(1-f_c) + \hat{L}^{Cld}_{J-1,\tilde{\nu}^*} f_c \tag{13}$$

where $f_c = (p_J - p_c) / (p_J - p_{J-1})$. In RTIASI-4 the radiative transfer equation is integrated on the same levels as the transmittance computations although in principle this is not necessary. The atmosphere is divided into 89 layers whose boundaries are the fixed pressure levels listed in Table 1. An interpolation/extrapolation is required to obtain the surface transmittance. In particular if the surface pressure p_s lies between standard pressure levels *J* and *J-1*, the optical depth at the surface, $\hat{\rho}_{s,\tilde{\nu}^*}$, is obtained by linear interpolation:

$$\hat{\rho}_{s,\tilde{\nu}^*} = \hat{\rho}_{J,\tilde{\nu}^*} + f_s(\hat{\rho}_{J-1,\tilde{\nu}^*} - \hat{\rho}_{J,\tilde{\nu}^*}) \tag{14}$$

where $f_s = (p_J - p_s) / (p_J - p_{J-1})$. If the surface pressure is greater than the pressure of all the fixed levels, J is set to the last fixed level and is extrapolated using Eq. 14.

Finally an empirical correction to the transmittance is possible by raising the computed transmittance to the power γ where γ is determined empirically. In RTIASI-4 γ is set equal to 1.

Level	Pressure	Level	Pressure	Level	Pressure	Level	Pressure
1	0.004985	24	4.665232	47	111.59828	70	478.53991
2	0.008217	25	5.661819	48	122.04000	71	499.53915
3	0.013544	26	6.949999	49	132.49238	72	521.46014
4	0.022327	27	8.489492	50	143.83996	73	543.05297
5	0.036803	28	10.36999	51	155.42814	74	565.53997
6	0.060665	29	12.39272	52	167.94999	75	587.63824
7	0.092000	30	14.81000	53	180.67306	76	610.59997
8	0.130497	31	17.38171	54	194.35997	77	638.6005
9	0.170293	32	20.39999	55	208.16008	78	667.70817
10	0.222228	33	23.58185	56	222.94002	79	696.97015
11	0.289999	34	27.26000	57	237.82787	80	727.43557
12	0.360172	35	31.11273	58	253.71002	81	759.15569
13	0.447325	36	35.50999	59	269.65405	82	792.18394
14	0.558831	37	40.10295	60	286.60000	83	826.57600
15	0.698133	38	45.29000	61	303.54892	84	862.38997
16	0.872159	39	50.68828	62	321.49993	85	899.68638
17	1.089564	40	56.73001	63	339.39209	86	938.52836
18	1.361163	41	63.00314	64	358.27996	87	978.98172
19	1.659991	42	69.96998	65	377.05325	88	1007.1150
20	2.061283	43	77.20131	66	396.80999	89	1021.1150
21	2.512501	44	85.17998	67	416.39657	90	1050.0000
22	3.109479	45	93.23421	68	436.94998		
23	3.783893	46	102.05001	69	457.27246		

Table 1: Fixed pressure levels (in hPa)

3. Update of the molecular database

Regression coefficients in RTIASI-4 are generated from a database of LBL transmittances computed using the GENLN2 model (Edwards, 1994). In principle fast radiative transfer models should not add significantly to the errors generated by uncertainties in the spectroscopic data used by the LBL model so that these errors make most of the contribution to the total error. Although in principle differences due to different LBL model mechanics should be considered, the accuracy of the LBL computations is largely based on the quality of the spectroscopic database used by the model (Rizzi et al., 2001, Tjemkes et al., 2002). Improved water vapour spectroscopic parameters are particularly needed across the whole vibro-rotational band of water vapour.

In RTIASI-4 the molecular parameters for the LBL computations are taken from the year 2000 release of the HITRAN database. A major difference to the year 1996 release (Rothman et al., 1998) used in RTIASI-2 is the total replacement for all water vapour and methane lines. These lines have been extensively updated. In particular for methane there is a fourfold increase in the number of lines from the previous version of HITRAN. To assess the impact of the new molecular database on LBL computations, GENLN2 spectra were computed for the USAFGL mid-latitude summer profile using the old and new version of the database. Results are shown in Fig. 1 where the difference between IASI level 1C simulated spectra is plotted.

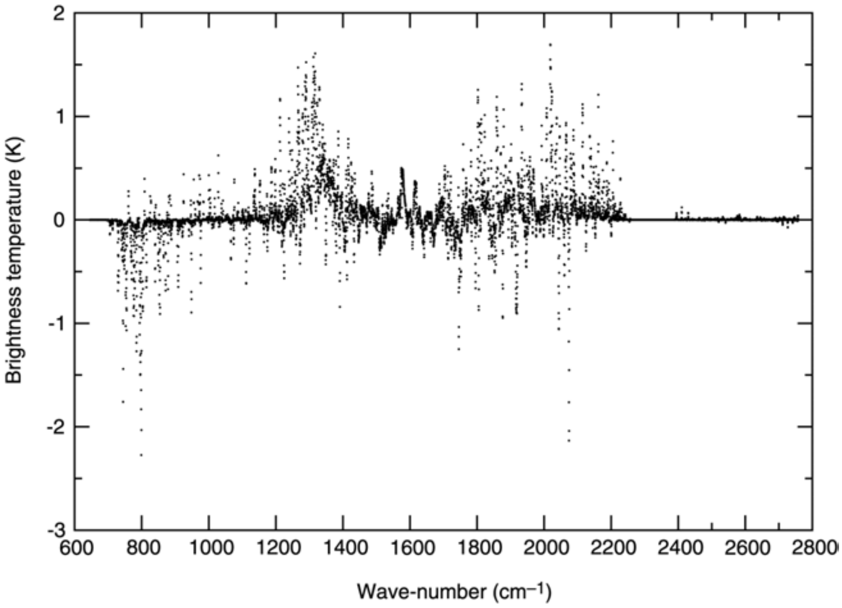

Figure 1. Difference between GENLN2 simulated IASI level 1C spectra obtained by using two different version of the HITRAN molecular database for the USAFGL mid-latitude summer profile.

In some spectral regions the signal resulting from the use of the updated molecular database is well above the instrument noise (see figure 2) and much larger than the typical errors associated to the parameterization of the transmittances in the fast model.

The impact of the revised water vapour parameters has also been tested (see Rizzi et al., 2001) by comparing measured spectra with computed spectra. Results indicate that the use of the new database makes simulations significantly closer to measurements.

4. Change to the number of molecules used in the line-by-line computations

In RTIASI-4 we define fixed gases as N_2, O_2, HNO_3, OCS, CCl_4, CF_4, CCl_3F and CCl_2F_2 (see section 2). Among these species, HNO_3, OCS, CCl_4, and CF_4 were not featured in the previous version of the model (RTIASI-2). Although in principle one might include all the HITRAN gases in the LBL computations, it has to be borne in mind that the execution time of GENLN2 poses limitations to the number of molecules that can be modeled. The inclusion of four more absorbers in the LBL computations is the result of a study where the impact of unmodelled absorbers on IASI level 1C radiances was evaluated.

A reference GENLN2 spectrum was computed for the USAFGL standard atmosphere when absorption from all the gas species featured in the HITRAN compilation is modeled (for OCS, CF_4 and CCl_4 more realistic profiles than the USAFGL ones were used). A number of test spectra were then generated by excluding in turn each of the absorbers modeled in the reference spectrum (note that CO_2, N_2O, CH_4, N_2, O_2, CCl_3F and CCl_2F_2 have not been considered since these absorbers are already modeled in RTIASI-2). After convolving the spectra with the IASI level 1C ISRF, variations in brightness temperature on exclusion of absorbing species were computed. Results are shown in Fig.2 where the difference between test and reference spectrum for each IASI channel is plotted along with the IASI level 1C Noise Equivalent Delta Temperature (NEdT) computed at a scene temperature taken to be equal to the simulated channel brightness temperature (here we show results only for those molecular species whose impact on the radiances is not negligible). Figure 2 evidences that only for a limited number of absorbers is the impact on simulated radiances above the noise level. For OCS and CCl_4 this happens for a large portion of the absorption band whereas for HNO_3 and CF_4 only a limited number of channels are to be considered. Thus we can assume the most basic set of absorbers to be considered in the LBL computations is made of 14 gases (H_2O, CO_2, O_3, N_2O, CO, CH_4, O_2, HNO_3, OCS, N_2, CCl_3F, CCl_2F_2, CF_4, CCl_4).

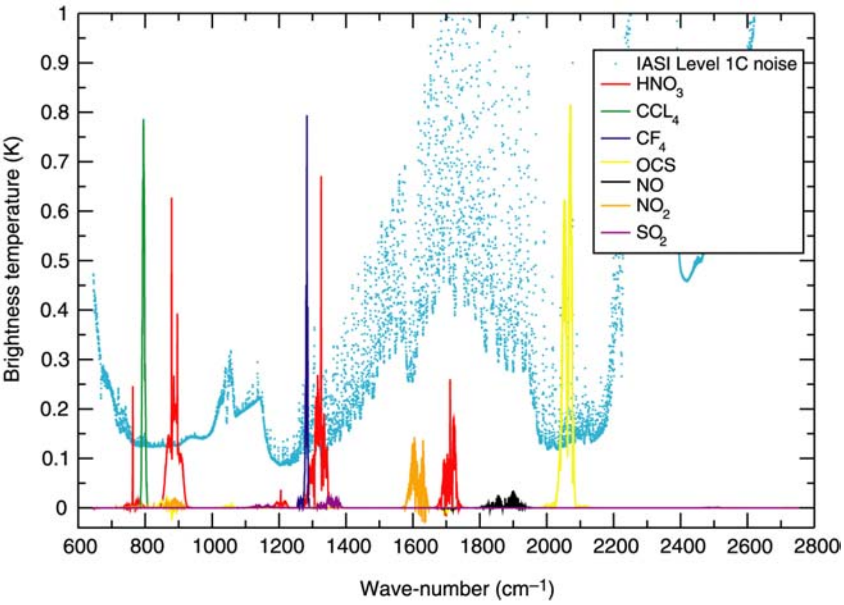

Figure 2. Impact of unmodelled absorbers on IASI Level 1C radiances

5. Revision of the training profiles for water vapour in the stratosphere

In RTIASI-2 the water vapour regression coefficients are generated by use of a training set of 42 profiles selected from the 1761 profile TOVS Initial Guess retrieval (TIGR) dataset (Matricardi and Saunders, 1999).

Since the quality of the radiosonde stratospheric humidity measurements in the TIGR dataset is a matter of concern, for each of the 42 TIGR water vapour profiles the specific humidity was extrapolated with a cubic law in pressure from 300 to 100 hPa. From 100 hPa to 0.005 hPa a number of profiles from the Halogen Occultation Experiment (HALOE) were used to provide some kind of variability to the stratospheric water vapour.

The choice of conditioning the regression in the stratosphere using a limited number of water vapour profiles was considered to be adequate since absorption from water vapour is very weak in that region. However, analysis of water Jacobians from RTIASI-2 show the occurrence of unphysical oscillations in the region above 100 hPa for some of the channels with very high peaking weighting functions. In an effort to improve the quality of water vapour Jacobians in the stratosphere, RTIASI-4 features a revised set of water vapour training profiles. The numerical conditioning of the regression in the stratosphere has in fact been improved by replacing the current stratospheric water vapour profiles with a much wider profile set from HALOE.

Each of the original 42 TIGR water vapour profiles is now joined at 100 hPa to the nearest (in terms of season and latitude) stratospheric profile chosen among those shown in the left panel of Fig.3. Also shown in Fig.3 (right panel) are the stratospheric profiles used in RTIASI-2. Figure 3 illustrates well the enhanced variability associated with the new profile set as well as the wider range of variation.

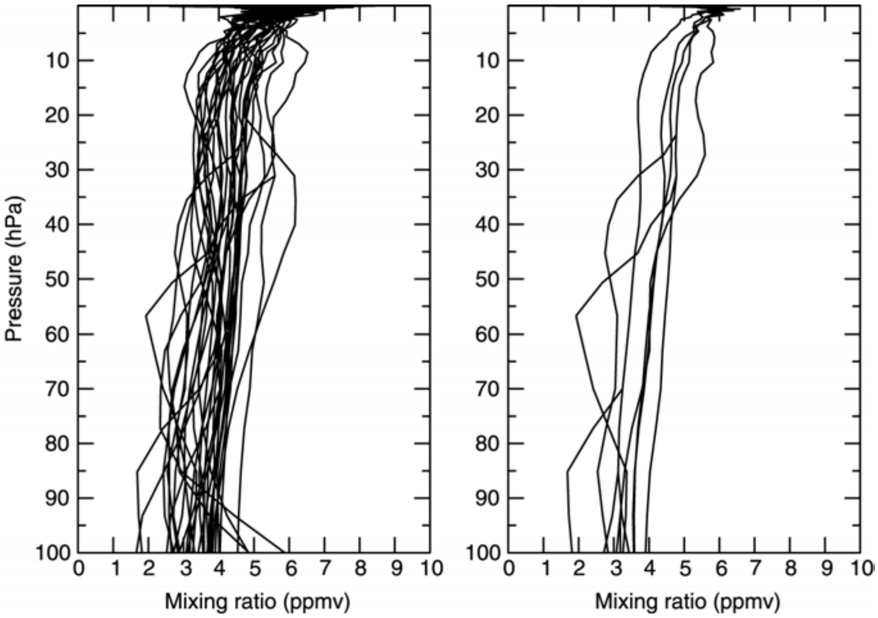

Figure 3 Stratospheric water vapour profiles used in (left panel) RTIASI-4 and (right panel) RTIASI-2.

6. Weighting of the input data prior to the regression

The scheme used in RTIASI-2 to model the behaviour of the water vapour layer optical depth involves a split algorithm. Two sets of regression coefficients are computed to model the absorption in the optically thin and optically thick regimes. The use of the split algorithm means that a running sum must be maintained in the fast transmittance model to use the appropriate regression coefficients (see Matricardi and Saunders, 1999). This can result in discontinuities in the water vapour Jacobians and a relatively poor prediction of the water vapour layer optical depth. To eliminate this problem, a single algorithm for water vapour has been introduced in RTIASI-4 with the data being weighted prior to performing the regression. In fact, since the radiance coming either from the layers where no attenuation is taking place or from the layers where the transmittance has become very small contributes little to the total radiance, not all the data are of equal importance for the regression. To improve the accuracy of the regression it would be desirable to have the computation of the regression coefficients not to be influenced by data corresponding to optically thick situations since they exhibit a behavior that is more complex to model than the one for the optically thin case. The accuracy of the prediction of the optical depths corresponding to optically thick situations is in fact of secondary importance since the contribution they make to the top of atmosphere radiance is negligible. Consequently, in RTIASI-4 input data to the regression are weighted in terms of the effective contribution to the total radiance with the weighting function chosen to be equal to $\hat{\tau}_{l,\tilde{\nu}^*} - \hat{\tau}_{l+1,\tilde{\nu}^*}$ (it can be seen from Eq. 8 that the emission from a single layer is proportional to $\hat{\tau}_{l,\tilde{\nu}^*} - \hat{\tau}_{l+1,\tilde{\nu}^*}$). This will result in smaller weights for situations where either no attenuation is taking place or the transmittance is very small and larger weights for situations where the emission from the layer is more significant.

7. A new scheme for prediction of water vapour continuum

For water vapour the continuum type absorption is of particular importance. The self-continuum contributes to absorption for most of the IASI channels and is predominant in the window regions. It displays a dependence on the inverse of the temperature and is proportional to the square of water amount. The foreign-continuum is only important at wave numbers greater than 1250 cm^{-1}. It displays a weaker dependence on temperature than the self-continuum and is linearly proportional to the water amount. In RTIASI-2 the continuum type absorption for H_2O was included in the LBL computations but no predictors of the type described above were included in the water vapour model.

In RTIASI-4 the regression for the water continuum is handled separately from the other gases. A fast model for the far wing water continuum has been developed based on a database of transmittances generated using a water continuum model. The advantage of having a separate fast model for the continuum is that any change in the continuum coefficients can be addressed without the need of generating a new LBL database. A considerable amount of time and disk space can then be saved. It also allows the reduction of the number of predictors used in the water vapour model helping improving the accuracy of the regression since the interaction of some of the predictors can cause numerical instabilities in the results of the regression.

The fast model for the water continuum introduced in RTIASI-4 is based on the general methods described in section 2. A database of model transmittances was created and regression coefficients generated by linear regression of the model transmittances versus the predictor values calculated from the profile variables. A feature of the continuum type absorption is that the variation with frequency is very slow when compared to the IASI spectral response function. It can then be considered constant over a channel and therefore the convolved transmittance can be replaced by the monochromatic continuum transmittance. The database of monochromatic transmittances was created using the most recent release (version 2.4) of the so-called CKD continuum model (Clough et al, 1989). This is a change to the continuum model used in RTIASI-2 (CKD 2.1). The CKD 2.4 self-broadening coefficients are identical to the CKD 2.1 coefficients whereas the foreign-broadening coefficients in CKD 2.4 are greater than CKD 2.1 from 600 to about 800 cm^{-1} and significantly smaller between 1860 and 2160 cm^{-1}. Based on the expected behaviour of the water continuum described above, prediction of the continuum optical depths is performed by using a total of four predictors (see table 2 for predictors and table 8 for the definition of the variables). Predictors $X_{j,1}$ and $X_{j,2}$ are used to model the self-continuum absorption whereas predictors $X_{j,3}$ and $X_{j,4}$ are used to model the foreign-continuum absorption. The accuracy of the continuum model will be discussed in detail later, but here we can anticipate that the fit to the GENLN2 radiances has been significantly improved compared to the results obtained for RTIASI-2.

$X_{j,1}$	$sec(\theta)\frac{W_r^2}{T_r}$
$X_{j,2}$	$sec(\theta)\frac{W_r^2}{T_r^4}$
$X_{j,3}$	$sec(\theta)\frac{W_r}{T_r}$
$X_{j,4}$	$sec(\theta)\frac{W_r}{T_r^2}$

Table 2. Predictors used in RTIASI-4 for water vapour continuum

8. Refinement of the vertical pressure grid

The radiance calculation in RTIASI-2 is performed assuming that the atmosphere is sub-divided into 43 homogeneous layers of fixed pressure levels. The thickness of the layers was selected to be less or at least equal to the IASI nominal vertical resolution (at least in the troposphere) and care was taken to select an adequate number of layers around the tropopause and the boundary layer. It should be noted however that the choice of the number of levels was the result of a compromise between computing resources and the accuracy of the RTIASI-2 radiance calculation. The latter is determined by the temperature gradient across the layer since it is dependent on the evaluation of the Planck function at a mean layer temperature that should be representative of the temperature variation across the layer. In principle the greater the number of layers the higher the accuracy of the radiance computation. On the other hand, the numbers of layers largely control the execution time of the LBL computations and the size of the associated database. There is no need however to go to a disproportionate number of layers since any gain in accuracy that is below the noise level of the instrument is not be detected. Further than limiting the accuracy of the radiance computation, the choice of layering made in RTIASI-2 makes the execution time of the adjoint routines significantly longer than the execution time of the corresponding forward model. This is a direct consequence of the fact that in RTIASI-2 the layer mean temperature is obtained by use of the Curtis-Godson air density weighted temperature (T_{CG}) and a path integral has thus to be evaluated. This choice was rendered necessary by the coarse spacing of the 43 layers grid. In fact it gives a representation of the layer mean temperature that is more accurate than the one that can be achieved by averaging the temperature at top and the bottom of the layer (T_A). Since execution time is a major issue in an operational environment, it would be desirable to have the number of vertical layers increased since as long as there are enough layers ensuring that the assumption of homogeneity within a layer is valid, the computation of the mean layer temperature by averaging the temperature at the top and bottom of the layer is not expected to introduce any significant error.

The above considerations have led to a revision of the pressure grid used in RTIASI-4. To arrive at the definition of the new pressure grid, tests were made where the sensitivity of the top of the atmosphere radiance to the refinement of the pressure grid was studied. In turn, each of the existent layers was divided into two sub-layers by adding one more pressure level in the middle of the layer. LBL radiances were then computed and compared with those obtained by dividing the atmosphere into the standard 43 layers.

Computations were made for several profiles representative of average situations in the atmosphere. Results show that water vapour channels are mostly sensitive to refinement of the grid between 600 and 100 hPa whereas for the channels in the temperature sounding bands most of the radiance difference is generated by the refinement of the grid in the stratopause and lower mesosphere. A preliminary version of the new pressure grid was thus obtained by doubling the number of levels between 600 and 100 hPa and above 20 hPa. The spacing of the grid above 20 hPa was further refined by iterating the process of doubling the number of layers until the difference T_{CG} - T_A was comparable to or smaller than the typical brightness temperature error attributed to the prediction of the transmittances in the fast model. The position of the layer boundaries where then finally adjusted in such a way as to have a smooth variation of the layer thickness with pressure. This has lead to the definition of a new pressure grid made of 90 levels with pressure ranging from 0.005 to 1050 hPa.

As discussed before a finer pressure grid would not only allow an improved accuracy in the radiance calculation but also a considerable gain of speed in the execution of the adjoint routines by replacing the Curtis-Godson mean layer temperature with a more affordable quantity. The error resulting from the introduction of the mean layer temperature T_A has been evaluated by computing the statistics of the difference T_{CG} -T_A. Results are shown in Fig. 4 where the bias, standard deviation and rms is plotted for the set of 117 profiles selected to validate RTIASI-4 (for details on the profiles see section 11.2).

Larger errors are in general obtained for the uppermost, thicker layers where the assumption of homogeneity within the layer is weaker. Since radiances are the quantities that will be used, it is useful to understand how the use of the two different definitions of layer average temperature affects the RTIASI-4 radiance L. This is shown in Fig. 5 where the statistics of the difference $L_{T_{CG}} - L_{T_A}$ is plotted for the 117 profiles. As shown in Fig. 5, differences are larger in the spectral regions where the peak of the channel weighting function is higher. This is consistent with the results shown in Fig. 4 since the higher the peak of the weighting function the larger the contribution of the upper layers to the top of atmosphere radiance. In absolute terms, differences shown in Fig. 5 are considerably below the noise of the IASI instrument and a small fraction of the error that can be attributed to errors in the prediction of the transmittances.

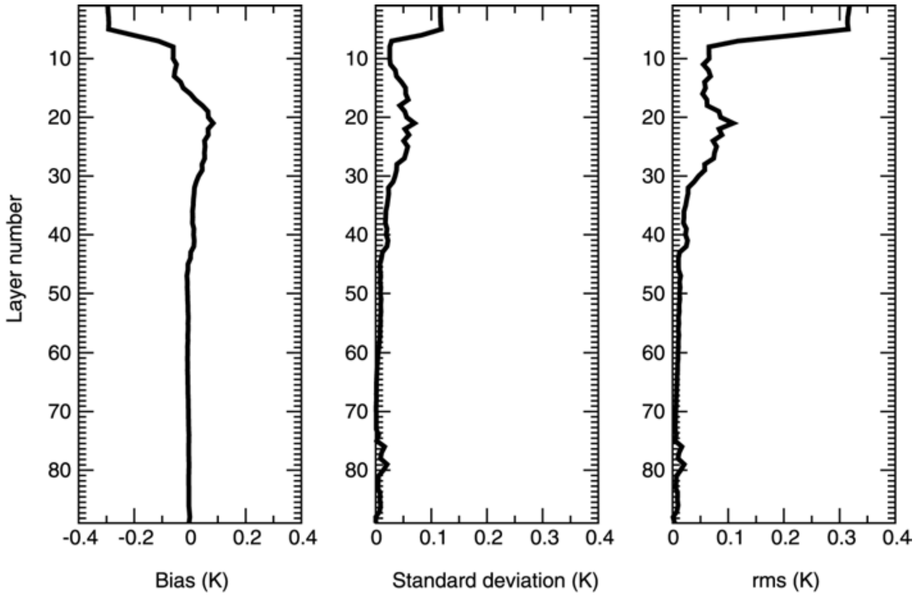

Figure 4. Statistics of the difference T_G-T_A. *Layers are numbered from 1 (top of the atmosphere) to 89 (surface).*

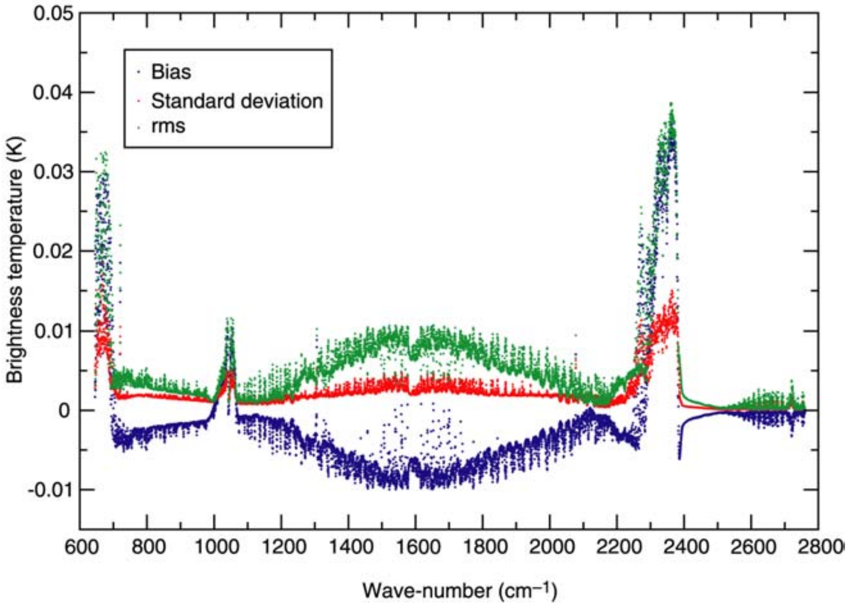

Figure 5 . Statistics of the difference $L_{T_{CG}} - L_{T_A}$ *for 117 profiles.*

It was previously observed that in an effort to refine the pressure grid there is no need to go to a disproportionate number of levels since any gain in accuracy below the instrument noise will not be detected. To test the absolute accuracy of the radiance calculation performed using the 90 level pressure grid, LBL radiance spectra (L_{89}) were computed for each of the 117 profiles by dividing the atmosphere into the standard 89 layers and then compared to the equivalent spectra (L_{178}) computed by dividing the atmosphere in 178 layers obtained by halving each of the layers of the 89-layer grid. Although in principle one could have chosen a different number of layers or made a different choice of layering, the 178 layers grid was convenient and easy to implement. In fact the number of layers is so large that the generality of the results should not be affected. The statistics of the difference L_{89}-L_{178} is shown in Fig. 6 where the ratio of the rms error to the IASI radiance noise is plotted. It can be seen that the error-to-noise ratio is considerably below unity for all channels. This means that any gain in accuracy in radiance computation achieved by refining further the 90 levels pressure grid will not be detected by IASI.

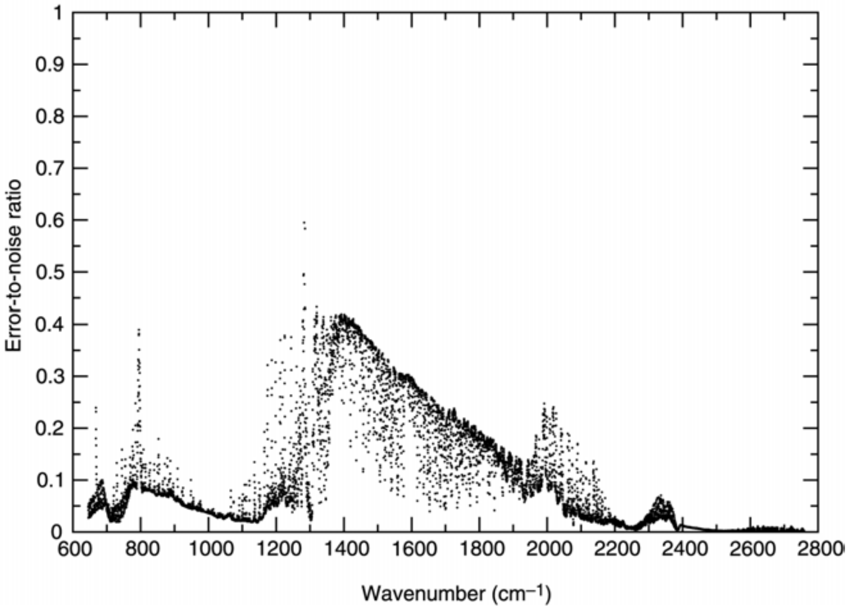

Figure 6. Statistics of the difference L_{89}-L_{178} *for 117 profiles.*

Finally, the impact of the choice of layering on LBL radiances has been evaluated by simulating GENLN2 level 1C spectra using the layering definitions adopted in RTIASI-2 and RTIASI-4 (spectra L_{43} and L_{90} respectively) for three different atmospheres. Results are shown in Fig. 7 where the difference L_{43}-L_{90} is plotted for a mid-latitude, artic and tropical profile obtained from the 34 profile set using to train the ozone fast transmittance model. Larger differences are observed across the whole 6.3 μm (1594 cm^{-1}) water vapour band and in the centre of the 4.3 μm (2325 cm^{-1}) band with a lesser impact in the 15 μm (660 cm^{-1}) band. It is evident from Fig.7 that differences depend on the atmospheric state and in particular on the vertical gradients of water vapour and temperature in the upper troposphere and lower stratosphere.

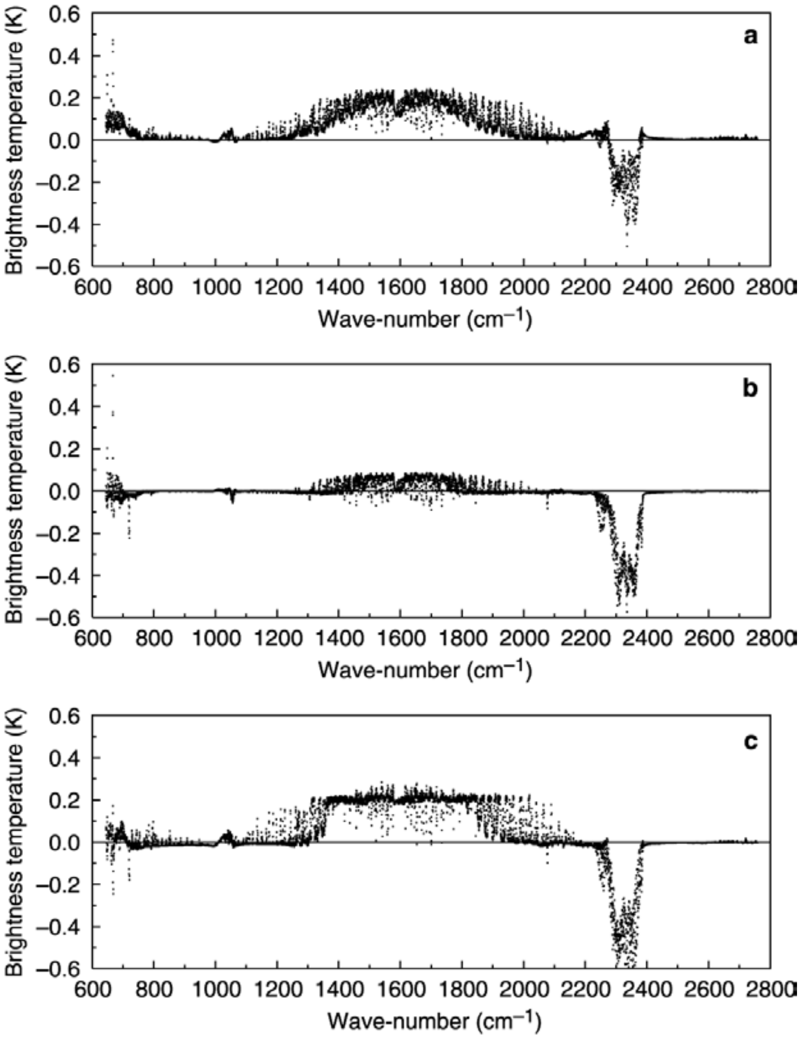

Figure 7. Difference between GENLN2 level 1C spectra obtained using the layering definitions adopted in RTIASI-2 and RTIASI-4. Results are shown for (a) Mid-latitude spectrum; (b) Artic spectrum; (c) Tropical spectrum.

9. Inclusion of trace gases CO_2, N_2O, CO and CH_4 as profile variables in RTIASI

RTIASI contains a fast model of the transmittances of the atmospheric gases that is generated from accurate LBL transmittances for a set of diverse atmospheric profiles. The monochromatic transmittances are convolved with the appropriate ISRF and used to compute channel-specific regression coefficients by use of a selected set of predictors (Matricardi and Saunders, 1999). In RTIASI-2 only H_2O and O_3 were allowed to vary. The other atmospheric gases (referred to as fixed) included in the LBL computations were held constant and are not profile variables in fast model. Although, by definition, spatial and temporal variations of fixed gases should not contribute significantly to the observed radiance, in localized IASI spectral regions the variability of CO, CH_4, N_2O and CO_2 generates a signal that can considerably exceed the instrumental noise. To improve the accuracy of the radiance simulation in RTIASI-4, CO_2, N_2O, CO and CH_4 profiles are now allowed to vary and are profile variables in the fast model with H_2O and O_3.

For each of the gases allowed to vary, the profiles used to compute the database of LBL transmittances are chosen to represent the range of variations in absorber amount found in the real atmosphere and should be representative of the gas observed behavior. The trace gases profiles used in RTIASI-4 are a blend of profiles from in-situ measurements and chemistry model (for water vapour, ozone and temperature profiles details can be found in Matricardi and Saunders (1999)).

The CO_2 profiles were assembled assuming that the vertical distribution of this gas is constant in the troposphere and decreases by 5 to 10 ppmv between the tropopause and about 22 km altitude (see Bischof et al, 1985). No further change is assumed above this layer. The seasonal and spatial variations we have used are based on the data accessible on the GLOBALVIEW database (GLOBALVIEW- CO2, 2000). CO_2 profiles were generated on the basis of the season/latitude classification used for the original temperature/humidity 43 profile set. Mixing ratios apply in year 2005 assuming an increase of concentration with time by 1.5 ppmv/year.

For the generation of the N_2O profiles we assumed N_2O is well mixed in the troposphere. The N_2O level in the lower troposphere is monitored by the Climate Monitoring and Diagnostic Laboratory (CMDL) of the national Oceanic and Atmospheric Administration (NOAA) and by the Advanced Global Atmospheric Gas Experiment (AGAGE) program through measurement made at a world-wide distributed network of stations (for further information see http://www.cmdl.noaa.gov and http://www.cdiac.ornl.gov/ndps/alegage.html). The N_2O profile set was generated from Cryogenic Limb Array Etalon Spectrometer (CLAES) measurements in the stratosphere and from CMDL and AGAGE measurements at the surface. The CLAES instrument has flown on board the Upper Atmosphere Research Satellite (UARS) (Reber et al. 1993) to provide stratospheric mixing ratios for 23 different molecular species. It views up to the 80 degree latitude bands providing essentially global coverage of the stratosphere and the mesosphere. Profiles for N_2O are available from 19-1-1992 to 13-3-1993 and are given at 4 degree latitude intervals and gridded to the UARS pressure array. To generate the N_2O profile set, stratospheric profiles from CLAES were firstly selected for the locations that are nearest to the ones of the original 43 temperature/humidity profiles, then, depending on season and latitude, joined by parabolae to a constant tropospheric mixing ratio based on measurements obtained at the surface. We then generated a preliminary N_2O 42 profile set using the monthly mean profile at each location. The final profile set was obtained by replacing in turn each of the monthly mean profiles with either the minimum or maximum profile if the latter was found to extend the range of variability of the set based on the monthly mean profiles.

The CO profile set was generated assembling profiles based on MOZART 3D model calculations (Brasseur et al., 1998; Cunnold, 2001) and measurements taken during the STRATOZ III and TROPOZ II campaign in the Austral summer, 4-26 June 1984, and in the Austral winter, 9 January to 1 February 1991 (Marenco et al., 1995). CO profiles from the STRATOZ and TROPOZ experiments were measured from a Caravelle aircraft whose flight path was a meridional track in two hemispheres, starting from Europe and passing over Greenland, North and South America, and West Africa. Profiles from MOZART extend from 32 to 1000 hPa whereas profiles from STRATOZ/TROPOZ were measured between 0 and 12 km. Since no stratospheric data were available from these sources, mixing ratios in the troposphere were extrapolated to the stratosphere assuming a lapse rate equal to the one from the corresponding seasonal USAFGL CO profile. The final CO 42 profile set was then obtained by selecting the CO profiles that were nearest (in terms of season and latitude) to the original 42 temperature/humidity profiles.

For CH_4, profile concentrations in the troposphere are based on the IMAGES model calculations (Müller and Brasseur, 1995; Clerbaux et al., 1998). The profile set covers the seasonal cycle of the gas. Although the latitudinal gradient was retained, absolute values at all levels were scaled to reflect recent estimates of surface values from measurements made at the stations of the CMDL network. Tropospheric mixing ratios were joined by parabola to stratospheric measurements made by CLAES and the final CH_4 42 profile set was then assembled by using the same methods described for N_2O. For CH_4 and N_2O, profiles are assumed to apply in year 2005 based on a recently measured rate of increase of 0.3%/year that reflects not only growth in the measured surface-based concentrations from 1995-2000 but also very slight change in calibration.

The general 42 profile set thus obtained (the original 42 temperature/humidity profiles plus CO_2, N_2O, CO and CH_4 profiles) is now used in RTIASI-4 to generate regression coefficients for fixed gases, H_2O, CO_2, N_2O, CO and CH_4. Note that a separate training set (33 profiles) is used for ozone. For either sets an average profile is added to serve as a reference profile. A plot of the training set for each of the newly added variable trace gas is shown in figures 8 through 11.

As stated in section 2, the total model transmittance is written according to Eq. 5. For not-monochromatic channels the convolution of the transmittance of all the gases $\hat{\tau}^{tot}_{\tilde{\nu}^*,j} = \hat{\tau}^{fix+wv+CO_2+O_3+N_2O+CO+CH_4}_{\tilde{\nu}^*,j}$ differs from the product of the transmittance of the single gases convolved individually. To reduce the errors introduced by separation of the gas transmittances after convolution, we divided the channel range into 12 sets and computed transmittances for different combinations of gases. In each band the total transmittance was then obtained as shown in tables 3 and 4. The superscripts denote what was included in the LBL computations and the terms on the right hand side are what is predicted by the fast model [for example, for set 1 we define $\hat{\tau}^{wv}_{\tilde{\nu}^*,j} = \left(\dfrac{\hat{\tau}^{fix+wv+CO_2}_{\tilde{\nu}^*,j}}{\hat{\tau}^{fix+CO_2}_{\tilde{\nu}^*,j}} \right)$, $\hat{\tau}^{CO_2}_{\tilde{\nu}^*,j} = \left(\dfrac{\hat{\tau}^{fix+CO_2}_{\tilde{\nu}^*,j}}{\hat{\tau}^{fix}_{\tilde{\nu}^*,j}} \right)$ and so on].

It can be seen that all the terms but the one accounting for the correct total convolved transmittance cancel (in each spectral range we included only those molecules that contribute to the total absorption).

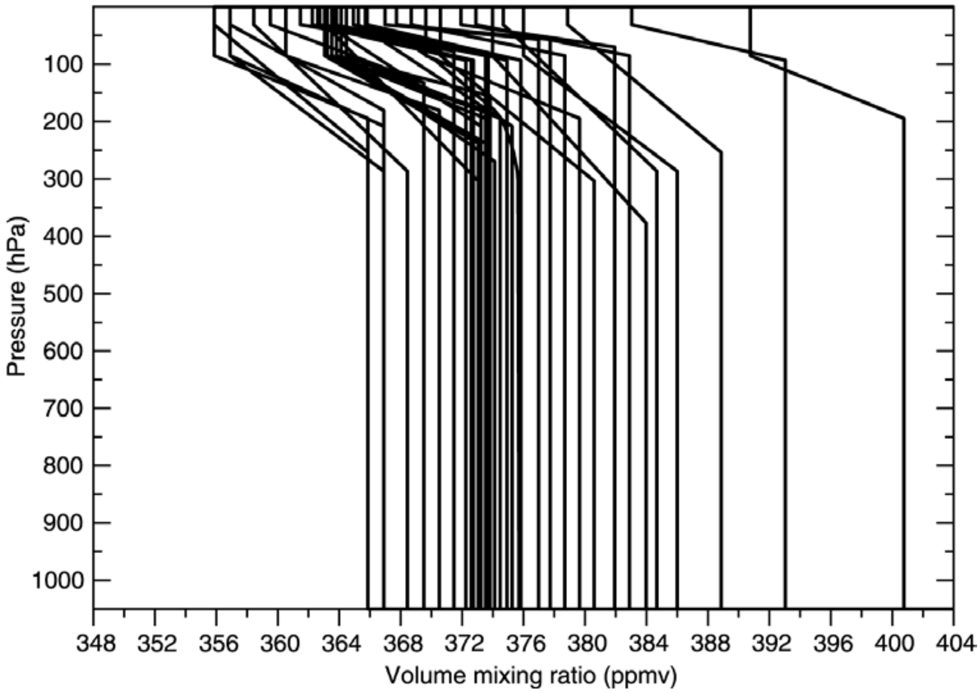

Figure 8. The CO_2 profile set used in RTIASI-4.

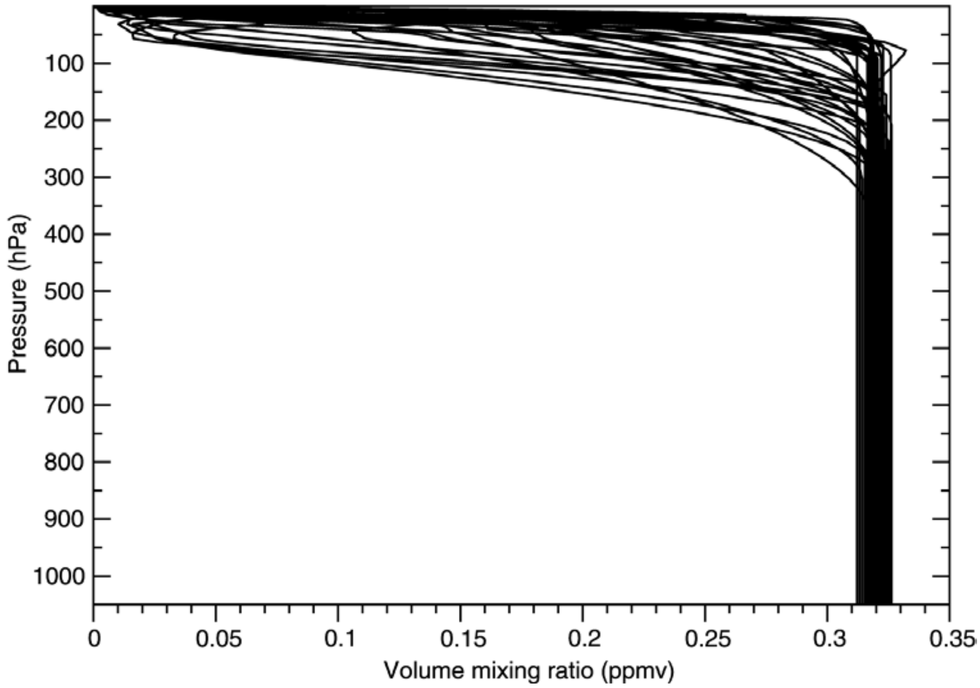

Figure 9. The N_2O profile set used in RTIASI-4.

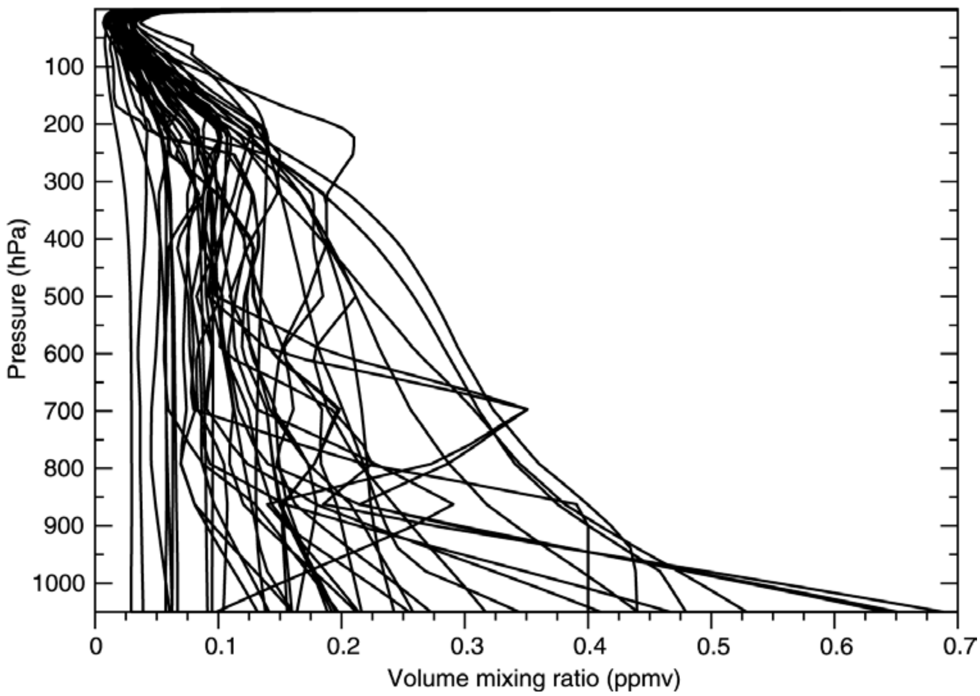

Figure 10. The CO profile set used in RTIASI-4.

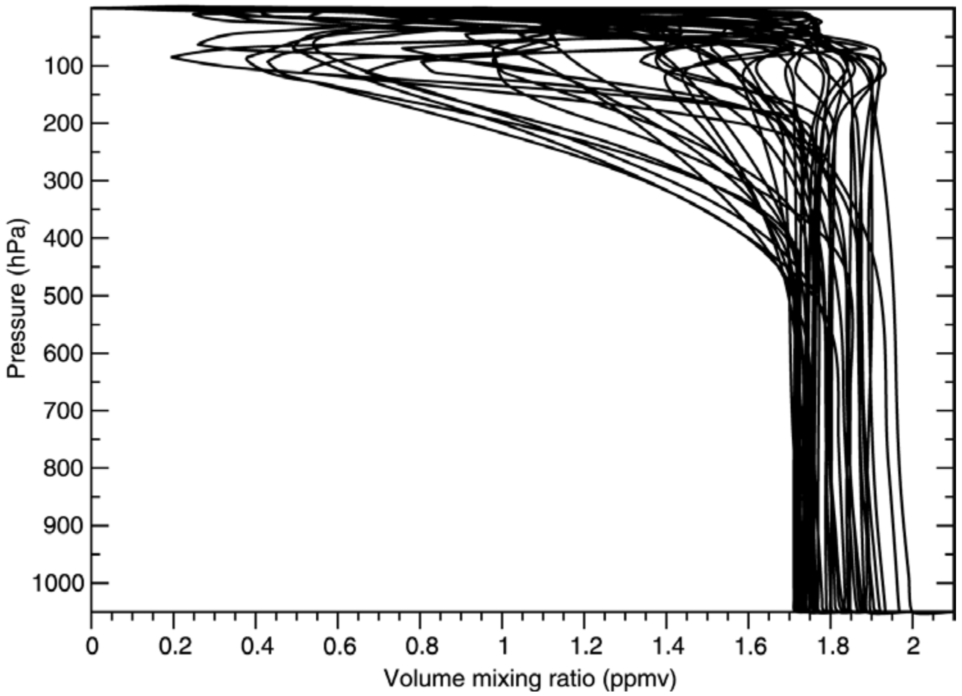

Figure 11. The CH4 profile set used in RTIASI-4.

Set 1 [Channel 1-1801]

$$\hat{\tau}^{tot}_{\tilde{v}^*,j} = \hat{\tau}^{fix}_{\tilde{v}^*,j}\left(\frac{\hat{\tau}^{fix+CO_2}_{\tilde{v}^*,j}}{\hat{\tau}^{fix}_{\tilde{v}^*,j}}\right)\left(\frac{\hat{\tau}^{fix+wv+CO_2}_{\tilde{v}^*,j}}{\hat{\tau}^{fix+CO_2}_{\tilde{v}^*,j}}\right)\left(\frac{\hat{\tau}^{fix+wv+CO_2+O_3}_{\tilde{v}^*,j}}{\hat{\tau}^{fix+wv+CO_2}_{\tilde{v}^*,j}}\right)$$

Set 2 [Channel 1802-2220]

$$\hat{\tau}^{tot}_{\tilde{v}^*,j} = \hat{\tau}^{fix}_{\tilde{v}^*,j}\left(\frac{\hat{\tau}^{fix+CH_4}_{\tilde{v}^*,j}}{\hat{\tau}^{fix}_{\tilde{v}^*,j}}\right)\left(\frac{\hat{\tau}^{fix+CH_4+N_2O}_{\tilde{v}^*,j}}{\hat{\tau}^{fix+CH_4}_{\tilde{v}^*,j}}\right)\left(\frac{\hat{\tau}^{fix+wv+CH_4+N_2O}_{\tilde{v}^*,j}}{\hat{\tau}^{fix+CH_4+N_2O}_{\tilde{v}^*,j}}\right)\left(\frac{\hat{\tau}^{fix+wv+CH_4+N_2O+O_3}_{\tilde{v}^*,j}}{\hat{\tau}^{fix+wv+CH_4+N_2O}_{\tilde{v}^*,j}}\right)$$

Set 3 [Channel 2221-2821]

$$\hat{\tau}^{tot}_{\tilde{v}^*,j} = \hat{\tau}^{fix}_{\tilde{v}^*,j}\left(\frac{\hat{\tau}^{fix+CH_4}_{\tilde{v}^*,j}}{\hat{\tau}^{fix}_{\tilde{v}^*,j}}\right)\left(\frac{\hat{\tau}^{fix+CH_4+N_2O}_{\tilde{v}^*,j}}{\hat{\tau}^{fix+CH_4}_{\tilde{v}^*,j}}\right)\left(\frac{\hat{\tau}^{fix+CH_4+N_2O+CO_2}_{\tilde{v}^*,j}}{\hat{\tau}^{fix+CH_4+N_2O}_{\tilde{v}^*,j}}\right)\left(\frac{\hat{\tau}^{fix+CH_4+N_2O+CO_2+wv}_{\tilde{v}^*,j}}{\hat{\tau}^{fix+CH_4+N_2O+CO_2}_{\tilde{v}^*,j}}\right)\left(\frac{\hat{\tau}^{fix+CH_4+N_2O+CO_2+wv+O_3}_{\tilde{v}^*,j}}{\hat{\tau}^{fix+CH_4+N_2O+CO_2+wv}_{\tilde{v}^*,j}}\right)$$

Set 4 [Channel 2822-3021]

$$\hat{\tau}^{tot}_{\tilde{v}^*,j} = \hat{\tau}^{fix}_{\tilde{v}^*,j}\left(\frac{\hat{\tau}^{fix+CH_4}_{\tilde{v}^*,j}}{\hat{\tau}^{fix}_{\tilde{v}^*,j}}\right)\left(\frac{\hat{\tau}^{fix+CH_4+CO_2}_{\tilde{v}^*,j}}{\hat{\tau}^{fix+CH_4}_{\tilde{v}^*,j}}\right)\left(\frac{\hat{\tau}^{fix+wv+CH_4+CO_2}_{\tilde{v}^*,j}}{\hat{\tau}^{fix+CH_4+CO_2}_{\tilde{v}^*,j}}\right)\left(\frac{\hat{\tau}^{fix+wv+CH_4+CO_2+O_3}_{\tilde{v}^*,j}}{\hat{\tau}^{fix+wv+CH_4+CO_2}_{\tilde{v}^*,j}}\right)$$

Set 5 [Channel 3022-4421]

$$\hat{\tau}^{tot}_{\tilde{v}^*,j} = \hat{\tau}^{fix}_{\tilde{v}^*,j}\left(\frac{\hat{\tau}^{fix+CH_4}_{\tilde{v}^*,j}}{\hat{\tau}^{fix}_{\tilde{v}^*,j}}\right)\left(\frac{\hat{\tau}^{fix+wv+CH_4}_{\tilde{v}^*,j}}{\hat{\tau}^{fix+CH_4}_{\tilde{v}^*,j}}\right)\left(\frac{\hat{\tau}^{fix+wv+CH_4+O_3}_{\tilde{v}^*,j}}{\hat{\tau}^{fix+wv+CH_4}_{\tilde{v}^*,j}}\right)$$

Set 6 [Channel 4422-4821]

$$\hat{\tau}^{tot}_{\tilde{v}^*,j} = \hat{\tau}^{fix}_{\tilde{v}^*,j}\left(\frac{\hat{\tau}^{fix+wv}_{\tilde{v}^*,j}}{\hat{\tau}^{fix}_{\tilde{v}^*,j}}\right)\left(\frac{\hat{\tau}^{fix+wv+O_3}_{\tilde{v}^*,j}}{\hat{\tau}^{fix+wv}_{\tilde{v}^*,j}}\right)$$

Table 3. The transmittances combinations used to generate regression coefficients in RTIASI-4

Set 7 [Channel 4822-5021]

$$\hat{\tau}^{tot}_{\tilde{v}^*,j} = \hat{\tau}^{fix}_{\tilde{v}^*,j} \left(\frac{\hat{\tau}^{fix+N_2O}_{\tilde{v}^*,j}}{\hat{\tau}^{fix}_{\tilde{v}^*,j}}\right) \left(\frac{\hat{\tau}^{fix+CO_2+N_2O}_{\tilde{v}^*,j}}{\hat{\tau}^{fix+N_2O}_{\tilde{v}^*,j}}\right) \left(\frac{\hat{\tau}^{fix+wv+CO_2+N_2O}_{\tilde{v}^*,j}}{\hat{\tau}^{fix+CO_2+N_2O}_{\tilde{v}^*,j}}\right) \left(\frac{\hat{\tau}^{fix+wv+CO_2+N_2O+O_3}_{\tilde{v}^*,j}}{\hat{\tau}^{fix+wv+CO_2+N_2O}_{\tilde{v}^*,j}}\right)$$

Set 8 [Channel 5022-5400]

$$\hat{\tau}^{tot}_{\tilde{v}^*,j} = \hat{\tau}^{fix}_{\tilde{v}^*,j} \left(\frac{\hat{\tau}^{fix+CO_2}_{\tilde{v}^*,j}}{\hat{\tau}^{fix}_{\tilde{v}^*,j}}\right) \left(\frac{\hat{\tau}^{fix+wv+CO_2}_{\tilde{v}^*,j}}{\hat{\tau}^{fix+CO_2}_{\tilde{v}^*,j}}\right) \left(\frac{\hat{\tau}^{fix+wv+CO_2+O_3}_{\tilde{v}^*,j}}{\hat{\tau}^{fix+wv+CO_2}_{\tilde{v}^*,j}}\right)$$

Set 9 [Channel 5401-6601]

$$\hat{\tau}^{tot}_{\tilde{v}^*,j} = \hat{\tau}^{fix}_{\tilde{v}^*,j} \left(\frac{\hat{\tau}^{fix+CO}_{\tilde{v}^*,j}}{\hat{\tau}^{fix}_{\tilde{v}^*,j}}\right) \left(\frac{\hat{\tau}^{fix+CO+N_2O}_{\tilde{v}^*,j}}{\hat{\tau}^{fix+CO}_{\tilde{v}^*,j}}\right) \left(\frac{\hat{\tau}^{fix+CO+N_2O+CO_2}_{\tilde{v}^*,j}}{\hat{\tau}^{fix+CO+N_2O}_{\tilde{v}^*,j}}\right) \left(\frac{\hat{\tau}^{fix+CO+N_2O+CO_2+wv}_{\tilde{v}^*,j}}{\hat{\tau}^{fix+CO+N_2O+CO_2}_{\tilde{v}^*,j}}\right) \left(\frac{\hat{\tau}^{fix+CO+N_2O+CO_2+wv+O_3}_{\tilde{v}^*,j}}{\hat{\tau}^{fix+CO+N_2O+CO_2+wv}_{\tilde{v}^*,j}}\right)$$

Set 10 [Channel 6602-6860]

$$\hat{\tau}^{tot}_{\tilde{v}^*,j} = \hat{\tau}^{fix}_{\tilde{v}^*,j} \left(\frac{\hat{\tau}^{fix+CO_2}_{\tilde{v}^*,j}}{\hat{\tau}^{fix}_{\tilde{v}^*,j}}\right) \left(\frac{\hat{\tau}^{fix+wv+CO_2}_{\tilde{v}^*,j}}{\hat{\tau}^{fix+CO_2}_{\tilde{v}^*,j}}\right) \left(\frac{\hat{\tau}^{fix+wv+CO_2+O_3}_{\tilde{v}^*,j}}{\hat{\tau}^{fix+wv+CO_2}_{\tilde{v}^*,j}}\right)$$

Set 11 [Channel 6861-8061]

$$\hat{\tau}^{tot}_{\tilde{v}^*,j} = \hat{\tau}^{fix}_{\tilde{v}^*,j} \left(\frac{\hat{\tau}^{fix+CH_4}_{\tilde{v}^*,j}}{\hat{\tau}^{fix}_{\tilde{v}^*,j}}\right) \left(\frac{\hat{\tau}^{fix+CH_4+N_2O}_{\tilde{v}^*,j}}{\hat{\tau}^{fix+CH_4}_{\tilde{v}^*,j}}\right) \left(\frac{\hat{\tau}^{fix+CH_4+N_2O+CO_2}_{\tilde{v}^*,j}}{\hat{\tau}^{fix+CH_4+N_2O}_{\tilde{v}^*,j}}\right) \left(\frac{\hat{\tau}^{fix+CH_4+N_2O+CO_2+wv}_{\tilde{v}^*,j}}{\hat{\tau}^{fix+CH_4+N_2O+CO_2}_{\tilde{v}^*,j}}\right) \left(\frac{\hat{\tau}^{fix+CH_4+N_2O+CO_2+wv+O_3}_{\tilde{v}^*,j}}{\hat{\tau}^{fix+CH_4+N_2O+CO_2+wv}_{\tilde{v}^*,j}}\right)$$

Set 12 [Channel 8062-8461]

$$\hat{\tau}^{tot}_{\tilde{v}^*,j} = \hat{\tau}^{fix}_{\tilde{v}^*,j} \left(\frac{\hat{\tau}^{fix+CH_4}_{\tilde{v}^*,j}}{\hat{\tau}^{fix}_{\tilde{v}^*,j}}\right) \left(\frac{\hat{\tau}^{fix+wv+CH_4}_{\tilde{v}^*,j}}{\hat{\tau}^{fix+CH_4}_{\tilde{v}^*,j}}\right) \left(\frac{\hat{\tau}^{fix+wv+CH_4+O_3}_{\tilde{v}^*,j}}{\hat{\tau}^{fix+wv+CH_4}_{\tilde{v}^*,j}}\right)$$

Table 4. The transmittance combinations used to generate regression coefficients in RTIASI-4

10. Predictors for line absorption

The functional dependence of the predictors $X_{j,k}$ used to parameterize the optical depths $\hat{\rho}_{j,\tilde{\nu}^*}$ depends mainly on factors such as the absorbing gas, spectral response function and spectral region although the order in which the gases are separated out and the layer thickness can also be important. Within the framework of a linear regression method, the large variability between extreme profiles makes the regression prone to numerical instabilities and thus difficulties in calculating the coefficients can arise if the predictors are allowed to vary too much. To avoid these difficulties, most of the predictors in RTIASI-4 are defined by taking the ratio with respect to the values for a reference profile. Optical depths are less difficult to model in the spectral regions where absorption is due to gases whose concentration is held fixed in that, for a given viewing angle, the optical depth then depends only on the temperature profile. For water vapour, ozone, CO_2, N_2O, CO and CH_4 sounding channels the variation in absorber amount has to be taken into account.

The fast transmittance model predicts the polychromatic layer optical depths defined in Eq. 3. One can formulate a model to compute the layer optical depth based on the assumption that the basic behavior of the quantity defined in Eq.3 is that of the layer optical depth for a gas in a homogeneous layer at pressure $p(j)$, temperature $T(j)$ and absorber amount $n(j)$. A set of basic predictors can then be defined based on simple functions of the viewing angle and of the profile variables in the layer j, $T_r(j)$, $W_r(j)$, $CO2_r(j)$, $N2O_r(j)$, $CO_r(j)$, $CH4_r(j)$ and $\delta T(j)$ (see table 8 for details). One can expect the layer optical depth to be proportional to $n(j)$ for weak absorption and $\sqrt{n(j)}$ for strong absorption. The absorption due to the combined effect of weak and strong lines can be obtained using an intermediate value of the exponent. This was accounted for by introducing a term proportional to $\sqrt[4]{n(j)}$. Values of the exponent greater than 1 were introduced to account for effects of higher order in the water vapour model since they were found to have some skill in the prediction of the optical depths for the more opaque cases. For the variable species the slowly varying dependence on temperature was modeled by introducing terms proportional to $n(j)\,\delta T(j)$ and $\sqrt{n(j)}\,\delta T(j)$. An additional term proportional to $n(j)\,\delta T(j)\left|\delta T(j)\right|$ was further introduced for the water vapour and CO model. The angular dependence was addressed by scaling the layer amount through the secant of the viewing angle.

The model for CO_2 is somewhat simpler than the one for the other variable species. For the range of variability covered in the training set, the variation of layer optical depth with CO_2 layer amount is basically linear. This is reflected in the choice of predictors (see table 5) that are formulated to basically reproduce the model for fixed gases (see below) plus a term to account for the dependence on CO_2 layer amount variation.

As discussed above, for a fixed viewing angle, the optical depth in the spectral regions where absorption from the fixed gases is predominantly depends only on the temperature profile. Consequently, the model for the fixed gases is based on predictors that depend on the ratio $T_r(j)$. First and second order terms were included. Terms that depend only on the viewing angle had also to be considered since the effect of a variable viewing angle is to impart an offset to the curve that represents the variation of optical depth with temperature.

So far, predictors have been defined based on layer quantities only. Since we are predicting polychromatic transmittances, adjustment terms must be included to extend the validity of the model from monochromatic to polychromatic transmittances. In fact account must be taken for the dependence of the layer transmittance on the properties of the atmosphere above the layer. Although the formulation of the layer optical depth given in Eq.3 reduce this dependence, the optical depth in layer j for two profiles having the same temperature $T(j)$ and gas amount $n(j)$ will in general differ if the profile above layer j is different. This effect can be modeled by introducing predictors representative of the effective temperature and species column density above the layer (Fleming and McMillin, 1977). Predictors based on the variables $T_w(j)$, $T_{fu}(j)$, $T_{fw}(j)$, $W_w(J)$, $CO2_w(j)$, $O_w(j)$, $N2O_w(j)$, $CO_w(j)$ and $CH4_w(j)$ (see table 8 for details) can then be used. The relation between these predictors and the optical properties of the gas is not obvious [for example the different form of the predictors used in the various trace gas models partly reflects the different order in which the gases are separated out (see tables 3 and 4)] and in absence of theoretical guidance the final form of these predictors was largely derived empirically.

Another issue that needs to be addressed in the compilation of the list of predictors is that in the IASI channels absorption by gas species cannot be considered to be completely uncorrelated with absorption by other gases. In the fact the quantity used in the regression is the “effective” layer optical depth defined in tables 3 and 4 and this can differ significantly from the layer optical depth computed for the single gas species alone. Thus, in spectral regions where absorption bands from different molecules overlap, the introduction of predictors accounting for the variable concentration of a concomitant absorbing molecule has to be envisaged (above all for those channels where the effective layer optical depth has to be predicted for a specie for whom just a few absorption lines are of importance). Because of the way the gases have been separated out, in RTIASI-4 channel dependent predictors are introduced for H_2O, CO_2 and N_2O and are listed with the other predictors and profile variables in tables 5, 6, 7 and 8 respectively.

Predictor	**H_2O**	**CO**	**O_3**
$X_{j,1}$	$(\sec(\theta)W_r(j))^2$	$\sec(\theta)CO2_r(j)$	$\sec(\theta)O_r(j)$
$X_{j,2}$	$\sec(\theta)W_w(j)$	$T_r^2(j)$	$\sqrt{\sec(\theta)O_r(j)}$
$X_{j,3}$	$(\sec(\theta)W_w(j))^2$	$\sec(\theta)T_r(j)$	$\sec(\theta)O_r(j)\delta T(j)$
$X_{j,4}$	$\sec(\theta)W_r(j)\delta T(j)$	$\sec(\theta)T_r^2(j)$	$(\sec(\theta)O_r(j))^2$
$X_{j,5}$	$\sqrt{\sec(\theta)W_r(j)}$	$T_r(j)$	$\sqrt{\sec(\theta)O_r(j)}\,\delta T(j)$
$X_{j,6}$	$\sqrt[4]{\sec(\theta)W_r(j)}$	$\sec(\theta)$	$\sec(\theta)O_r^2(j)O_w(j)$
$X_{j,7}$	$\sec(\theta)W_r(j)$	$\sec(\theta)T_w(j)$	$\frac{O_r(j)}{O_w(j)}\sqrt{\sec(\theta O_r(j)}$
$X_{j,8}$	$(\sec(\theta)W_r(j))^3$	$(\sec(\theta)CO2_w(j))^2$	$\sec(\theta)O_r(j)O_w(j)$
$X_{j,9}$	$(\sec(\theta)W_r(j))^4$	T_w^3	$O_r(j)\sec(\theta)\sqrt{O_w(j)\sec(\theta)}$
$X_{j,10}$	$\sec(\theta)W_r(j)\delta T(j)\lvert\delta T(j)\rvert$	0	$\sec(\theta)O_w(j)$
$X_{j,11}$	$(\sqrt{\sec(\theta)W_r(j)})\delta T(j)$	0	$(\sec(\theta)O_w(j))^2$
$X_{j,12}$	$\frac{\sec(\theta)W_r^2(j)}{W_{tw}(j)}$	0	0
$X_{j,13}$	$\frac{\sqrt{\sec(\theta)W_r(j)}\,W_r(j)}{W_{tw}(j)}$	0	0

For channels $\in$ ***[1802,4421]***

$X_{j,14}$	$\sec(\theta)CH4_r(j)$
$X_{j,15}$	$(\sec(\theta)CH4_r(j))^2\,\delta T$

For channels $\in$ ***[5022,5400]***

$X_{j,14}$	$\sec(\theta)CO2_r(j)$

For channels $\in$ ***[5401,6601]***

$X_{j,14}$	$\sec(\theta)CO2_r(j)$
$X_{j,15}$	$\sec(\theta)CO_r(j)$

For channels $\in$ ***[5401,6601]***

$X_{j,10}$	$\sec(\theta)CO_r(j)$
$X_{j,11}$	$\sec(\theta)T_w(j)\sqrt{T_r(j)}$

For channels $\in$ ***[6602,8061]***

$X_{j,10}$	$\sec(\theta)T_w(j)\sqrt{T_r(j)}$

Table 5. Predictors used in RTIASI-4 for Water vapour, CO_2 and ozone.

Predictor	CO	N_2O	CH_4
$X_{j,1}$	$\sec(\theta)\, CO_r(j)$	$\sec(\theta) \vert\, N2O_r(j)$	$\sec(\theta) \vert\, CH4_r(j)$
$X_{j,2}$	$\sqrt{\sec(\theta)\, CO_r(j)}$	$\sqrt{\sec(\theta)\, N2O_r(j)}$	$\sqrt{\sec(\theta)\, CH4_r(j)}$
$X_{j,3}$	$\sec(\theta)\, CO_r(j)\, \delta T(j)$	$\sec(\theta)\, N2O_r(j)\, \delta T(j)$	$\sec(\theta)\, CH4_r(j)\, \delta T(j)$
$X_{j,4}$	$(\sec(\theta)\, CO_r(j))^2$	$(\sec(\theta)\, N2O_r(j))^2$	$(\sec(\theta)\, CH4_r(j))^2$
$X_{j,5}$	$\sqrt{\sec(\theta)\, CO_r(j)}\, \delta T(j)$	$N2O_r(j)\, \delta T(j)$	$CH4_r(j)\, \delta T(j)$
$X_{j,6}$	$\sqrt[4]{\sec(\theta)\, CO_r(j)}$	$\sqrt[4]{\sec(\theta)\, N2O_r(j)}$	$\sqrt[4]{\sec(\theta)\, CH4_r(j)}$
$X_{j,7}$	$\sec(\theta)\, CO_r(j)\, \delta T(j) \vert \delta T(j) \vert$	$\sec(\theta)\, N2O_w(j)$	$\sec(\theta)\, CH4_{tw}(j)$
$X_{j,8}$	$\dfrac{\sec(\theta)\, CO_r^2(j)}{CO_w(j)}$	$\sec(\theta)\, N2O_{tw}(j)$	$CH4_{tw}(j)$
$X_{j,9}$	$\dfrac{\sqrt{\sec(\theta)\, CO_r(j)}\, CO_r(j)}{CO_w(j)}$	$N2O_{tw}(j)$	$(\sec(\theta)\, CH4_w(j))^2$
$X_{j,10}$	$\dfrac{\sec(\theta)\, CO_r^2(j)}{\sqrt{CO_w(j)}}$	$\dfrac{\sqrt{\sec(\theta)\, N2O_r(j)}\, N2O_r(j)}{N2O_w(j)}$	$\sec(\theta)\, CH4_w(j)$
$X_{j,11}$	$\dfrac{\sec(\theta)\, CO_r^2(j)}{\sqrt[4]{CO_w(j)}}$	0	$\dfrac{\sqrt{\sec(\theta)\, CH4_r(j)}\, CH4_r(j)}{CH4_w(j)}$

For channels $\in$ ***[1621,2821]***

$X_{j,11}$	$\sec(\theta)\, CH4_r(j)$
$X_{j,12}$	$\sec(\theta)\, CH4_w(j)$

For channels $\in$ ***[5401,6601]***

$X_{j,11}$	$\sec(\theta)\, CO_r(j)$
$X_{j,12}$	$\sec(\theta)^2\, CO_r(j)\, CO_w(j)$

Table 6. Predictors used in RTIASI-4 for CO, N_2O and CH_4.

Predictor	**Fixed Gases**
$X_{j,1}$	$\sec(\theta)$
$X_{j,2}$	$\sec^2(\theta)$
$X_{j,3}$	$\sec(\theta)T_r(j)$
$X_{j,4}$	$\sec(\theta)T_r^2(j)$
$X_{j,5}$	$T_r(j)$
$X_{j,6}$	$T_r^2(j)$
$X_{j,7}$	$\sec(\theta)T_{fw}(j)$
$X_{j,8}$	$\sec(\theta)T_{fu}(j)$

Table 7. Predictors used in RTIASI-4 for fixed gases.

$$T(l) = [T^{profile}(l+1) + T^{profile}(l)] / 2 \qquad T^*(l) = [T^{reference}(l+1) + T^{reference}(l)] / 2$$

$$W(l) = [W^{profile}(l+1) + W^{profile}(l)] / 2 \qquad W^*(l) = [W^{reference}(l+1) + W^{reference}(l)] / 2$$

$$O(l) = [O^{profile}(l+1) + O^{profile}(l)] / 2 \qquad O^*(l) = [O^{reference}(l+1) + O^{reference}(l)] / 2$$

$$CO(l) = [CO^{profile}(l+1) + CO^{profile}(l)] / 2 \qquad CO^*(l) = [CO^{reference}(l+1) + CO^{reference}(l)] / 2$$

$$CH_4(l) = [CH_4^{profile}(l+1) + CH_4^{profile}(l)] / 2 \qquad CH_4^*(l) = [CH_4^{reference}(l+1) + CH_4^{reference}(l)] / 2$$

$$N_2O(l) = [N_2O^{profile}(l+1) + N_2O^{profile}(l)] / 2 \qquad N_2O^*(l) = [N_2O^{reference}(l+1) + N_2O^{reference}(l)] / 2$$

$$CO_2(l) = [CO_2^{profile}(l+1) + CO_2^{profile}(l)] / 2 \qquad CO_2^*(l) = [CO_2^{reference}(l+1) + CO_2^{reference}(l)] / 2$$

$$T_r(l) = \frac{T(l)}{T^*(l)} \qquad \delta T(l) = T(l) - T^*(l) \qquad W_r(l) = \frac{W(l)}{W^*(l)} \qquad O_r(l) = \frac{O(l)}{O^*(l)}$$

$$CO_r(l) = \frac{CO(l)}{CO^*(l)} \qquad CH4_r(l) = \frac{CH_4(l)}{CH_4^*(l)} \qquad N2O_r(l) = \frac{N_2O(l)}{N_2O^*(l)} \qquad CO2_r(l) = \frac{CO_2(l)}{CO_2^*(l)}$$

$$T_w(l) = \{\textstyle\sum_{i=1}^{l} P(i)\,[P(i) - P(i-1)]\,T(i)\} / \{\textstyle\sum_{i=1}^{l} P(i)\,[P(i) - P(i-1)]\,T^*(i)\}$$

$$T_{fu}(l) = \{\textstyle\sum_{i=1}^{l} T(i)\} / \{\textstyle\sum_{i=1}^{l} T^*(i)\}$$

$$T_{fw}(l) = \{\textstyle\sum_{i=2}^{l} T(i)\} / \{\textstyle\sum_{i=2}^{l} T^*(i)\}$$

$$W_w(l) = \{\textstyle\sum_{i=1}^{l} P(i)\,[P(i) - P(i-1)]\,W(i)\} / \{\textstyle\sum_{i=1}^{l} P(i)\,[P(i) - P(i-1)]\,W^*(i)\}$$

$$W_{tw}(l) = \{\textstyle\sum_{i=1}^{l} P(i)\,[P(i) - P(i-1)]\,T(i)\,W(i)\} / \{\textstyle\sum_{i=1}^{l} P(i)\,[P(i) - P(i-1)]\,T^*(i)\,W^*(i)\}$$

$$O_w(l) = \{\textstyle\sum_{i=1}^{l} P(i)\,[P(i) - P(i-1)]\,O(i)\} / \{\textstyle\sum_{i=1}^{l} P(i)\,[P(i) - P(i-1)]\,O^*(j)\}$$

$$CO_w(l) = \{\textstyle\sum_{i=1}^{l} P(i)\,[P(i) - P(i-1)]\,CO(i)\} / \{\textstyle\sum_{i=1}^{l} P(i)\,[P(i) - P(i-1)]\,CO^*(j)\}$$

$$CO_{tw}(l) = \{\textstyle\sum_{i=1}^{l} P(i)\,[P(i) - P(i-1)]\,T(j)CO(i)\} / \{\textstyle\sum_{i=1}^{l} P(i)\,[P(i) - P(i-1)]\,T^*(j)CO^*(j)\}$$

$$CH4_w(l) = \{\textstyle\sum_{i=1}^{l} P(i)\,[P(i) - P(i-1)]\,CH_4(i)\} / \{\textstyle\sum_{i=1}^{l} P(i)\,[P(i) - P(i-1)]\,CH_4^*(j)\}$$

$$CH4_{tw}(l) = \{\textstyle\sum_{i=1}^{l} P(i)\,[P(i) - P(i-1)]\,T(j)\,CH_4(i)\} / \{\textstyle\sum_{i=1}^{l} P(i)\,[P(i) - P(i-1)]\,T^*(j)CH_4^*(j)\}$$

$$N2O_w(l) = \{\textstyle\sum_{i=1}^{l} P(i)\,[P(i) - P(i-1)]\,N_2O(i)\} / \{\textstyle\sum_{i=1}^{l} P(i)\,[P(i) - P(i-1)]\,N_2O^*(j)\}$$

$$N2O_{tw}(l) = \{\textstyle\sum_{i=1}^{l} P(i)\,[P(i) - P(i-1)]\,T(j)N_2O(i)\} / \{\textstyle\sum_{i=1}^{l} P(i)\,[P(i) - P(i-1)]\,T^*(j)N_2O^*(j)\}$$

$$CO2_w(l) = \{\textstyle\sum_{i=1}^{l} P(i)\,[P(i) - P(i-1)]\,CO_2(i)\} / \{\textstyle\sum_{i=1}^{l} P(i)\,[P(i) - P(i-1)]\,CO_2^*(j)\}$$

The $P(i)$'s are the values of the pressure at each level. $T^{profile}(l)$, $W^{profile}(l)$, $O^{profile}(l)$, $CO^{profile}(l)$, $CH_4^{profile}(l)$, $N_2O^{profile}(l)$ and $CO_2^{profile}(l)$ are the temperature and variable gases mixing ratio profiles. $T^{reference}(l)$, $W^{reference}(l)$, $O^{reference}(l)$, $CO^{reference}(l)$, $CH_4^{reference}(l)$, $N_2O^{reference}(l)$ and $CO_2^{reference}(l)$ are corresponding reference profiles. For these variables l refers to the lth level; otherwise l is the lth layer, i.e.the layer below the lth level (layers are numbered from 1 to 89). Note that we take $P(0) = 2P(1) - P(2)$ and $T_{fw}(1) = (P(2) - P(1))P(1)T(1)/T^*(1)$. Here θ is the zenith angle.

Table 8. Definition of profile variables used in predictors defined in tables 5, 6 and 7.

11. Performance of the fast model for simulation of IASI radiances

The accuracy of RTIASI-4 simulations can be assessed by a comparison of the transmittances and radiances computed by the fast model with the corresponding values from LBL models in different ways. Firstly the fast model transmittance profiles and top of the atmosphere radiances computed for the dependent set of profiles used to train the fast model can be compared with the LBL model equivalents to determine the accuracy of the fast model itself. Secondly a set of profiles independent of the regression coefficients can be used to allow uncertainties from different type of profiles to be included.

The comparison of transmittances is more useful to understand how the model performs and to see where it needs to be improved, but the comparison of radiances is the most important as the radiances are what will be used. The analysis of the results discussed below concentrates on the error of RTIASI-4 in terms of the bias, standard deviation and rms of the radiance and transmittances differences between the fast and LBL radiative transfer models.

11.1 Results for the dependent set of profiles

The simulation of the layer optical depth using Eq. 2 is the essence of a regression based fast radiative transfer model. For the 43 profile set, the dependent set of fast model transmittances were compared to LBL equivalents computed using GENLN2 for six scan angles from 0° to 64°. Results are shown in Fig. 12 where the maximum value of the rms of the difference between fast model and LBL layer-to-space transmittances is shown (both line and continuum contribution are included).

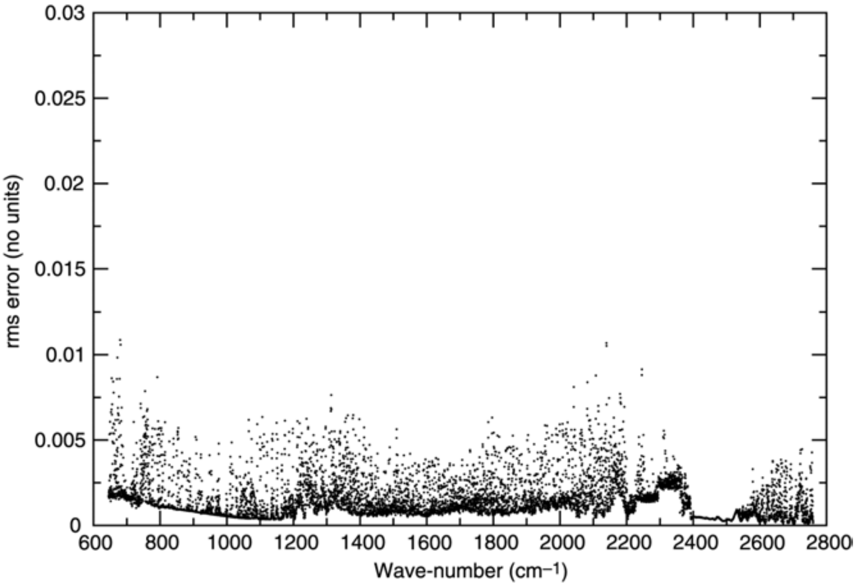

Figure 12. Maximum value of the rms of the difference between fast model and GENLN2 layer-to-space transmittances for 43 diverse profiles and 6 viewing angles.

Maximum errors are generally found near the peak of the weighting functions as shown in Fig. 13 where we plotted the level at which the maximum rms error is attained [levels are numbered from 1 (top of the atmosphere) to 90 (surface)]. It can be clearly seen that for the high peaking channels in the regions around 650 cm^{-1} and 2300 cm^{-1}, maximum errors are generally found at low- level numbers; in the window regions maximum errors are attained closer to the surface and in the strong water vapour band centred at 1594 cm^{-1}, maximum errors are found at increasingly lower level numbers as we move to channels that are less sensitive to surface.

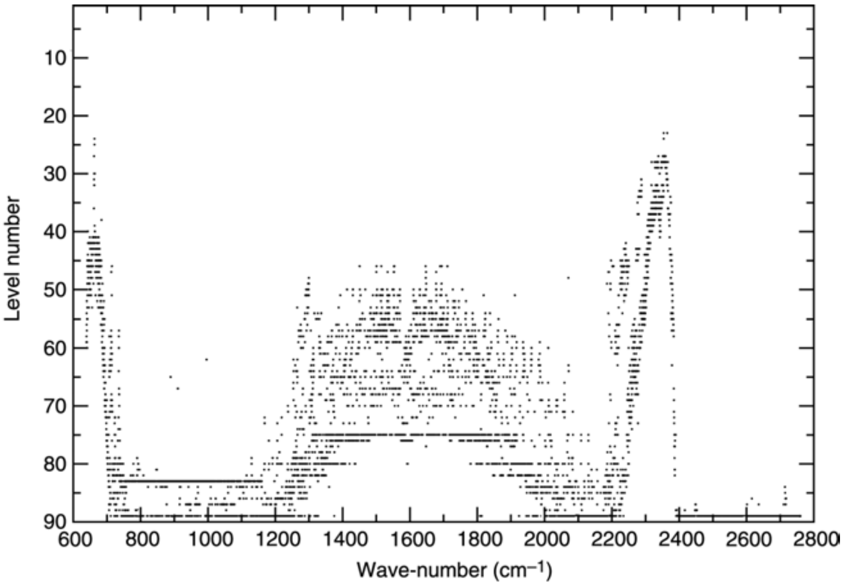

Figure 13. Level index at which the maximum rms error in transmittance is attained.

We also tested the accuracy of the fast model for the water continuum by comparing the fast model transmittances with CKD 2.4 equivalents for 43 profiles and six viewing angles. Results are shown in Fig. 14 where the maximum value of the rms of the difference between fast model and CKD 2.4 layer-to-space water vapour continuum transmittances is plotted. Errors are in general less than 0.002 and are consistently larger in the spectral regions where the contribution of the foreign-continuum is predominant.

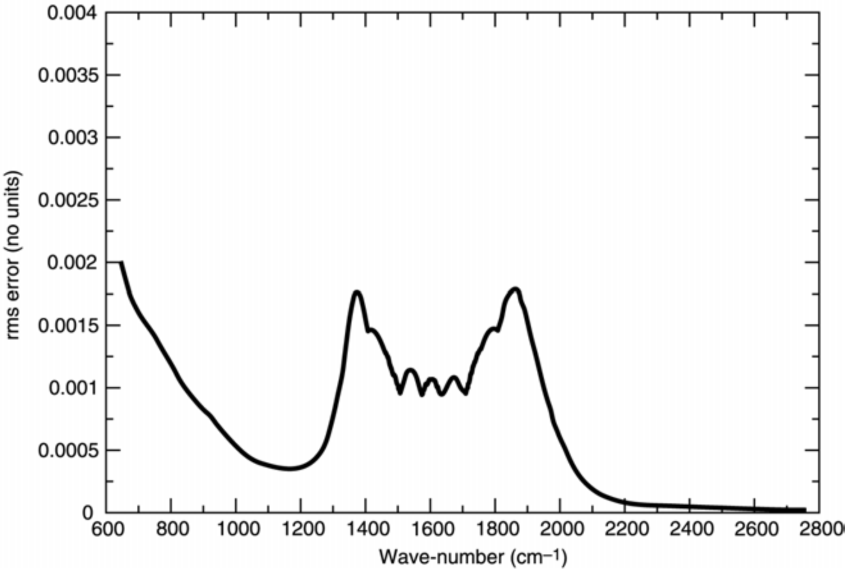

Figure 14. Maximum value of the rms of the difference between fast model and CKD 2.4 layer-to-space water vapour continuum transmittances for 43 diverse profiles and 6 viewing angles.

Errors in brightness temperature were computed by using the fast model transmittances as compared with those computed by using the LBL and CKD 2.4 transmittances in Eq. 7. Results for the dependent 43 profile set and six viewing angles are shown in Fig. 15 where the mean value, standard deviation and rms of the difference between the fast and LBL computed radiances in units of equivalent black body brightness temperature is given for both the RTIASI-4 and RTIASI-2 models.

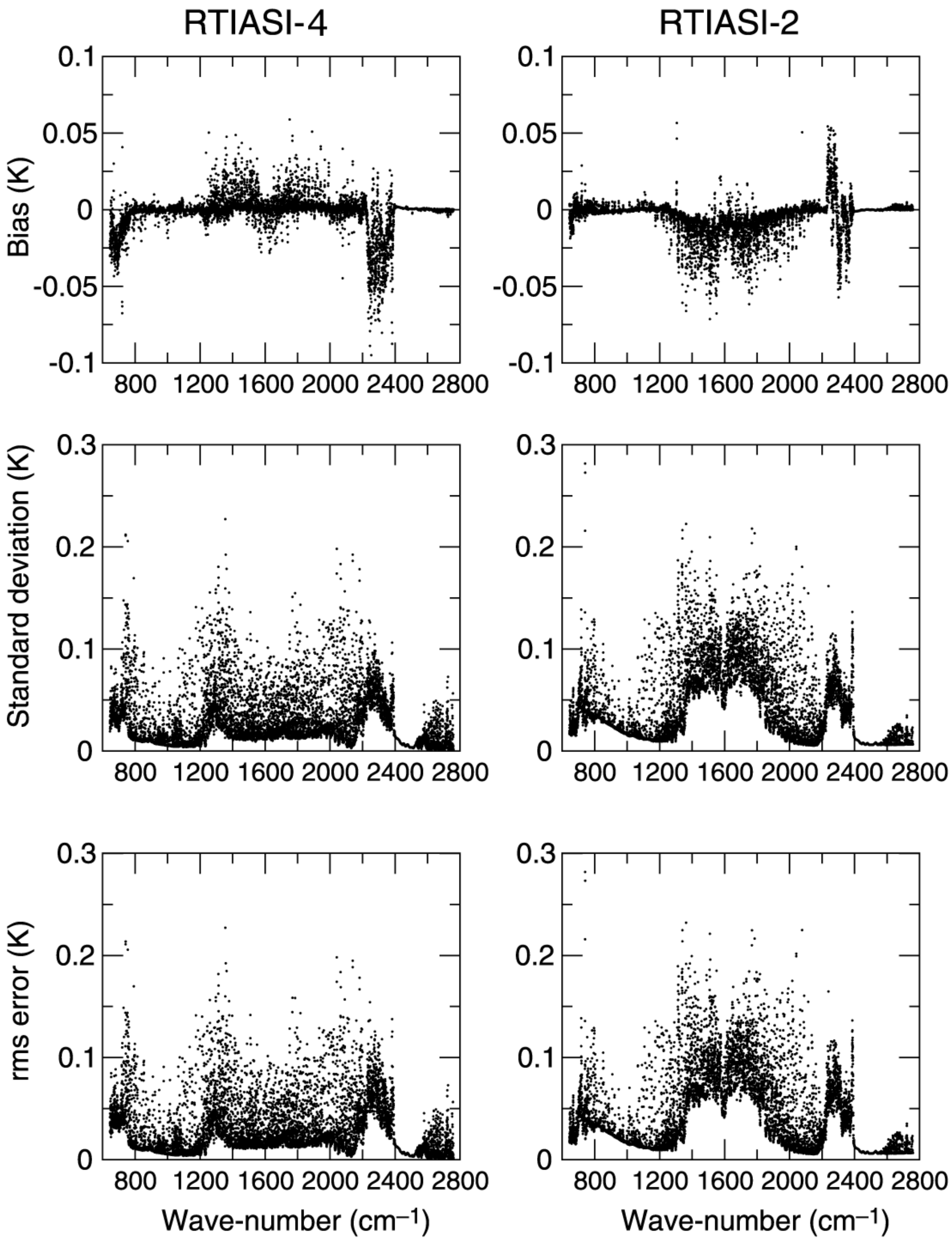

Figure 15. Mean value, standard deviation and rms of the difference between fast model and GENLN2 computed brightness temperatures for 43 diverse profiles and 6 viewing angles.

It should be noted that since no ozone profiles are included in the 43 profile set, transmittances for a climatological ozone profile are used so that no conclusions can be draw on the accuracy of the model for the channels where ozone absorption is relevant. For RTIASI-4 biases are typically less than 0.05 K (absolute value) and contribute only fractionally to the rms error that is generally less than 0.1 K. Larger rms errors (still less than 0.2 K) occur for a small number of outlier channels where absorption from lower water vapour is important. The rms error score for RTIASI-4 compares favourably with the one for RTIASI-2. Errors have been dramatically reduced in the strong water vapour band largely as a consequence of the introduction of a dedicated water vapour continuum model and the weighting of the data prior to the regression. A smaller role has also been played by the revision of two of the predictors used in the original RTIASI-2 water model [in the RTIASI-4 water model the variable $W_{tw}(j)$ has replaced $W_{w}(j)$ in predictors $X_{j,12}$ and $X_{j,13}$ (see table

5)]. The introduction of a dedicated water vapour continuum model has also resulted in a significant reduction of the errors in the 11 μm (900 cm^{-1}) window region. It should also been noted that despite the fact CO_2, N_2O, CO and CH_4 are treated as variable gases in RTIASI-4, errors in the regions where absorption from these molecules takes place are comparable to those in RTIASI-2 where only water vapour and ozone are allowed to vary. Although this is mainly a result of the sensible transmittance model adopted for these molecules, it should be stressed that the range of variability for these gases is only a fraction of that for water vapour. Some more insight into the performance of RTIASI-4 can be gained by looking at the distribution of the fitting errors as a function of viewing angle. This is given in Fig.16 where the binned distribution of channels with rms error is plotted.

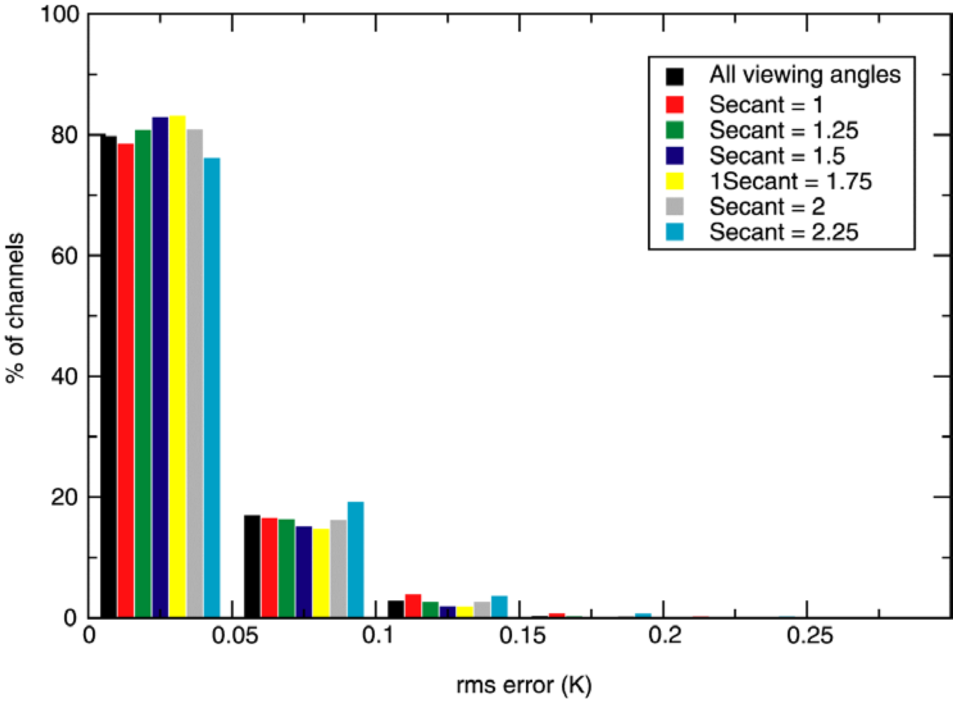

Figure 16. Histogram of the distribution of channels with rms error for six viewing angles.

It can be seen that the distribution of channels within each bin is not dramatically influenced by the viewing geometry. In fact, whatever the viewing geometry, almost 97% of the channels have rms errors less than 0.1 K.

When assessing the performance of RTIASI-4 it is useful to compare the rms error in radiance units with the radiance noise of IASI. This can give useful indications about the spectral regions where the model needs to be improved. In Fig. 17 we plot the ratio of the rms error to the IASI level 1C radiance noise. It can be seen that at least for the dependent set, the ability of the fast model to reproduce LBL radiances is such that errors introduced by the parameterization of the transmittances are below the level of detectability of IASI.

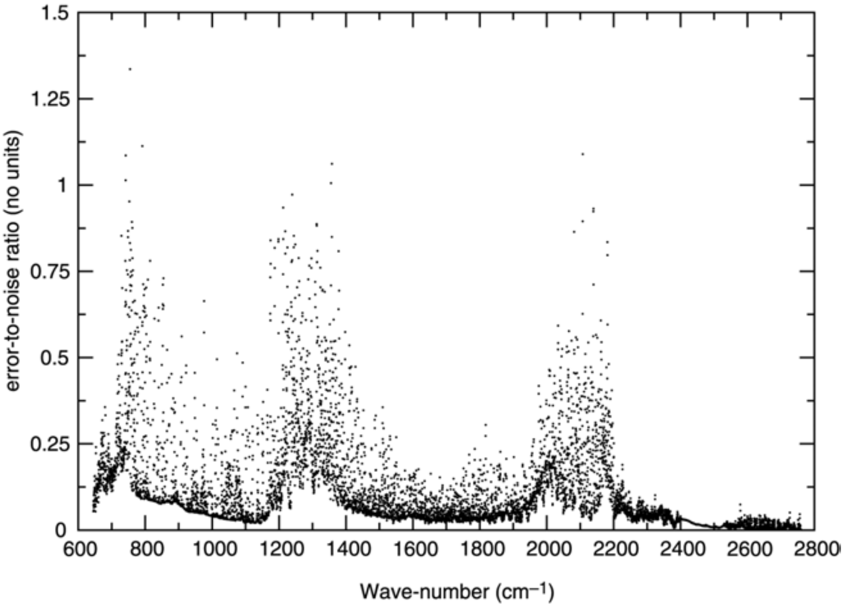

Figure 17. Error-to-noise ratio for the IASI channels for 43 diverse profiles and 6 viewing angles.

Finally, errors in the fast transmittance model for ozone have been translated into brightness temperature errors using the same approach followed for the 43 profile set. The ozone 34 profile set is now used. Only the ozone transmittance is predicted by the model. Transmittances for water vapour, fixed and trace gases are LBL computed ones for a climatological profile. Results are shown in Fig. 18 where the rms error is plotted. Values are typically less than 0.1 K with some outliers in the strong ozone band at 9.8 μm (1020 cm^{-1}). Some outliers are also present in the relatively week ozone band at 2100 cm^{-1}. The origin of larger errors for these outliers has yet to be fully understood.

To conclude this section we want to stress that radiances generated by RTIASI-4 and RTIASI-2 will differ not just because of the improved RTIASI-4 fast transmittance model (as shown in Fig. 15). A larger gain in accuracy is in fact to be expected as a result of the adoption of the finer vertical pressure grid and the use of the latest version of the HITRAN molecular database.

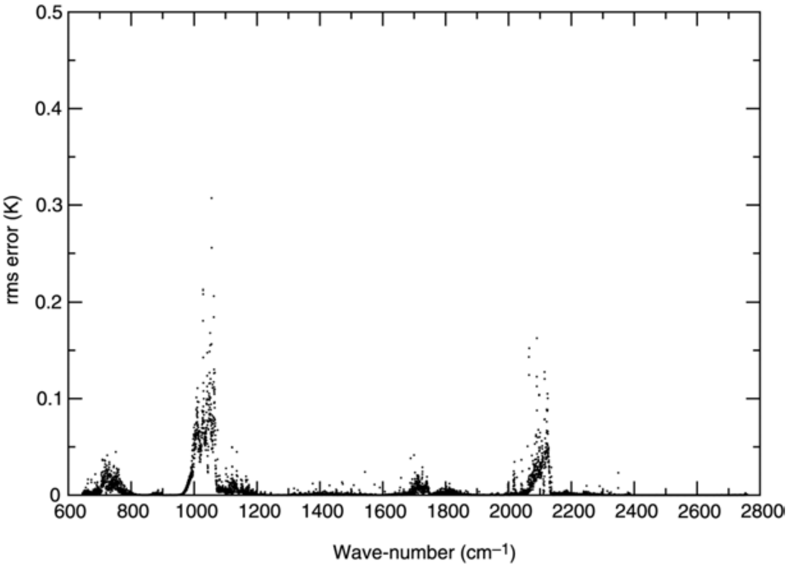

Figure 18. Root-mean-square of the difference between fast model and GENLN2 computed brightness temperatures for 34 diverse ozone profiles and 6 viewing angles.

11.2 Results for the independent set of profiles

A complete validation of the fast model requires the use of an independent set of profiles. The sampling strategy described by Chevallier et al. (2000) was used for the sampling of profiles generated from the ECMWF atmospheric model. The 13766 initial profiles were randomly sampled to select a subset of 176 profiles to be used in the training/testing of fast radiative transfer models. The dataset used here comprises 117 profiles since the profiles with low surface pressures (less that 950 hPa) were not included. Note that while temperature and specific humidity profiles are from the ECMWF model, ozone was added separately from the Fortuin and Langematz climatology (1994) depending on season and latitude. The dataset was designed to cover a wide range of temperature and water vapour profiles, which usually do not exceed the extremes included in the dependent set. For the statistical independence of the independent set, it is important that the independent set is not made of profiles that are part of the large compilation of profiles used to generate the dependent set. It should be stressed here that within the 117 profile set, concentrations for the trace gases CO_2, N_2O, CO and CH_4 are held fixed. Since independent profiles were difficult to obtain, LBL transmittances were generated assuming a constant climatological profile (the average of the 42 profiles) for these gases. Given the results obtained for the dependent set (the fast transmittance model for CO_2, N_2O, CO and CH_4 was able to reproduce LBL transmittances to an accuracy comparable to the one obtained with RTIASI-2 where these species were not variable) we expect this should not affect significantly the generality of the results. However, we plan to generate a new set of LBL transmittances when independent profiles will be available.

Uncertainties from profiles different from those used to train the fast model result in a moderate degradation in the performance of the water vapour model as shown in Fig. 19 where the maximum value of the rms of the difference between fast model and LBL transmittances is plotted. A comparison with Fig. 12 show an inflation of the error in the strong water vapour band centred at 1594 cm^{-1}. Also note that errors for the channels in the regions around 1020 cm^{-1} and 2100 cm^{-1} have now to be attributed to the ozone model.

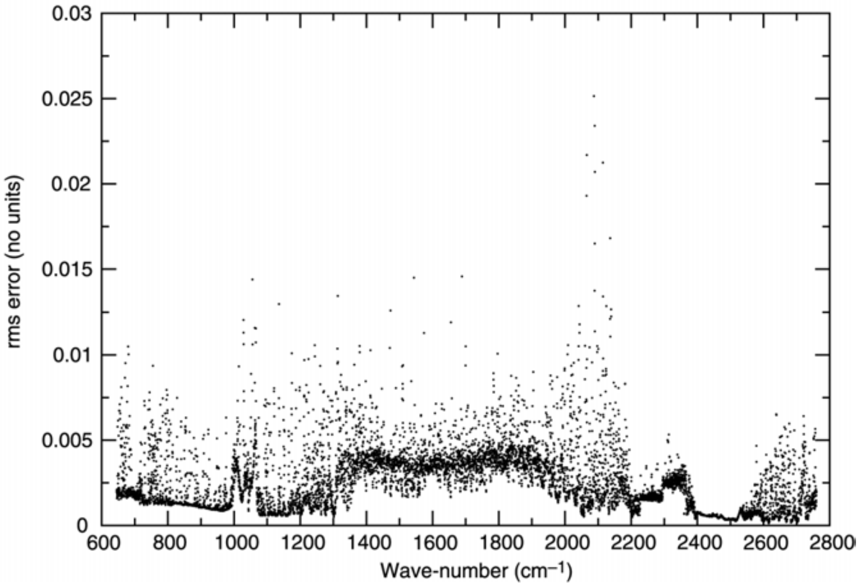

Figure 19. Maximum value of rms of the difference between fast model and GENLN2 layer-to-space transmittances for 117 independent profiles and 6 viewing angles.

The inflation of the error in the centre of the water band is to be attributed mainly to the performance of the water continuum model. This is shown in Fig. 20 where the maximum value of the difference between fast model and CDK 2.4 transmittances is plotted for the 117 profiles and six viewing angles.

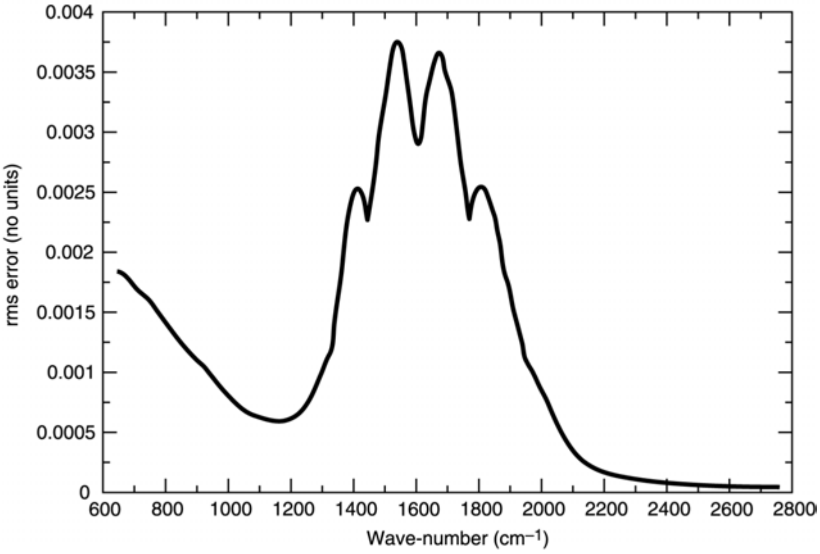

Figure 20. Maximum value of the rms of the difference between fast model and CKD 2.4 layer-to-space water vapour continuum transmittances for 43 diverse profiles and 6 viewing angles.

In the spectral region where the self-continuum is dominating, errors are comparable to those obtained for the dependent set case. In the spectral region dominated by the foreign-continuum (wave-numbers greater than 1250 cm^{-1}) errors have typically doubled with a three-fold increase in the regions contiguous to the centre of the band at 1600 cm^{-1}. As before, errors in transmittances can be translated into brightness temperature errors. These are shown in Fig. 21 where the mean value, standard deviation and rms of the difference between the fast and LBL computed radiances in units of equivalent black body brightness temperature is given for both the RTIASI-4 and RTIASI-2 models.

A comparison with Fig.15 shows that, as expected, larger errors in the fast transmittance model result in an inflation of the temperature errors in the water vapour band. Although this is true in relative terms, in absolute terms results shown in Fig. 21 still point to an overall good performance of RTIASI-4. The rms error is still below 0.15 K for 95% of the channels. Worst results are obtained for the channels where absorption for either lower atmosphere water vapour or ozone is important. In the other spectral regions, errors are only marginally worse than the ones obtained for the dependent set case. A comparison with the error score for RTIASI-2 readily assesses the much improved accuracy of the RTIASI-4 transmittance model. An almost universal improvement is achieved that is most dramatic in the 1594 cm^{-1} water vapour band and in the 11 μm (900 cm^{-1}) window region.

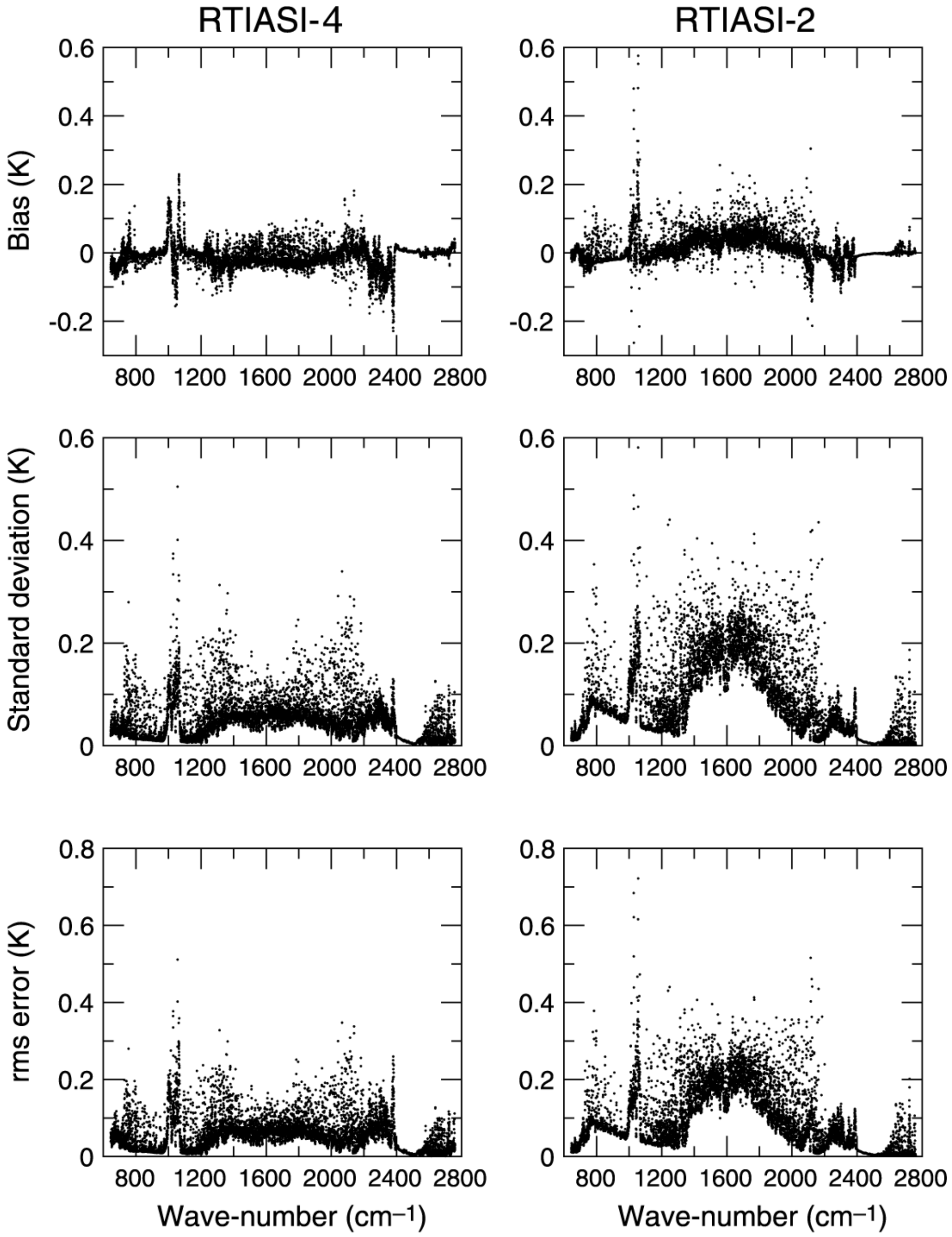

Figure 21. Mean value, standard deviation and rms of the difference between fast model and GENLN2 computed brightness temperatures for 117 diverse profiles and 6 viewing angles.

The plot of the error-to-noise ratio in Fig. 22 shows that for the vast majority of channels the error-to-noise ratio is below one. For 2% of the channels the error-to-noise ratio is greater than one and there is clearly room for improvement for these channels. They are to be found in the ozone sounding bands at 1020 cm^{-1} and 2100 cm^{-1} and in the 1300 cm^{-1} region where absorption is influenced by water vapour from lower atmospheric layers. For the outliers in the ozone sounding channels the higher errors might be explained by the fact that ozone profiles are not thermodynamically linked to the temperature profiles and this might have artificially degraded the results. However, results obtained for the dependent set in the 1020 cm^{-1} band seem to point to the need of a more accurate transmittance model. For the ozone channels in the 2100 cm^{-1} band, prediction of the ozone transmittance might be facilitated by changing the way the gases are separated out in that band (see table 4, set 9). For the water vapour channels in the 1300 cm^{-1} region a scheme might be envisaged in the future where dedicated predictors are used in this region to better account for the behaviour of the layer optical depth.

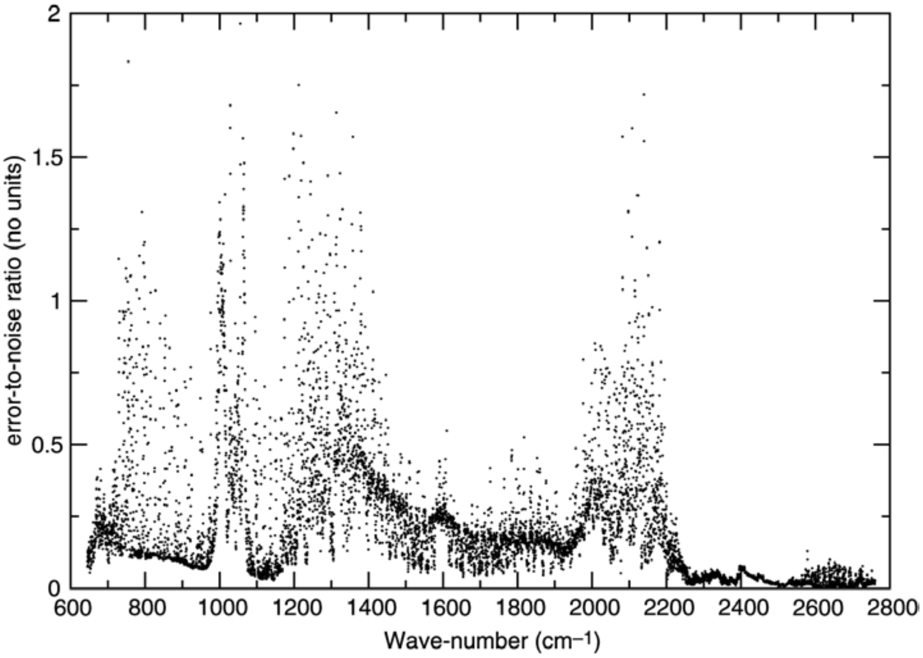

Figure 22. Error-to-noise ratio for the IASI channels for 117 diverse profiles and 6 viewing angles.

Finally, the distribution of the fitting errors as a function of viewing angle is shown in Fig 22. As observed before, the rms error is below 0.15 K for 95% of the channels. When comparing to the binned distribution for the dependent set it can be seen that almost half the number of channels inside the 0-0.05 K bin have been redistributed inside the 0.05-0.1 K bin. Also note that within the first two bins the distribution of channels with viewing angle is less regular than the one for the dependent set. For the independent set larger errors are associated with larger viewing angle geometry. However, for rms errors greater than 0.1 K the distribution of channels within the bins is scarcely influenced by the viewing geometry.

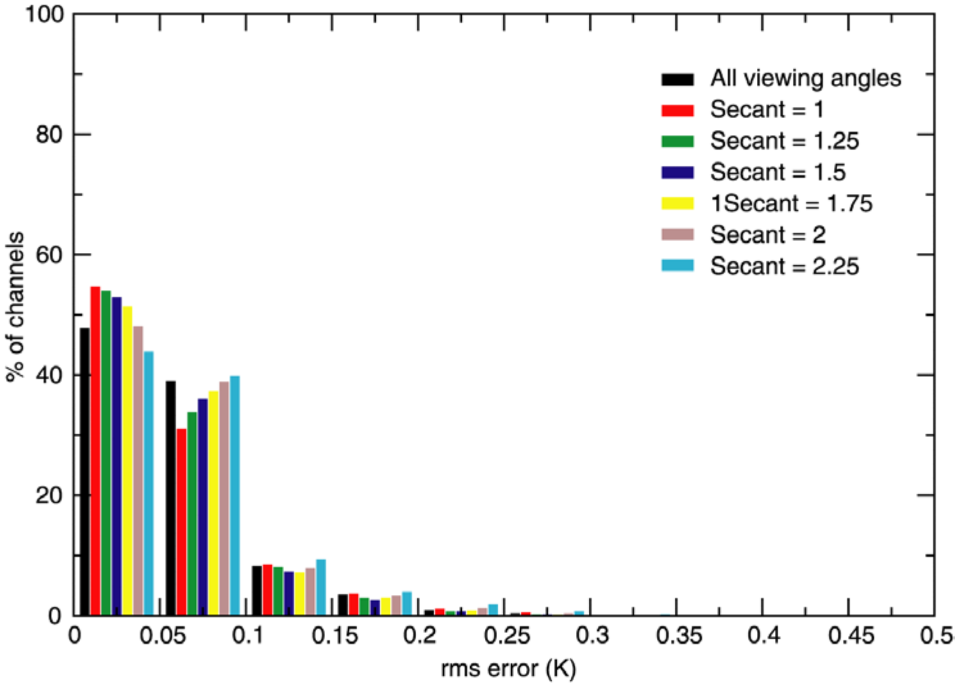

Figure 23. Histogram of the distribution of channels with rms error for six viewing angles.

12. The formulation of the model for the solar term

Equation (7) ignores the effect of solar radiance reflected by the surface. The solar radiance term comes from the solar radiance that is transmitted through the atmosphere and then partially reflected back upward through the atmosphere to the receiver. Since solar radiation gives a significant contribution to the top of the atmosphere radiance for the shorter wavelengths (<5 μm), the introduction of a solar term in RTIASI would enable the daytime assimilation of the short wave IASI channels into the 4-DVAR system.

i) Perfectly diffusing surface following the Lambert law. For a non-scattering atmosphere and in clear sky, the monochromatic radiance at the point of reflection at surface can be written as

$$L_{\tilde{\nu}}^{\uparrow}(\tau^{\downarrow},\mu,\phi)=\frac{1}{\pi}\iint_{\Omega_{\oplus}}\rho_{\tilde{\nu}}(\mu,\phi,\mu',\phi')\,\mu'\,L_{\tilde{\nu}}^{\oplus}(-\mu',\phi')\,\tau_{\tilde{\nu}}^{\downarrow}(\mu')\,d\mu'\,d\phi' \qquad (15)$$

If $\vec{U}_r(\theta,\phi)$ is the unit vector pointing toward the receiver, then $L_{\tilde{\nu}}^{\uparrow}(\tau^{\downarrow},\mu,\phi)$ is the radiance reflected upward along the direction of the unit vector $\vec{U}_r(\theta,\phi)$ where μ denotes is the cosine of the zenith angle θ and ϕ is the azimuth angle. On the right hand side of Eq. (15), $\rho_{\tilde{\nu}}$ is the bi-directional reflectance (it depends on the direction of the unit vector $\vec{U}_r(\theta,\phi)$ and on the direction of the unit vector pointing toward the source ($\vec{U}_s(\theta',\phi')$) and is generally a complex function of both), $L_{\tilde{\nu}}^{\oplus}(-\mu',\phi')$ is the solar radiance along the direction of the unit vector $\vec{U}_s(\theta',\phi')$ and $\tau_{\tilde{\nu}}^{\downarrow}(\mu')$ is the surface-to-space transmittance along the downward path through the atmosphere. Note that the integral in equation (15) has to be evaluated over the solar disk ($\Omega_{\oplus}$ is the solid angle subtended by the solar disk at the Earth).

For the case of solar radiance reflected by a land surface, a proper treatment of the solar term would then require the knowledge of the bi-directional reflectance of the considered surface. Given that the bi-directional reflectance is not currently available in RTIASI-4, we treat the reflecting surface as a perfect diffuser following the Lambert law. For a Lambertian surface the bidirectional reflectance is constant and is equal to the surface albedo ρ^L. If we assume that the direction of the centre of the sun is that of the unit vector $\vec{U}_s(\theta_{\oplus},\phi_{\oplus})$, then $L_{\tilde{\nu}}^{\oplus}(-\mu',\phi')$ is different from zero only if the vector $\vec{U}_s(\theta',\phi')$ is very close to the vector $\vec{U}_s(\mu_{\oplus},\phi_{\oplus})$. We can then write

$$L_{\tilde{\nu}}^{\uparrow}(\tau^{\downarrow},\mu,\phi)\cong\frac{1}{\pi}\rho^{L}\,L_{\tilde{\nu}}^{\oplus}(-\mu_{\oplus},\phi_{\oplus})\iint_{\Omega_{\oplus}}\mu'\,\tau_{\tilde{\nu}}^{\downarrow}(\mu')\,d\mu'\,d\phi' \qquad (16)$$

Since the solar disk occupies a very small fraction of the sky, the integrand in Eq. (16) will remain almost constant during integration over the disk and can be brought outside the integral. Equation (16) can then be written as

$$L_{\tilde{\nu}}^{\uparrow}(\tau^{\downarrow},\mu,\phi)\cong\frac{1}{\pi}\rho^{L}\,L_{\tilde{\nu}}^{\oplus}(-\mu_{\oplus},\phi_{\oplus})\,\mu_{\oplus}\,\tau_{\tilde{\nu}}^{\downarrow}(\mu_{\oplus})\iint_{\Omega_{\oplus}}d\mu'\,d\phi'=\frac{1}{\pi}\rho^{L}I_{\tilde{\nu}}^{\oplus}\,\mu_{\oplus}\tau_{\tilde{\nu}}^{\downarrow}(\mu_{\oplus}) \qquad (17)$$

where $I_{\tilde{\nu}}^{\oplus}=L_{\tilde{\nu}}^{\oplus}(-\mu_{\oplus},\phi_{\oplus})\Omega_{\oplus}$ is the irradiance of the solar disk at the top of the atmosphere. If $\tau_{\tilde{\nu}}^{\uparrow}(\mu)$ is the surface-to-space transmittance along the upward path through the atmosphere, then the reflected radiance that reaches the receiver is:

$$L_{\tilde{\nu}}(\mu) = \frac{1}{\pi}\rho^{L} I_{\tilde{\nu}}^{\oplus}\mu_{\oplus}\tau_{\tilde{\nu}}^{\downarrow}(\mu_{\oplus})\tau_{\tilde{\nu}}^{\uparrow}(\mu) \tag{18}$$

Although a perfectly diffusing surface is an extreme case, it can be used as a rough approximation for a various number of soils.

ii) *Flat water surface*. For an ideal flat water surface we have specular reflection and

$$\rho_{\tilde{\nu}}(\mu,\phi,\mu',\phi') = \delta(\mu-\mu')\delta(\phi-\phi'+\pi)\rho_{\tilde{\nu}}^{F}(\mu) \tag{19}$$

where δ is the delta Dirac function and $\rho_{\tilde{\nu}}^{F}(\mu)$ is the reflectance obtained from the Fresnel's formula:

$$\rho_{\tilde{\nu}}^{F}(\mu) = \frac{\left|\rho_{\|}\right|^{2} + \left|\rho_{\perp}\right|^{2}}{2} \tag{20}$$

$$\rho_{\|} = \frac{n\cos(\theta) - \cos(\theta^{*})}{n\cos(\theta) + \cos(\theta^{*})} \tag{21}$$

$$\rho_{\perp} = \frac{\cos(\theta) - n\cos(\theta^{*})}{\cos(\theta) + n\cos(\theta^{*})} \tag{22}$$

where n is the refractive index of water and θ^{*} is the angle of refraction obtained by Snell's law:

$$\sin(\theta^{*}) = \frac{\sin(\theta)}{n} \tag{23}$$

For a flat water surface the solar radiance that reaches the receiver can then be written as:

$$L_{\tilde{\nu}}(\mu) = \frac{1}{\pi}\rho_{\tilde{\nu}}^{F}(\mu) I_{\tilde{\nu}}^{\oplus}\mu\,\tau_{\tilde{\nu}}^{\downarrow}(\mu)\tau_{\tilde{\nu}}^{\uparrow}(\mu) \tag{24}$$

iii) *Wind roughened water surface*. A real water surface such as the ocean is roughened by the wind. However, since the radius of curvature of an ocean capillary wave is of the order of a centimetre, whereas the wavelength of infrared radiation is typically between 3 and 15 micrometers, one can regard the water surface as being locally flat and study the reflection of infrared radiation by the water surface with an approximation that uses geometrical optics. One can calculate the optical properties of the water surface (in our case the reflectivity) by first considering the reflection of light from a single mirror-like facet and then regard the water surface as a collection of all such facets, each randomly tilted with respect to the local horizon. As time passes, the tilt of a facet varies under the influence of the wind. When the open ocean reflects the solar disk, these fluctuating facets produce a dancing pattern known as sun glint. The radiance reflected by the sea surface can then be obtained using the effective reflectivity computed by taking the average of the reflectivity of the flat-water surface over the statistical variations of the surface slopes. The statistical characteristics of a wind roughened water surface are specified by the probability $P \equiv p(S_x, S_y)\, dS_x dS_y$ that a facet would have a slope within $\pm\frac{dS_x}{2}$ of S_x and $\pm\frac{dS_y}{2}$ of S_y where S_x and S_y are the slopes of the facet along the X and Y-axis of an appropriate coordinate system.

To model the reflective characteristics of a wind roughened water surface, we have followed the approach by Yoshimori et al. (1995). In this model the probability density P of the wave slope obeys a Gaussian distribution whereas the spectrum of the wave slope is specified by the Joint North Sea Wave Project

(JONSWAP) (Hasselmann et al.1973) wave-spectral model. The probability density P of the wave slope is the joint probability density of the S_x and S_y slopes and is written as

$$P(S_x, S_y) = \frac{1}{2\pi\sigma_x\sigma_y} \exp(-\frac{S_x^2}{2\sigma_x^2}) \exp(\frac{S_y^2}{2\sigma_y^2}) \tag{25}$$

where σ_x and σ_y are the mean-square slopes of S_x and S_y given by

$$\sigma_x^2 = \frac{2+\cos(2\psi)}{4} \int_0^{\infty} \Psi(\omega)[k(\omega)]^2 d\omega \tag{26}$$

$$\sigma_y^2 = \frac{2-\cos(2\psi)}{4} \int_0^{\infty} \Psi(\omega)[k(\omega)]^2 d\omega \tag{27}$$

Here, ψ is the angle that the wind direction makes with the X (along-view) axis, $k(\omega)$ is the inverse function of the dispersive relation of the full-gravity capillary wave and $\Psi(\omega)$ is the frequency spectrum of the surface wave as specified by the JONSWAP wave model. Since $\Psi(\omega)$ depends on the wind speed and on the wind fetch, the mean-square slopes σ_x and σ_y are determined by three external parameters: wind speed, wind fetch and wind direction. Note that the total variance of the slope σ_{tot}^2 is given by

$$\sigma_{tot}^2 = \sigma_x^2 + \sigma_y^2 = \int_0^{\infty} \Psi(\omega)[k(\omega)]^2 d\omega \tag{28}$$

and does not depends on the wind direction. As stated before, $k(\omega)$ is the inverse function of the dispersive relation of the full-gravity capillary wave

$$\omega(k) = \sqrt{(\frac{g}{k} + \frac{\Gamma k}{\rho}) \tanh(hk)\ k} \tag{29}$$

where g, Γ, ρ and h are the gravitational acceleration, the surface-tension constant of water, the mass density of water and the water depth. Since $\omega(k)$ cannot be inverted analytically, we have pre-computed analytically values of $k(\omega)$ for a water depth of 50 m (deep water approximation). These are stored in RTIASI-4 and used to evaluate the total variance of the surface slope, σ_{tot}, given in equation (28). The dependence of the total variance of the slope for the JONSWAP spectrum is plotted in figure 24 where a wind fetch of 40 km is assumed.

It should be noted here that since the slope variance is obtained by weighting the spectrum by $k(\omega)^2$, the wind dependence of the slope variance is a measure of the correctness of the high-wave-number spectrum. By means of optical data, Cox and Munk (1954) obtained a linear wind speed dependence for the slope variance. Since the original work of Cox and Munk, different and more complex dependencies for slopes have been obtained by various authors from radar and tank work (Jackson et al. 1992, Young 1993). Recent scanning-laser glint measurements of the sea-surface slope statistics (Shaw and Churnside 1997) suggest that the slope variance does not only depend on the wind speed but also on the stability of the marine boundary layer. Figure 24 illustrates seven curves. The red curve represents the Cox and Munk dataset. The black and green curve represent the slope variance measured by Shaw and Churnside (1997) for the case of strong negative ($T_{air} << T_{sea}$) and strong positive stability ($T_{air} >> T_{sea}$). The blue curve is a linear fit to a variety of radar altimeter and scatterometer cross section data (Apel 1994). Finally, the cyan, brown and orange curve represent the variance slope obtained from equation (28) for a depth of water of 50 m and a wind fetch of 40, 200 and 500 km. It is seen that the radar-derived slopes and the laser-derived slopes in conditions of strong positive stability are below the Cox and Munk optical values whereas the laser-derived slopes in conditions of strong negative stability are well above the Cox and Munk optical values. For large wind fetch and for wind speeds greater than 8 m/s the hydrodynamic slopes obtained from equation (28) under-estimates the remotely sensed ones. This is a direct consequence of the asymptotic behavior of the JONSWAP frequency spectrum $\Psi(\omega)$ for large ω ($\Psi(\omega)$ is proportional to ω^{-5}). It should be pointed out that the work of Donelan and Pierson (1987) and the work of Apel (1994) suggest the existence of hydrodynamic slopes that are larger than the remotely sensed ones by perhaps 100%. The use of the JONSWAP frequency spectrum seems adequate for the current use of RTIASI as a stand-alone code for research studies. However, following the implementation of RTIASI (or RTIASI derived codes) into the ECMWF Integrated Forecasting System, the use of the slope variance obtained from the ECMWF wave model could be envisaged.

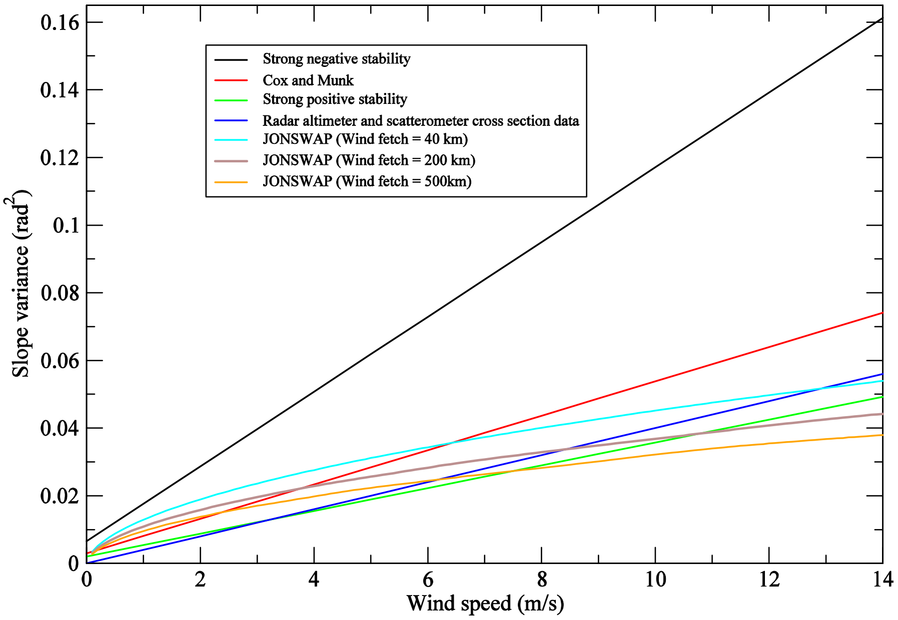

Figure 24. The dependence of the total variance of the slope on the wind speed.

An interesting feature of the model by Yoshimori et al. (1995) is that shadowing (the fact that the slopes on the back sides of the waves and deep in the troughs between waves are hidden from view) is treated explicitly and allows the estimate of the reflected solar radiance for large solar zenith angles. In principle, multiple reflections should also be included. These occur when a solar ray bounces off of several facets before reaching the receiver. Yoshimori et al. (1994) however suggest that higher-order reflection processes occur for viewing angles larger that 60°. Since the scan pattern of IASI is such that the maximum zenith angle at surface does not exceeds 58°, multiple reflection processes should not affect the effective reflectivity.To obtain the effective reflectivity, Yoshimori et al. (1995) considered the geometry of reflection of light by a tilted facet shown in figure 25.

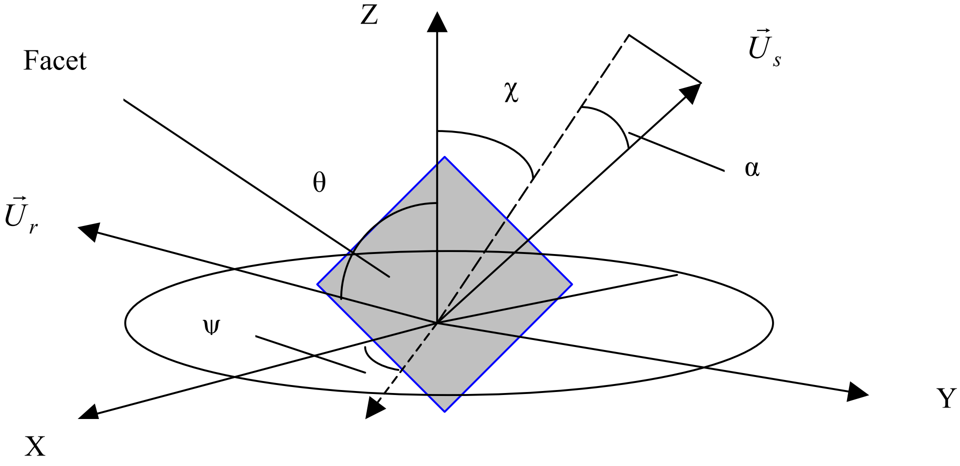

Figure 25. The geometry of reflection

The origin of the coordinate system is in the point of reflection. The tilted facet passes through the origin and the *X-Y* plane coincides with the mean sea level at the reflection point. The *X*-axis is the axis formed by the projection on the X-Y plane of the vector pointing towards the receiver, $\vec{U}_r(\theta,\phi)$. Since the *Z*-axis points towards the zenith, a right-handed system is formed. The angle χ is positive if the vector $\vec{U}_r(\theta,\phi)$ and $\vec{U}_s(\theta,\phi)$ are in opposite hemispheres, otherwise χ is negative. The angle α is positive if counted clockwise from the negative X-axis, negative is counted counter-clock wise.

Following Yoshimori et al. (1995), the radiance reflected upward along the direction of the vector $\vec{U}_r(\theta)$ can be written in terms of the effective reflectivity $w_{\tilde{\nu}}(\theta,\alpha,\chi)$ as

$$L_{\tilde{\nu}}^{\uparrow}(\tau^{\downarrow},\theta)=\int_{\Omega_{\oplus}} w_{\tilde{\nu}}(\theta,\chi,\alpha)\;\; L_{\tilde{\nu}}^{\oplus}(-\chi,\alpha)\;\; \tau_{\tilde{\nu}}^{\downarrow}(\chi)\;\; d\Omega(\chi,\alpha) \tag{30}$$

where

$$w_{\tilde{\nu}}(\theta,\chi,\alpha)=\frac{\rho_{\tilde{\nu}}^{F}\left(\frac{\chi+\theta}{2}\right)\;\left[1-\tan\left(\frac{\chi-\theta}{2}\right)\tan(\theta)\right]\frac{1}{\sqrt{2\pi c}}\exp\left(-\frac{\tan^{2}(\alpha)}{2c^{2}}\right)p_{1x}(\chi,\theta,\psi)}{2\cos^{2}(\alpha)\cos^{2}\left(\frac{\chi-\theta}{2}\right)} \tag{31}$$

$$c=\left|\cos(\chi)+\cos(\theta)\right|\,\sigma_{y} \tag{32}$$

The function $p_{1x}(\chi,\theta,\psi)$ is defined as:

$$
\begin{cases}
p_{1x}(\chi,\theta,\psi) = \dfrac{1}{\sqrt{2\pi\sigma_x}} \exp(-\dfrac{S_x^2}{2\sigma_x^2}) & \\
\times\varphi[\cot(|\theta|) - S_x \,\mathrm{sgn}(\theta)] & \theta\chi > 0 \\
\times\phi[\cot(|\chi|) + S_x \,\mathrm{sgn}(\chi)] & \\
\times Q(a,b) & \\
 & \\
p_{1x}(\chi,\theta,\psi) = \dfrac{1}{\sqrt{2\pi\sigma_x}} \exp(-\dfrac{S_x^2}{2\sigma_x^2}) & \\
\times\varphi[\cot(|\varsigma|) - S_x \,\mathrm{sgn}(\varsigma)] & \theta\chi \le 0 \\
\times Q(d) &
\end{cases}
\tag{33}
$$

where

$$\varphi(\gamma) = \begin{cases} 1 & \gamma \ge 0 \\ 0 & \gamma < 0 \end{cases} \tag{34}$$

$$Q(a,b) = \frac{1}{1+\Lambda(a)+\Lambda(b)} \tag{35}$$

$$\Lambda(\gamma) = \frac{1}{\sqrt{2\pi}\gamma} \exp(-\frac{\gamma^2}{2}) - \frac{1}{2} erfc(\frac{\gamma}{\sqrt{2}}) \tag{36}$$

$$a = \frac{\cot(|\vartheta|)}{\sigma_x} \tag{37}$$

$$b = \frac{\cot(|\chi|)}{\sigma_x} \tag{38}$$

$$\chi = \theta + 2\tan(S_x) \tag{39}$$

$$\varsigma = \max(|\theta|,|\chi|) \tag{40}$$

$$Q(d) = \frac{1}{1+\Lambda(d)} \tag{41}$$

$$d = \frac{\cot(|\varsigma|)}{\sigma_x} \tag{42}$$

The function $\varphi(\gamma)$ represents the first order shadowing effect (i.e. the facets on the back of the waves are excluded because they cannot contribute to the reflected radiance) whereas the function $Q(a,b)$ represents the second order shadowing effect (i.e. the facets deep in the trough of the wave are masked by the front of the wave).

In Eq. (31) the angle α can take arbitrary large values. However the theory developed by Yoshimori et al. (1995) is based on the assumption that the cross-view slope σ_y is small compared to the along-view slope σ_x. In this approximation the incidence angle χ of and the viewing angle θ are related by the law of reflection. Although this is accurate only for small values of the slope Sy, one should note that the main contribution to the effective reflectivity comes from those facets whose slope is near the mean-square slope given by equations (26) and (27). For large values of the slope S_y, the magnitude of the effective reflectivity is negligible and thus the theory can be considered adequate for arbitrary values of the angle α.

We can introduce an approximate form of Eq. (30) by making the same assumptions used to derive Eq.(18):

$$L_{\tilde{\nu}}(\theta) \cong w_{\tilde{\nu}}(\theta, \chi^{\otimes}, \alpha^{\oplus}) \; L_{\tilde{\nu}}^{\oplus} \; \Omega_{\oplus} \; \tau_{\tilde{\nu}}^{\downarrow} \; \tau_{\tilde{\nu}}^{\uparrow} \qquad (43)$$

The departure from the exact values given by Eq(30) is negligible unless the zenith angle of both the receiver and the sun are close to the horizon (Zeisse 1995). One should mention that given the viewing geometry of IASI, this is never going to be the case.

If for the purpose of illustration we set $\rho_{\tilde{\nu}}^{F}(\frac{\theta+\chi}{2}) = 1$, $\tau_{\tilde{\nu}}^{\downarrow} = 1$ and $\tau_{\tilde{\nu}}^{\uparrow} = 1$, we can plot the ratio of glint radiance leaving the surface to solar radiance arriving at the surface, $\frac{L_{\tilde{\nu}}(\theta)}{L_{\tilde{\nu}}^{\oplus}}$, as a function of the angle θ and for a number of different configurations for a wind speed of 7 m/s.

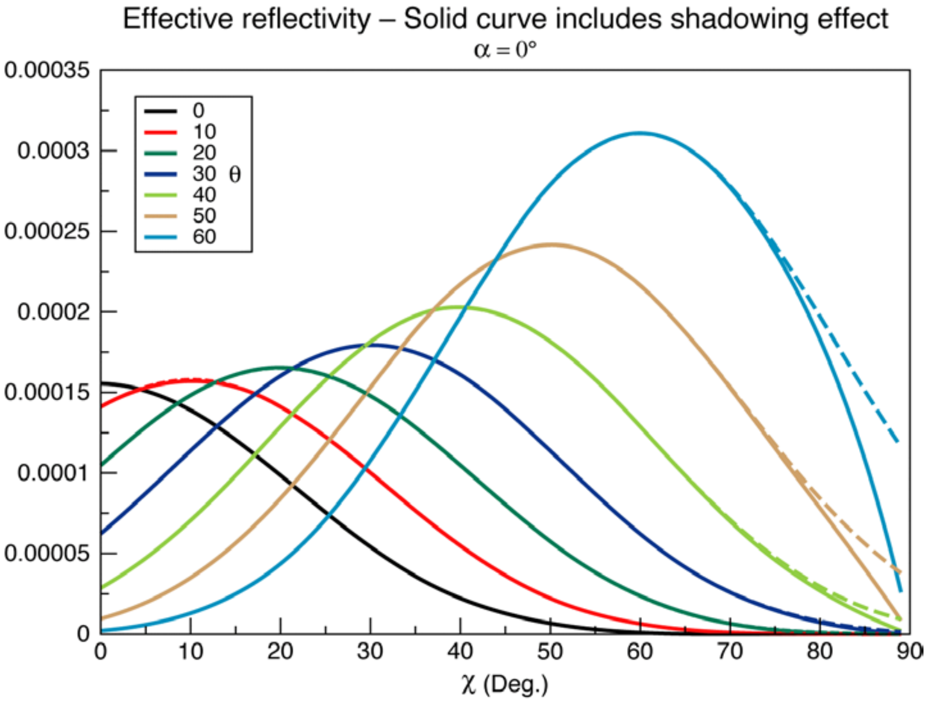

Figure 26. The effective reflectivity for: α=0°; ψ=0°.

In figure 26 the angle α is set equal to zero (i.e. the vector $\vec{U}_r(\theta,\phi)$ and $\vec{U}_s(\theta,\phi)$ are in the same X-Z vertical plane). It is evident that as the viewing angle θ increases, the distribution of the glint ratio become narrow and the peak of the distribution become large. Also shown in figure 26 is the effect of shadowing (solid curve). It can be seen that shadowing become important for solar zenith angles larger than 75° and results in a decrease of the glint ratio as a consequence of the fact that facets deep in the trough of the wave are hidden from view.

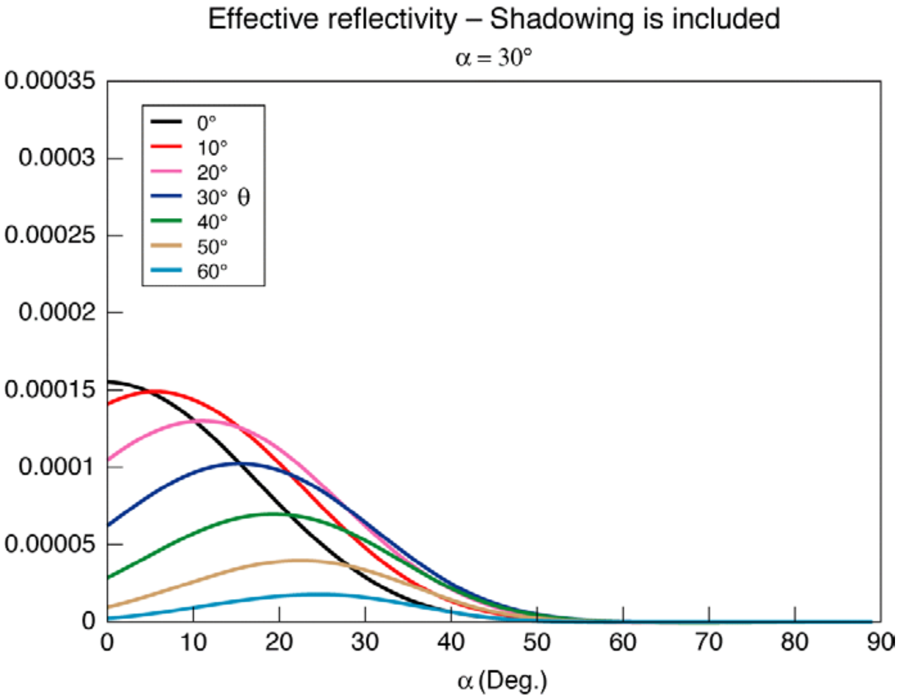

Figure 27. The effective reflectivity for: α=30°; ψ=0°.

In figure 27 the angle α has been set equal to 30°. Since for this geometry only the facets with a non zero cross-view slope, $S_{y,}$ contribute to the reflected radiance, the values of the glint ratio are now significantly smaller and the peak of the distribution is large for small viewing angles. Finally, figure 28 illustrates the change in the distribution of the glint ratio as a consequence of the difference of the corresponding mean-square slope resulting from a shift of the wind direction (from 0° to 90°).

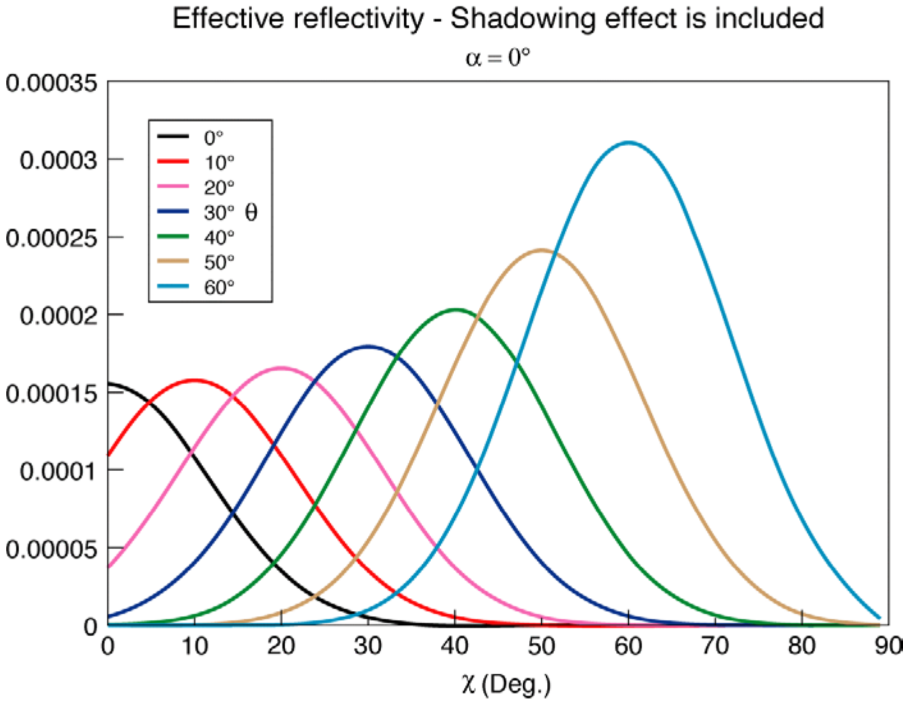

Figure 28. The effective reflectivity for: α=0°; ψ=90°.

13. Implementation of the solar term in RTIASI

The solar source function $I_{\tilde{\nu}}^{\oplus}$ used in RTIASI-4 is based on theoretical radiative transfer calculations for the solar atmosphere made by Kurucz (1992). In the spectral region of interest for IASI, it is strongly dependent on measurements made by the ATMOS instrument on the Space Shuttle. In figure 29 the source function $I_{\tilde{\nu}}^{\oplus}$ is shown for the spectral interval considered in RTIASI-4 to be affected by solar radiation.

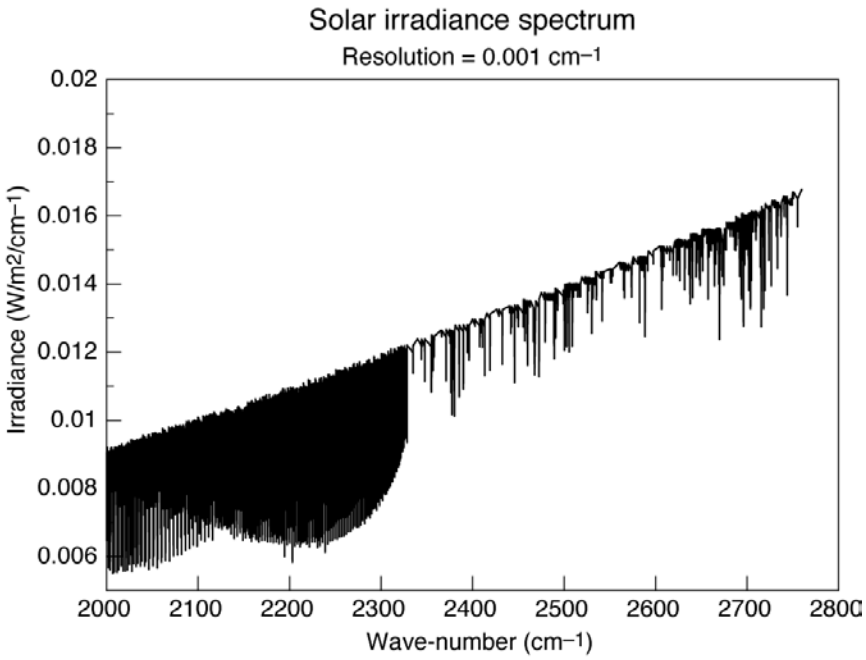

Figure 29. The solar irradiance spectrum used in RTIASI-4.

The integration of $I_{\tilde{\nu}}^{\oplus}$ gives a total irradiance (solar constant) equal to 1368.6 Wm^{-2}. This is the value for the mean Sun-Earth distance. However, the solar constant varies on short and long- time scales for instance due to the development or decay of sunspots or due to the variation of the Sun-Earth distance. No attempt was made in RTIASI-4 to model this variability. Rather, a custom value of the solar constant can be introduced and the solar irradiance spectrum scaled accordingly.

Equations (18), (24) and (43) give the monochromatic solar radiance that reaches the detector. To represent the solar radiance as viewed by IASI, the spectrum of monochromatic radiances given by these equations must be convolved with the appropriate spectral response function. One can write

$$\hat{L}_{\tilde{\nu}^*}^{\uparrow}(\mu,\phi) = \int_{-\infty}^{+\infty} L_{\tilde{\nu}}^{\uparrow}(\mu,\phi)\, f(\tilde{\nu}^* - \tilde{\nu})\, d\tilde{\nu} \qquad (44)$$

where $f(\tilde{\nu}^* - \tilde{\nu})$ is the normalised spectral response function, $\tilde{\nu}^*$ is the central wave number of the IASI channel and the circumflex over the symbol denotes convolution.

The process of convolving the monochromatic radiances is too time-consuming to be performed in real time. In RTIASI-4 the convolved monochromatic radiance is approximated with the radiance computed using the convolved transmittances (polychromatic approximation). This approximation is already used in RTIASI-4 (and in general in all the regression based fast radiative transfer models) to evaluate the radiance emitted by the surface and by the atmosphere (emitted and reflected term) and was found to introduce errors typically well below the instrument noise (Matricardi and Saunders, 1999). In what follow we will study the errors introduced by the polychromatic approximation for the case when the transmittance along the downward path differs from the one on the upward path and for the case when the atmosphere is the same along both paths through the atmosphere.

13.1 The solar term when the atmosphere along the downward path is different from the atmosphere on the upward path

For the case of solar radiance reflected for instance by a wind roughened water surface, the polychromatic form of the solar term is:

$$\hat{L}^{\uparrow}_{\tilde{\nu}^*} \cong \hat{I}_{\tilde{\nu}^*}{}^{\oplus} \quad w_{\tilde{\nu}}(\theta,\alpha^{\oplus},\chi^{\oplus}) \quad \hat{\tau}_{\tilde{\nu}^*}{}^{\uparrow}(\mu) \quad \hat{\tau}_{\tilde{\nu}^*}{}^{\downarrow}(\mu_{\oplus}) \tag{45}$$

A fundamental difference to the polychromatic form of the radiative transfer equation used in RTIASI-4 to evaluate the surface and atmospheric contribution is the presence in equation (45) of the product of convolved transmittances. In the spectral regions where the transmittance is a rapidly varying function of wave number, one would expect the convolution of the product of the transmittances to differ sensibly from the product of the single transmittances convolved individually. To check the accuracy of Eq.(45) we have first computed top of the atmosphere radiances for a number of representative atmospheric profiles ignoring the effect of reflected solar radiance. We have then added the solar term in its exact and approximated form by using equations (44) and (45) respectively. All the computations have involved (when applicable) the use of line-by-line generated quantities. The trials were carried out for three different air mass types. For each air mass type we have chosen two slightly different atmospheric profiles chosen among the 43 used to train RTIASI. One profile was used along the upward path whereas the other was used along the downward path. The air mass type considered was tropical, mid-latitude and arctic. In figure 30 we show the difference between exact and approximated radiances for the tropical air mass (top panel), the mid-latitude air mass (centre panel) and the arctic air mass (bottom panel). The geometry of reflection is the one that gives the maximum sun glint ratio. (i.e. θ=60°, χ=60° and α=0°). The wind speed is 7 ms^{-1}. Results show that the polychromatic approximation for the solar term can be very crude. In the spectral regions where we expect the solar radiance to give a contribution (2000cm^{-1}<$\tilde{\nu}$<2250cm^{-1}; 2380cm^{-1}<$\tilde{\nu}$<2760cm^{-1}) differences can be as large as 6K. Since the solar term varies linearly with the sun glint ratio, the lower the sun glint ratio the lower the error. We have computed radiances for a number of different reflection geometries (results are not shown here) and found that unless the contribution of the solar radiance is reduced to very small values, errors are still typically of the order of a few K. It is interesting to see from figure 30 that the structure of the error is clearly correlated with the air mass type. For instance, in the spectral region where the solar radiance gives the maximum contribution (2380cm^{-1}<$\tilde{\nu}$<2760cm^{-1}) the error is larger for the very warm and moist tropical profiles and smaller for the very dry and cool arctic profiles. This is a direct consequence of the fact that the tropical profile is characterized by the presence of relatively strong water vapour lower altitude absorption lines whereas in this spectral region the arctic profile is almost transparent to radiation.

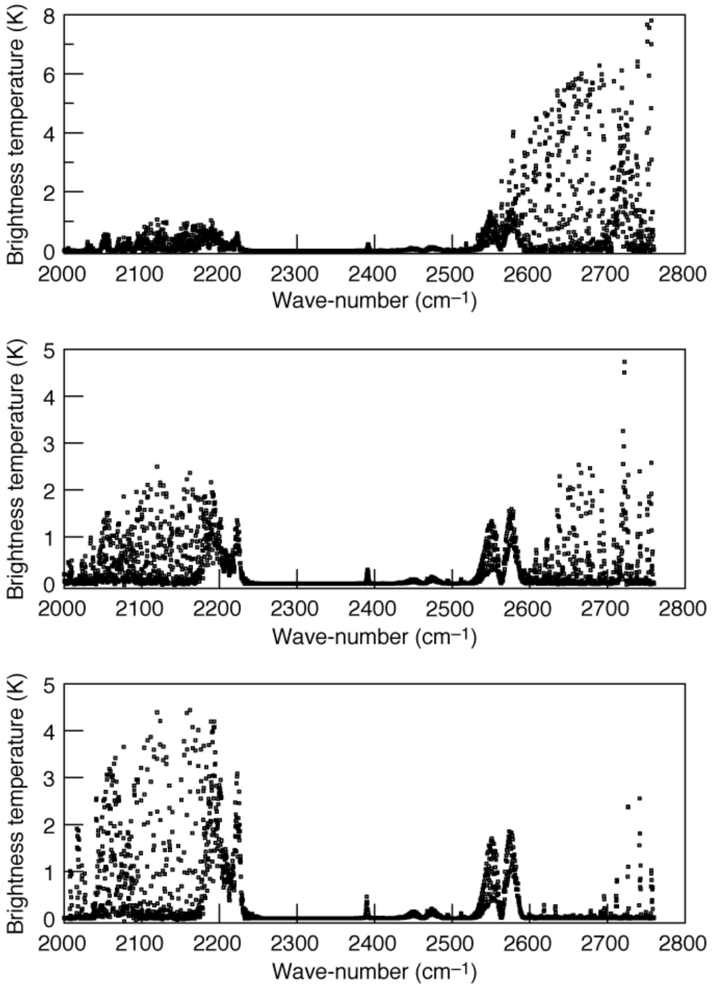

Figure 30. The polychromatic form of the solar term: the difference between exact and approximated radiances for a tropical profile (top panel); mid-latitude profile (centre panel); arctic profile (bottom panel).

13.2 The solar term when the atmosphere is the same along the downward and upward path

We have seen in section 13.1 that the implementation of an accurate polychromatic form of equation (43) is not easy in a fast radiative transfer model. One should note however that if we assume that atmosphere is the same along both downward and upward paths through the atmosphere, the product of the monochromatic transmittances $\tau_{\tilde{\nu}}^{\downarrow}(\mu_{\oplus})\tau_{\tilde{\nu}}^{\uparrow}(\mu)$ can be written as

$$\tau_{\tilde{\nu}}^{\downarrow}(\mu_{\oplus})\tau_{\tilde{\nu}}^{\uparrow}(\mu) = \tau_{\tilde{\nu}}(\mu_{eff}) \tag{46}$$

where

$$\frac{1}{\mu_{eff}} = \frac{1}{\mu} + \frac{1}{\mu_{\oplus}} \tag{47}$$

this is equivalent to say that the reflected solar radiance depends on a single transmittance whose secant is equal to the sum of the secants of the viewing and solar zenith angles. Equation (43) can then be written as

$$L_{\tilde{\nu}}(\theta) \cong w_{\tilde{\nu}}(\theta,\chi^{\otimes},\alpha^{\oplus})\ L_{\tilde{\nu}}^{\oplus}\ \ \Omega_{\oplus}\ \ \tau_{\tilde{\nu}}(\mu_{eff}) \tag{48}$$

The polychromatic form of the solar then becomes

$$\hat{L}^{\uparrow}_{\tilde{\nu}^*} \cong \hat{I}_{\tilde{\nu}^*}^{\oplus} \quad w_{\tilde{\nu}^*}(\theta,\alpha^{\oplus},\chi^{\oplus}) \quad \hat{\tau}_{\tilde{\nu}^*}(\mu_{eff}) \tag{49}$$

The form of Eq. (49) is similar to the one used to evaluate the radiance emitted from the surface. The main difference is that $\hat{I}_{\tilde{\nu}^*}^{\oplus}$ replaces the Planck function $B(T_s,\tilde{\nu}^*)$ as source function and $\tau_{\tilde{\nu}^*}(\mu_{eff})$ replaces $\tau_{\tilde{\nu}^*}^{\uparrow}(\mu)$ (also note that in Eq.(31) we can use the value of $\rho^F_{\tilde{\nu}}$ at the central wave number of the IASI channel, $\tilde{\nu}^*$. This does not introduce any significant error since the variation of $\rho^F_{\tilde{\nu}}$ with wave number is very slow). If $\hat{I}_{\tilde{\nu}^*}^{\oplus}$ would vary slowly compared to the spectral response function, we would expect the error introduced by the polychromatic approximation to be small (Matricardi and Saunders 1999). However, given the fine structure present in the solar spectrum used in RTIASI-4 (see figure 31 for details), we have to assess how much important this is for IASI.

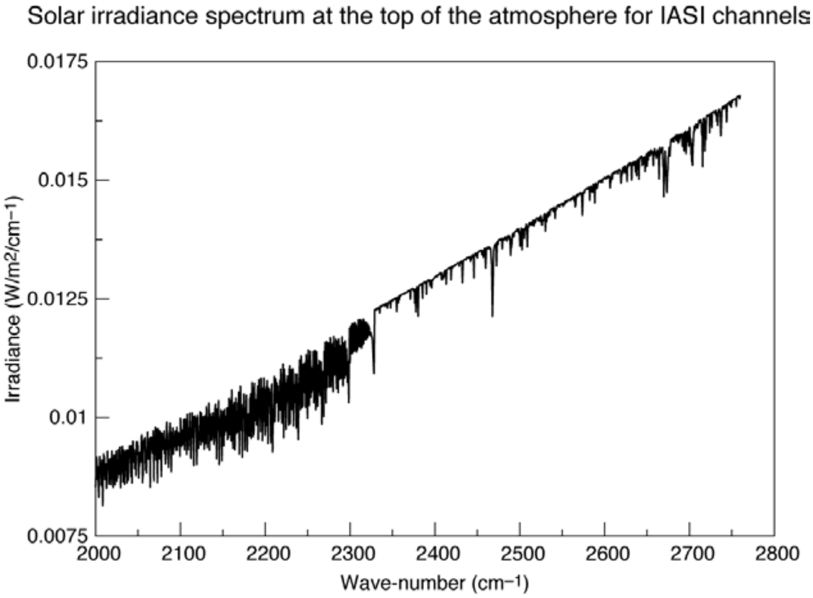

Figure 31. The convolved solar irradiance spectrum.

As for Eq. (43), we have assessed the accuracy of the polychromatic approximation for Eq. (48) by comparing exact and approximated line-by-line radiance for the three different air mass types. The profiles are the same described above. The only difference is that the profiles along the downward and upward paths are the same. For each profile, results are shown in figures 32 through 34 for three different reflection geometries: θ=0°, χ=0°, α=0° (top panel); θ=30°, χ=30°, α=0° (centre panel) and θ=60°, χ=60°, α=0° (bottom panel). The wind speed is 7 ms^{-1}.

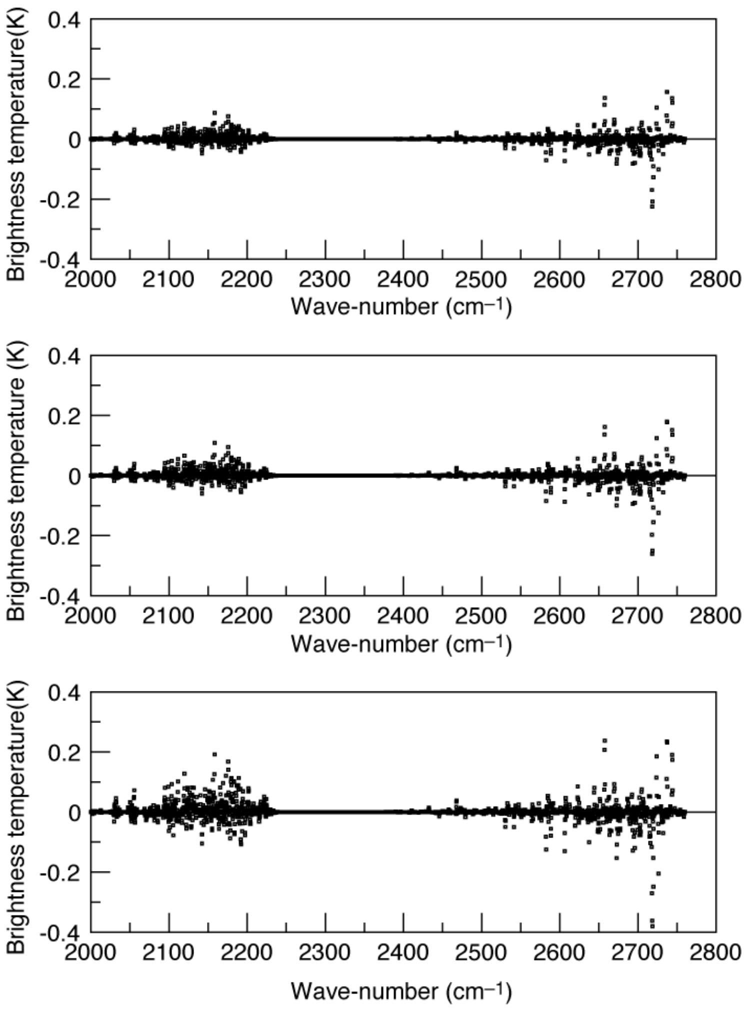

Figure 32. The polychromatic form of the solar term: the difference between exact and approximated radiances for the tropical profile. The top panel denotes θ=0°, χ=0°, α=0°; the centre panel denotes θ=30°, χ=30°, α=0°; the bottom panel denotes θ=60°, χ=60°, α=0°.

Figure 32 shows results for the tropical profile. The error introduced by the polychromatic approximation is typically less than 0.1 K for the vast majority of the channels. Only a few outliers show an error in excess of 0.1 K. Errors are slightly larger for large values of the angle θ and χ when more solar radiance is reflected by the surface. Results for the mid-latitude and arctic profile are shown in figures 33 and 34 respectively. In the spectral region $2380\,cm^{-1} \leq \tilde{\nu}^{*} \leq 2760\,cm^{-1}$ the polychromatic approximation is still very accurate. Errors are well below 0.1K and are correlated with the air mass type (i.e. errors are smaller for colder and dryer atmospheres where the absence of water vapour lower altitude absorption lines tends to mitigate the polychromatic approximation). A somewhat lesser accuracy is observed in the spectral region $2000\,cm^{-1} \leq \tilde{\nu}^{*} \leq 2250\,cm^{-1}$ above all for the dry and cold arctic profile. Two factors contribute to this behaviour. Firstly as the temperature and moisture content decrease, the peak of the weighting functions move closer to the surface and render the atmosphere more transparent to the solar radiance reflected by the surface (i.e. the amount of reflected solar radiance is larger, hence the error). Secondly, the polychromatic approximation is rendered less accurate by the fine spectral features of the solar irradiance spectrum (see figure 31).

Results shown in figures 32 to 34 have to be considered as an upper limit to the error. In fact the sun glint ratio is strongly dependent on the angle α. A tilt of the vertical plane that contains the vector $\vec{U}_s(\theta,\phi)$ results in a sharp decrease of the reflected solar radiance, hence the error, above all for a reflection geometry where the angle θ and χ are large (i.e. for this configuration only the facets with large cross-view slopes, S_y, can reflect the solar beam toward the receiver).

If we assume that these results can be generalised to the class of air mass type to which each of the considered profiles is part, then we can conclude that the polychromatic approximation can be considered adequate for the case when the atmosphere along both the upward and downward path is the same. This assumption relies on the fact that in the current NWP models no ray tracing is performed in the atmosphere. The vertical profile of temperature and atmospheric constituents is the one for the grid point at the footprint. In the event that vertical profiles were made available along the downward and upward path, one could still made good use of Eq.(49).

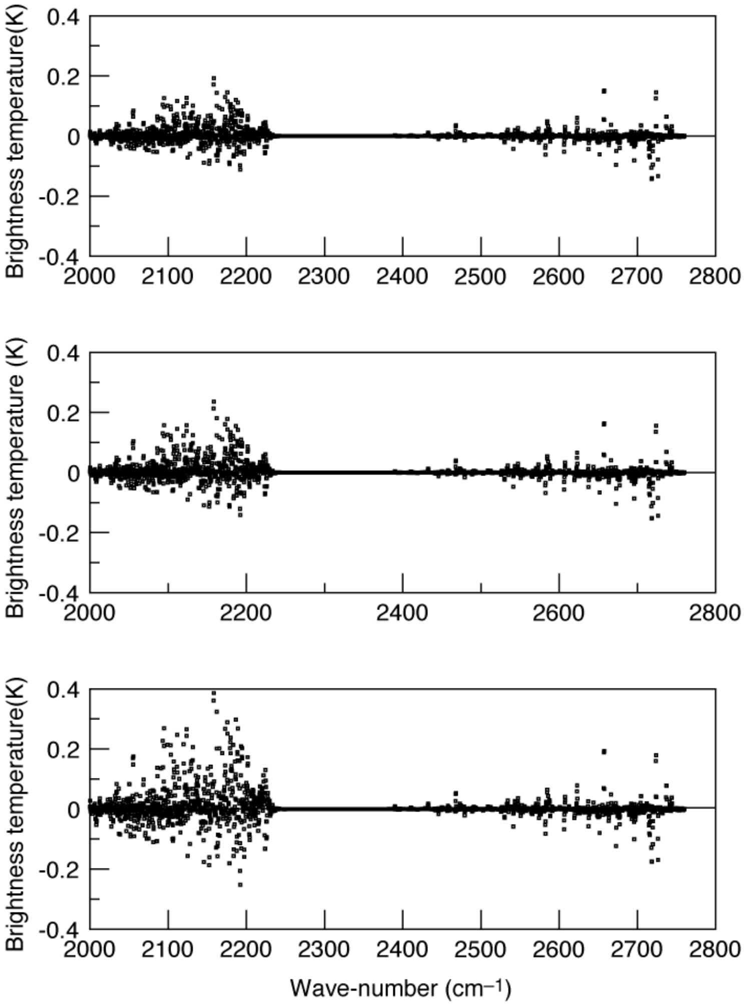

Figure 33. The polychromatic form of the solar term: the difference between exact and approximated radiances for the mid-latitude profile. The top panel denotes θ=0°, χ=0°, α=0°; the centre panel denotes θ=30°, χ=30°, α=0°; the bottom panel denotes θ=60°, χ=60°, α=0°.

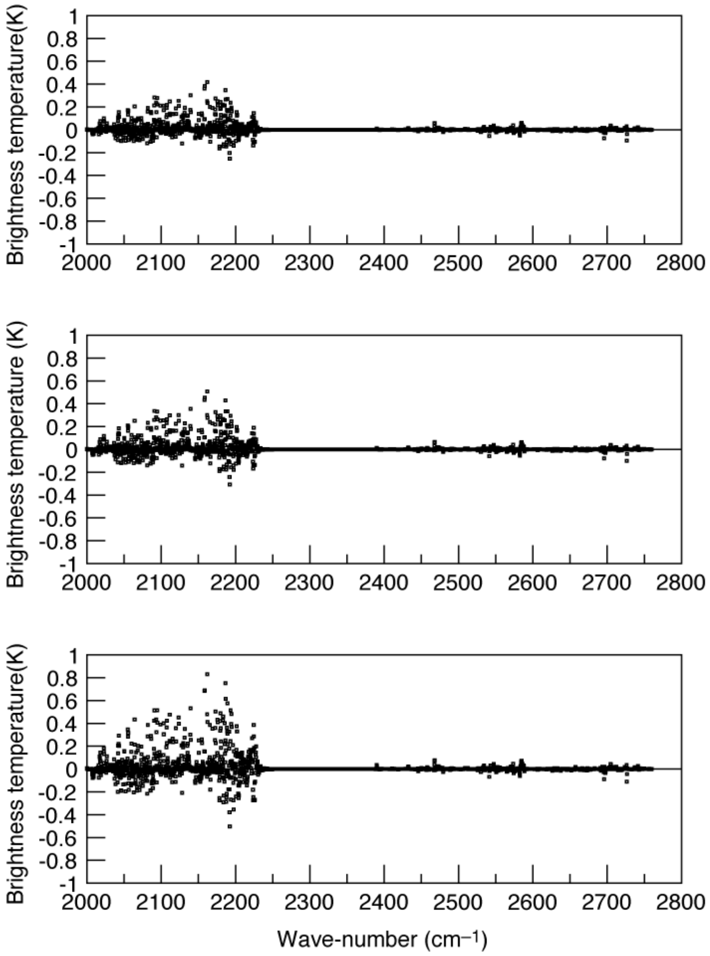

Figure 34. The polychromatic form of the solar term: the difference between exact and approximated radiances for the arctic profile. The top panel denotes θ=0°, χ=0°, α=0°; the centre panel denotes θ=30°, χ=30°, α=0°; the bottom panel denotes θ=60°, χ=60°, α=0°.

In figure 35 we have sketched the geometry of reflection for θ=57°, χ=57°, α=0° (a zenith angle θ=57 ° corresponds to the maximum viewing angle of the IASI instrument). For the pressure grid adopted in RTIASI-4 (the pressure of the bottom level is 1050 hPa and the pressure of the top level is 0.005 hPa) the thickness of the atmosphere (the segment $\overline{AE}$ in figure 35) is typically of the order of 80 km or less. For pressures less than 0.005 hPa the atmosphere is considered to be transparent and no absorption is taking place. If we consider the length of the segment $\overline{BD}$ to be of the same order as the horizontal resolution of the grid of the NWP model ($\cong$40 km) then the length of the segment $\overline{AC}$ is $\cong$13 km. The atmosphere along the segment $\overline{AB}$ and $\overline{AD}$ can thus considered be the same. For the paths that from the point B and D proceed to the top of the atmosphere, we have in principle to consider different atmospheres. For the profiles we have used to assess the accuracy of the polychromatic approximation, a length of the segment $\overline{AC}$ of the order of 13 km corresponds to a pressure of $\cong$200 hPa for the tropical profile, $\cong$170 hPa for the mid-latitude profile and $\cong$130 hPa for the arctic profile. One should note that for the channels that are most influenced by the presence of the reflected solar radiance ($2380\,cm^{-1} \le \tilde{\nu}^{*} \le 2760\,cm^{-1}$), the weighting functions peak at considerably higher pressures. Thus, in principle, we do expect that differences between the atmosphere along the paths that from the point B and D proceed to the top of the atmosphere should not have a significant impact on the solar term.

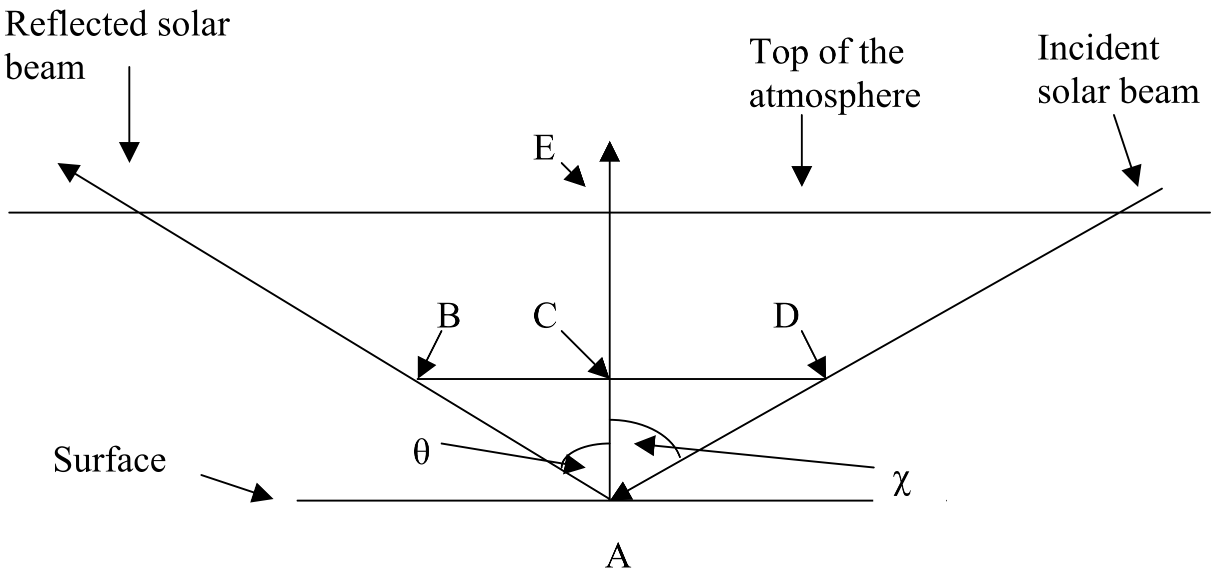

Figure 35

We have tested this hypothesis by computing line by-line radiances (*R1)* for the tropical, mid-latitude and arctic profile considered above assuming that the profile along the downward and upward path is the same. For pressure values less than the value correspondent to the height of 13 km, each of the profiles along the downward path (solar path) was then replaced with a different profile of the same air mass type. Radiances *R2* were then computed for this new profile configuration. In both cases the solar term is included. The difference (*R1-R2)* is shown in figure 36 for the tropical, mid-latitude and arctic profile respectively.

For the three profiles the accuracy of the approximation is fairly accurate in the spectral range $2380\,cm^{-1} \le \tilde{v}^* \le 2760\,cm^{-1}$ where apart from a limited number of outliers, errors do not exceed 0.2 K. For wave numbers $2000\,cm^{-1} \le \tilde{v}^* \le 2250\,cm^{-1}$ worst results are observed above all for the arctic profile. One should note here that the geometry of reflection chosen for this exercise is the one for which, as long as $\chi \le \theta$, the length of the segment $\overline{BD}$ is maximum. For any other geometry that involves smaller angles θ and χ, the length of the segment $\overline{BD}$ would be smaller than the resolution of the horizontal grid of the NWP model. Consequently, the altitude range for which the atmosphere along the downward and upward path can be considered the same is increased and so is the accuracy of the approximation. If $\chi > \theta$, one can still find a large number of angles θ and χ for which the length of the segment $\overline{BD}$ is smaller than the resolution of the NWP model. This is no longer true if χ is much larger than θ. However, a configuration where θ is much larger than χ would see the sun glint ratio (and consequently the reflected solar radiance) to decrease dramatically above all if the sun is moving away from the X-Z plane (i.e. α is different from zero).

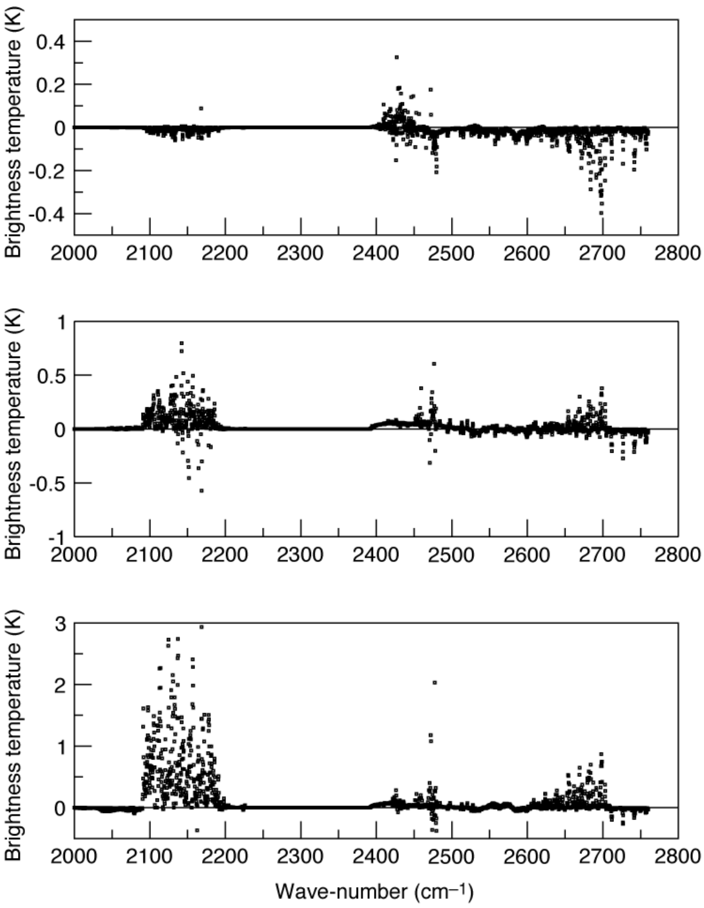

*Figure 36. The difference (*R1-R2*) for the tropical profile (top panel), mid-latitude profile (centre panel) and arctic profile (bottom) panel.*

All the arguments discussed above are based on the assumption that the resolution of the model is $\cong 40$ km. A higher resolution would reduce the range of applicability of the approximation and thus a more thorough study (that is outside the time frame of this study) should be carried out to obtain a suitable form of equation (43) that could be used in a fast radiative transfer model.

Finally, we want to note that in RTIASI-4, the solar term can be evaluated using either Eq(45) or Eq(49).

14. The fast transmittance model for the shortwave channels in presence of solar radiation

Given the wide range of solar zenith angles, the computation of either $\hat{\tau}_{\tilde{\nu}}^{\downarrow}(\mu_{\oplus})$ or $\hat{\tau}_{\tilde{\nu}}(\mu_{eff})$ requires the evaluation of transmittances at zenith angles considerably larger than the ones involved in the computation of top of the atmosphere radiances in absence of solar radiation. The standard fast transmittance model used in RTIASI-4 can accurately simulate transmittances for zenith angles less then 64º. For the fast transmittance model to be able to simulate transmittances for a wider range of zenith angles, we have extended the database of line-by-line transmittances by computing data for an additional number of eight more path angles, namely, the angles for which the secant assumes the following values: 2.58, 3.04, 3.72, 4.83, 6.1, 7.2, 9, 12. This extended range allows evaluating the solar term for zenith angles as large as $\approx 85°$. The additional database of line-by-line transmittances was generated using the methods described in sections 2 and 9 only for the shortwave channels ($\tilde{\nu} \geq 2000\,cm^{-1}$).

The large range of zenith angles (or secants) increases the difficulty of fitting the line-by-line optical depths. We have computed regressions coefficients for the larger range of secants using the standard RTIASI-4 predictors (see tables 5,6 and 7). Results show that the level of accuracy attainable by using this set of predictors is such that they are not adequate to be used in a context where large secants are involved. We have then formulated a revised set of predictors to be used in the shortwave range only. The new predictors do not differ dramatically from the standard ones. Predictors were added or replaced and/or added depending on the molecular species. For fixed gases optical depths we have added two predictors to the standard set so that we now use 10 predictors. For water vapour optical depths the predictors varies depending on the spectral region. In the spectral region $2000\,cm^{-1} \leq \tilde{v}^* \leq 2250\,cm^{-1}$ we use a total of 15 predictors. This is the same number of predictors used in RTIASI-4 although the revised set features four different predictors. We did the same in the spectral region $2380\,cm^{-1} \leq \tilde{v}^* \leq 2760\,cm^{-1}$ where we now use a total of 15 predictors. Four new predictors have replaced four of the old predictors and two more predictors have been added to model the dependence of the water vapour optical depth on the methane layer amount. The predictors for CO_2 optical depths also depend on the spectral region and we now use a maximum number of 14 predictors obtained by adding two predictors and replacing two of the old ones. For N_2O optical depths we use 12 predictors obtained from the old set by replacing one predictor and adding two ones. For CO optical depths we also use 12 predictors obtained from the old set by replacing one predictor and adding two new ones. Finally, 13 predictors are used for ozone. The new set has been obtained by replacing two of the old predictors and by adding two new predictors. For CH_4 and water vapour continuum optical depths we did not apply any change to the old set of predictors. Methane has a relatively weak band in the shortwave region and we found that the accuracy of the regression is not compromised by the use of the old predictors. The water vapour continuum coefficients depend linearly on the secant since the regression is made for monochromatic transmittances. This means that the predictors implicitly explain large part of the optical depth variability deriving from the larger set of secants so that the old predictors can be satisfactory be retained (see table 2). The new set of predictors for the shortwave channels ($2000\,cm^{-1} \leq \tilde{v}^* \leq 2760\,cm^{-1}$) are tabulated in tables 9, 10, 11. The definition of the profile variables used in the predictors can be found in table 8. In the spectral regions were we did not consider the effect of reflected solar radiance, the standard RTIASI-4 predictors are used (tables 5, 6 and 7).

Predictor	**Fixed gases**	**CO_2**	**O_3**
$X_{j,1}$	$\sec(\theta)$	$\sec(\theta)\, CO2_r(j)$	$\sec(\theta)\, O_r(j)$
$X_{j,2}$	$\sec^2(\theta)$	$T_r^2(j)$	$\sqrt{\sec(\theta)\, O_r(j)}$
$X_{j,3}$	$\sec(\theta)\, T_r(j)$	$\sec(\theta)\, T_r(j)$	$\dfrac{\sec(\theta) O_r(j)}{O_w(j)}$
$X_{j,4}$	$\sec(\theta)\, T_r^2(j)$	$\sec(\theta)\, T_r^2(j)$	$(\sec(\theta)\, O_r(j))^2$
$X_{j,5}$	$T_r(j)$	$T_r(j)$	$\sqrt{\sec(\theta)\, O_r(j)}\, \delta T(j)$
$X_{j,6}$	$T_r^2(j)$	$\sec(\theta)\, T_w(j)$	$\sec(\theta)\, O_r^2(j)\, O_w(j)$
$X_{j,7}$	$\sec(\theta)\, T_{fw}(j)$	$(\sec(\theta)\, CO2_w(j))^2$	$\dfrac{O_r(j)}{O_w(j)} \sqrt{\sec(\theta\, O_r(j)}$
$X_{j,8}$	$\sec(\theta)\, T_{fu}(j)$	$\sec(\theta)\ T_w(j) \sqrt{T_r(j)}$	$(\sec(\theta)\ O_w(j))^{1.75}$
$X_{j,9}$	$\sec(\theta)\ \ T_r^3$	$\sqrt{\sec(\theta) CO2_r(j)}$	$O_r(j) \sec(\theta) \sqrt{O_w(j) \sec(\theta)}$
$X_{j,10}$	$\sec(\theta)\ \ \sqrt{\sec(\theta) T_r(j)}$	$T_r^3(j)$	$\sec(\theta)\, O_w(j)$
$X_{j,11}$	0	$\sec(\theta)\ T_r^3(j)$	$(\sec(\theta)\, O_w(j))^2$
$X_{j,12}$	0	$\sec(\theta)\ T_r^2(j)\ T_w^3(j)$	$\sqrt{\sec(\theta)}\ O_w^2(j)\ \delta T(j)$
$X_{j,13}$	0	$(T_r(j)\ T_w(j))^2$	$\sec(\theta) T_r^3(j)$

For channels $\in$ ***[5421,6601]***

$X_{j,14}$ $\qquad$ $\sec(\theta)\, CO_r(j)$

Table 9. Predictors used in RTIASI-4 for Fixed gases, CO_2 and ozone channels in the shortwave region of the spectrum

Predictor	**CO**	**N_2O**	**CH_4**
$X_{j,1}$	$\sec(\theta)\,CO_r(j)$	$\sec(\theta)\vert\,N2O_r(j)$	$\sec(\theta)\vert\,CH4_r(j)$
$X_{j,2}$	$\sqrt{\sec(\theta)\,CO_r(j)}$	$\sqrt{\sec(\theta)\,N2O_r(j)}$	$\sqrt{\sec(\theta)\,CH4_r(j)}$
$X_{j,3}$	$\sec(\theta)\,CO_r(j)\,\delta T(j)$	$\sec(\theta)\,N2O_r(j)\,\delta T(j)$	$\sec(\theta)\,CH4_r(j)\,\delta T(j)$
$X_{j,4}$	$(\sec(\theta)\,CO_r(j))^2$	$(\sec(\theta)\,N2O_r(j))^2$	$(\sec(\theta)\,CH4_r(j))^2$
$X_{j,5}$	$\sqrt{\sec(\theta)\,CO_r(j)}\,\delta T(j)$	$N2O_r(j)\,\delta T(j)$	$CH4_r(j)\,\delta T(j)$
$X_{j,6}$	$\sqrt[4]{\sec(\theta)\,CO_r(j)}$	$\sqrt[4]{\sec(\theta)\,N2O_r(j)}$	$\sqrt[4]{\sec(\theta)\,CH4_r(j)}$
$X_{j,7}$	$\sec(\theta)\,CO_r(j)\,\delta T(j)\left\vert\delta T(j)\right\vert$	$\sec(\theta)\,N2O_w(j)$	$\sec(\theta)\,CH4_{tw}(j)$
$X_{j,8}$	$\dfrac{\sec(\theta)\,CO_r^2(j)}{CO_w(j)}$	$\sec(\theta)\,N2O_{tw}(j)$	$CH4_{tw}(j)$
$X_{j,9}$	$\dfrac{\sqrt{\sec(\theta)\quad CO_r(j)}\quad CO_r(j)}{CO_w(j)}$	$(\sec(\theta)\quad N2O_{tw}(j))^2$	$(\sec(\theta)\,CH4_w(j))^2$
$X_{j,10}$	$\dfrac{\sec(\theta)\,CO_r^2(j)}{\sqrt{CO_w(j)}}$	$\dfrac{\sqrt{\sec(\theta)\,N2O_r(j)}\,N2O_r(j)}{N2O_w(j)}$	$\sec(\theta)\,CH4_w(j)$
$X_{j,11}$	$(\sec(\theta)\,CO_{tw}(j))^{0.4}$	$(\sec(\theta)\quad N2O_{tw}(j))^3$	$\dfrac{\sqrt{\sec(\theta)\,CH4_r(j)}\,CH4_r(j)}{CH4_w(j)}$
$X_{j,12}$	$(\sec(\theta)\,CO_{tw}(j))^{0.25}$	$\sec(\theta)^2 N2O_{tw}(j)\,\delta T(J)$	

For channels $\in$ ***[5421,6601]***

$X_{j,13}$	$\sec(\theta)\,CO_r(j)$
$X_{j,14}$	$\sec(\theta)^2\,CO_r(j)\,CO_w(j)$

Table 10. Predictors used in RTIASI-4 for CO, N_2O and CH_4 channels in the shortwave region of the spectrum.

Predictor	**H2O**	**H2O**	**H2O**
$X_{j,1}$	$(\sec(\theta)W_r(j))^2$	$(\sec(\theta)W_r(j))^2$	$(\sec(\theta)W_r(j))^2$
$X_{j,2}$	$\sec(\theta)W_w(j)$	$\sec(\theta)W_w(j)$	$\sec(\theta)W_w(j)$
$X_{j,3}$	$(\sec(\theta)W_w(j))^2$	$(\sec(\theta)W_w(j))^2$	$(\sec(\theta)W_w(j))^2$
$X_{j,4}$	$\sec(\theta)W_r(j)\,\delta T(j)$	$\sec(\theta)W_r(j)\,\delta T(j)$	$\sqrt{\sec(\theta)W_r(j)}$
$X_{j,5}$	$\sqrt{\sec(\theta)W_r(j)}$	$\sqrt{\sec(\theta)W_r(j)}$	$\sqrt{\sec(\theta)W_r(j)}$
$X_{j,6}$	$\sqrt[4]{\sec(\theta)W_r(j)}$	$\sqrt[4]{\sec(\theta)W_r(j)}$	$\sqrt[4]{\sec(\theta)W_r(j)}$
$X_{j,7}$	$\sec(\theta)W_r(j)$	$\sec(\theta)W_r(j)$	$\sec(\theta)W_r(j)$
$X_{j,8}$	$(\sec(\theta)\ W_w(j))^{1.5}$	$(\sec(\theta)\ W_w(j))^{1.5}$	$(\sec(\theta)\ W_w(j))^{1.5}$
$X_{j,9}$	$(\sec(\theta)\ W_r(j))^{1.5}$	$(\sec(\theta)\ W_r(j))^{1.5}$	$(\sec(\theta)\ W_r(j))^{1.5}$
$X_{j,10}$	$\sec(\theta)W_r(j)\,\delta T(j)\lvert\delta T(j)\rvert$	$\sec(\theta)W_r(j)\,\delta T(j)\lvert\delta T(j)\rvert$	$(\sqrt{\sec(\theta)W_r(j)})\,\delta T(j)$
$X_{j,11}$	$(\sqrt{\sec(\theta)W_r(j)})\,\delta T(j)$	$(\sqrt{\sec(\theta)W_r(j)})\,\delta T(j)$	$(\sec(\theta)\ W_w(j))^{1.25}$
$X_{j,12}$	$(\sec(\theta)\ W_w(j))^{1.25}$	$(\sec(\theta)\ W_w(j))^{1.25}$	$(\sec(\theta)\,W_r(J))^{1.5}\ \delta T(j)$
$X_{j,13}$	$(\sqrt{\sec(\theta)\ W_r(j)})\ W_r(j)$	$(\sqrt{\sec(\theta)\ W_r(j)})\ W_r(j)$	$\dfrac{\sec(\theta)\,W_r^2(j)}{W_w(j)}$
$X_{j,14}$	$\sec(\theta)\,CO2_r(j)$	0	$(\sec(\theta)\,CH4_r(J))^{1.25}$
$X_{j,15}$	$\sec(\theta)\,CO_r(j)$	0	$(\sec(\theta)\,CH4_r(J))^{1.25}\ \delta T(j)$
	Channels $\in$ ***[5421,6601]***	***Channels*** $\in$ ***[6602,6860]***	***Channels*** $\in$ ***[6861,8461]***

Table 11. Predictors used in RTIASI-4 for Water vapour (line absorption) channels in the shortwave region of the spectrum.

It should be noted here that when the solar term is included, the transmittance computation in equation (7) and, for instance, in equation (45), has to be performed using the same transmittance model (i.e. the one that uses dedicated predictors in the shortwave). Thus the statistics of the error shown in figure 15 is no longer valid and has to be recomputed using the shortwave model. To assess the accuracy of the fast transmittance model in the shortwave, we have compared radiances obtained by using fast model and line-by-line transmittances in equation (7) (for ease of comparison we are considering the top of the atmosphere radiance generated by the emission of the surface and by the emission/absorption of the atmosphere system; no solar term is included). Radiance errors in units of equivalent black body brightness temperatures are shown in figure 37 where the viewing geometry involves the six angles used to derive the standard regression coefficients in RTIASI-4. The 43 profiles of the dependent set were used. In the top panel we have plotted the root mean square error for the case where the standard RTIASI-4 predictors are used (same as in the bottom left panel of figure 15) whereas in the bottom panel we have plotted the root mean square error for the case where dedicated predictors are used in the shortwave. In the spectral region $2250\,cm^{-1} \le \tilde{\nu}^{*} \le 2380\,cm^{-1}$ the standard RTIASI-4 predictors are used in both cases since in this region there is no contribution from the solar radiance.

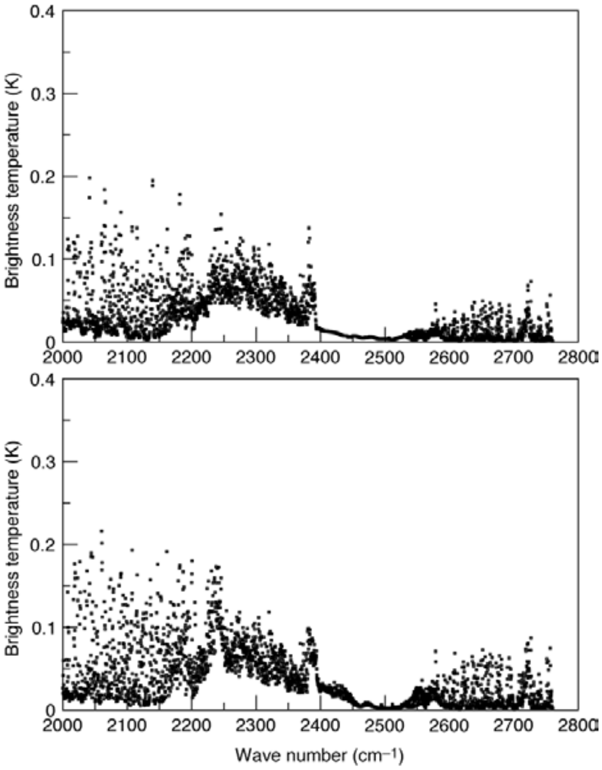

Figure 37. The root mean square of the difference between fast model and GENLN2 computed brightness temperatures for 43 profiles and six viewing angles. The standard RTIASI-4 fast transmittance model is used in the top panel; the RTIASI-4 shortwave fast transmittance model is used in the bottom panel.

Figure 37 shows that when the dedicated fast transmittance model is used in the shortwave, despite the fact that for this model the regression coefficients have been obtained from the fit of line-by-line optical depths for a very large range of zenith angles, the accuracy of the model is comparable to the accuracy of the standard fast transmittance model used in RTIASI-4 for which regression coefficients have been obtained from the fit of line-by-line optical depths for a limited range of zenith angles. Slightly worse results are only observed in the spectral regions where water vapour absorbing lines are present (i.e. $\tilde{\nu}$<2200 cm^{-1} and $\tilde{\nu}$>2600 cm^{-1}).

To assess the accuracy of the fast model in presence of solar radiation, we have included the solar term and compared radiances obtained from using fast model and line-by-line transmittances (equation (45) was used for the solar term with $\tau_{\tilde{\nu}}^{\downarrow}(\mu_{\oplus})\tau_{\tilde{\nu}}^{\uparrow}(\mu)=\tau_{\tilde{\nu}}(\mu_{eff})$; i.e. the atmosphere along the downward and upward path was considered to be the same). The statistics of the error has been obtained by first computing fast model and line-by-line radiances with no solar term for the 43 dependent profiles for each of the 6 standard viewing angles (the angle θ in figure 25). Then for each profile and for each of the six standard viewing angles we have added the solar term for a viewing geometry where the solar zenith angle (the angle χ in figure 25) assumes each of the 13 values used in the computation of the regression coefficients. Thus the instrument zenith angle at surface assumes values from 0° to 64° whereas the solar zenith angle at the surface assumes values from 0° to 85°. Results are shown in figure 38 for a configuration where α=0° (top panel) and α=30° (bottom panel).

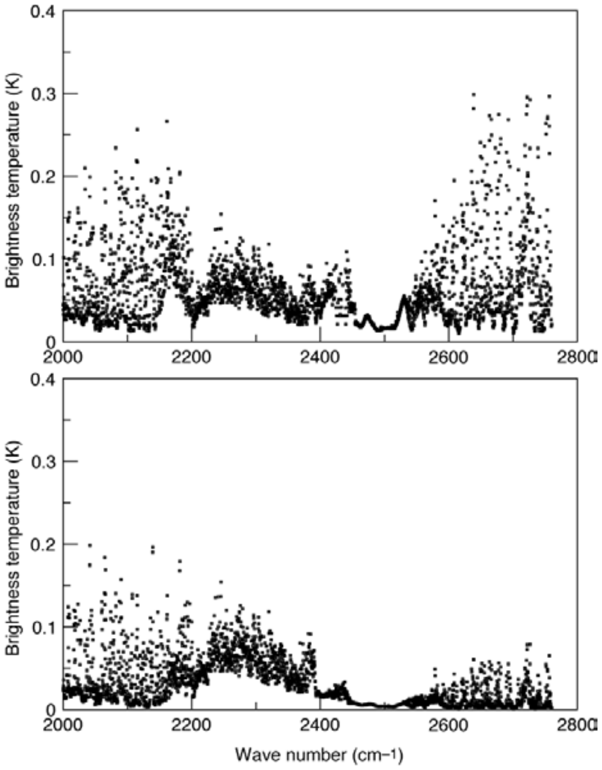

Figure 38. The root mean square of the difference between fast model and GENLN2 computed brightness temperatures for the 43 dependent profiles. The solar term is included. Results in the top panel are for α=0°. Results in the bottom panel are for α=30°

As expected, an increase of the error is observed in the spectral region where the solar radiance gives the maximum contribution ($\tilde{\nu}$>2380 cm^{-1}). In this spectral range, for some profiles the contribution of the solar term can be in excess of 80 K. In the spectral region $\tilde{\nu}$<2250 cm^{-1} the contribution of the solar term is more than one order of magnitude smaller and no inflation of the error is observed. Errors decrease dramatically for the configuration where α=30°. In this case less solar radiance is reflected towards the detector (for large zenith angles there is no reflected solar radiance at all) and since the solar term depends linearly on the sun glint ratio, smaller errors are obtained.

15. The evaluation of the local path angle

The larger range of zenith angles involved in the computation the solar term does also have implications on the way the layer optical depths are evaluated in RTIASI-4. In the fast transmittance model the angular dependence of the optical depths is generally addressed by scaling the predictors through the secant of the local path angle. In principle the satellite viewing angle (or the solar zenith angle) should be converted into a local path angle that decreases with altitude because of the curvature of the Earth and its surrounding atmosphere. This effect is largest at the maximum IASI viewing angle or at the maximum solar zenith angle and is currently ignored in RTIASI-3.2 where the IASI viewing angle is converted into the local path angle at surface and used throughout the atmosphere. The dependence of the local path angle on altitude has been explicitly introduced in RTIASI-4 by considering the geometry of the situation and the bending of rays as they traverse the atmosphere. The atmospheric layers are considered as concentric rings. If we trace a ray across these rings at any angle other than nadir, the local zenith angle relative to the outward radial direction at the point of intersection will be different at each ring because due the curvature of the Earth and to atmospheric refraction. The local zenith angle at the bottom of each layer can be computed according to Snell's law

$$c = n(h)\, h \sin(\theta) \tag{50}$$

where c is a constant through the layer, θ is the local path angle at the bottom of the layer, h is the height of the bottom of the layer and $n(h)$ is the index of refraction of air at height h. For a ray travelling along the upward path (the direction of the vector $\vec{U}_r(\theta)$) the sine of the local path angle at the bottom of layer j can then be written as

$$\sin(\theta_j) = \sin(\theta_{sat}) \frac{R_{earth} + H_{sat}}{R_{earth} + h_j} \frac{n_{top}}{n_j} \tag{51}$$

where θ_{sat} is the IASI viewing angle at the satellite point, R_{earth} is the radius of the Earth for a given latitude, H_{sat} is the altitude of the satellite, the height of the bottom of layer j, n_j is the index of refraction of air through layer j and n_{top} is the index of refraction of air at the top of the atmosphere (0.005 hPa). For a ray travelling along the downward path (the direction of the vector $\vec{U}_s(\chi,\alpha)$) we can write that the sine of the local path angle at the bottom of layer j is

$$\sin(\chi_j) = \sin(\chi_s) \frac{R_{earth}}{R_{earth} + h_j} \frac{n_s}{n_j} \tag{52}$$

where χ_s is the solar zenith angle at surface and n_s is the index of refraction of air at surface.

Ray tracing in the Earth's atmosphere requires the knowledge of the height of the pressure levels. In RTIASI-4 the height of pressure levels h_j is computed by integration of the hydrostatic equation between two adjacent levels

$$\int_{p_j}^{p_{j+1}} \frac{dp}{\rho_m(p)} = \int_{h_j}^{h_{j+1}} g(h)\, dh \tag{53}$$

where $\rho_m(p)$ is the density of moist air and $g(h)$ is the value of gravity as a function of altitude. In RTIASI-4, $g(h)$ is evaluated using the inverse-square law of gravitation

$$g(h) = g_L \left(\frac{R}{R+h}\right)^2 \tag{54}$$

where R is the radius of the Earth and, for a given latitude, g_L is the value of Earth's gravity at surface obtained by use of the international gravity formula (Woollard 1979). The density of moist air $\rho_m(p)$ is written as

$$\rho_m(p) = \rho(p)\frac{[M_a(10^6 - m_w) + M_w m_w]}{10^6 M_a} \tag{55}$$

where $\rho(p)$ is the density of dry air, M_a is the molecular weight of air, M_w is the molecular weight of water and m_w is the water vapour volume mixing ratio in units of parts by million volume. In deriving equation (55) we have implicitly assumed that the partial pressure of water vapour can be written as

$$p_w = p\, m_w\, 10^{-6} \tag{56}$$

Finally, for an ideal gas, we can write $\rho(p)$ as

$$\rho(p) = \frac{p\, M_a\, 10^{-1}}{R\, T(p)} \tag{57}$$

where $T(p)$ is the temperature of air and R is the molar gas constant. We have evaluated the impact that a variable local path has on the top of the atmosphere radiances by using RTIASI-4 in two different modes. Firstly, radiances (RT4_1) were computed by assuming a constant path angle (as done in RTIASI-3.2) for six different IASI viewing angles and 117 profiles. Additional radiances (RT4_2) were then computed assuming a variable path angle (as done in RTIASI-4) for the same configuration of six viewing angles and profiles. The root mean square of the difference (RT4_1-RT4_2) is shown in figure 39. It can be seen that as expected, differences are larger for large viewing angles. Also, the greater discrepancies are observed in correspondence of those IASI channels whose weighting functions peak higher in the atmosphere. For some profiles the inaccuracy introduced by assuming a constant path angle can be as large as 0.45K.

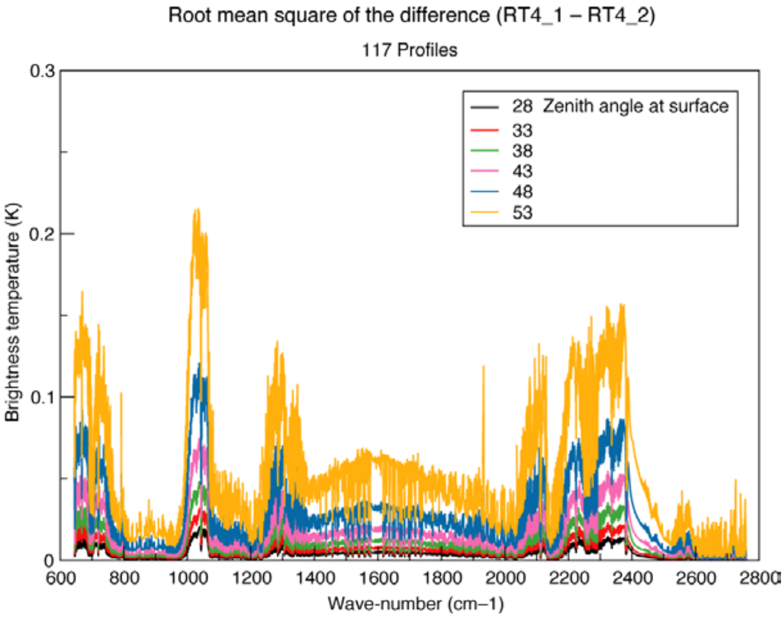

*Figure 39. The difference (*RT4_1-RT4_2*).* RT4_1 *is the RTIASI-4 radiance obtained by assuming a constant path angle.* RT4_2 *is the RTIASI-4 radiance obtained by assuming a variable path angle. The statistics is computed for 117 profiles and 6 scan angles.*

For the typical atmospheric paths involved in the viewing geometry of a nadir-sounding instrument, the effect of atmospheric refraction is very small and can usually be neglected. However, in RTIASI-4 we have retained the capability of performing a ray tracing through the atmosphere since this feature might be useful in future developments when RTIASI could serve as a skeleton to develop a fast radiative transfer model for limb sounding instruments for which atmospheric refraction is important.

16. Conclusions

An improved version of RTIASI (RTIASI-4), the ECMWF fast radiative transfer model for IASI, has been developed.

The accuracy of the LBL spectra on which the RTIASI-4 fast transmittance model is based has been improved by including 4 more molecules in the LBL computations (HNO3, CCl4, CF_4 and OCS) and by using the year 2000 release of the HITRAN molecular database. By using a revised set of water vapour training profiles in the stratosphere, the condition of the regression has been improved so that unphysical oscillations observed in the RTIASI-2 stratospheric water vapour Jacobians have been virtually eliminated. The updated RTIASI-4 features a revised vertical pressure grid that allows the integration of the radiative transfer equation to be performed with significantly increased accuracy. The water vapour transmittance model has been significantly improved by weighting the data prior to performing the regression and by introducing a dedicated transmittance model for the continuum absorption. Minor adjustments to the predictors for water vapour have also been made. RTIASI-4 can now handle variable CO_2, N_2O, CO ,CH_4 and a solar term has been introduced to evaluate the solar radiance reflected by a land or water surface in a non-scattering atmosphere.

Results for the dependent set of profiles used to train the fast model show that RTIASI-4 can reproduce LBL radiances to a degree of accuracy that is below the instrumental noise for virtually all the simulated IASI channels. In absolute terms, the rms of the difference between simulated and LBL radiances is below 0.1 K for 97 % of the channels. Larger errors (less than 0.2 K) are observed for a small fraction of channels where absorption due to water vapour from lower atmospheric layers is important. The statistics of the error for a set of profiles independent to the regression coefficients shows (in relative terms) a moderate degradation of the performance in the strong 6.7 μm water vapour band to be attributed mainly to the water continuum model. In absolute terms, the rms error is still below 0.15 K for 95% of the channels with outliers in the ozone sounding bands and in the spectral regions where absorption form lower atmospheric layers water vapour takes place. For 98% of the channels the radiance rms error is still below the instrumental noise. For the independent set a slight dependence of the error on the viewing geometry is observed for the channels that display rms errors less than 0.1K: larger errors are associated with larger viewing angle geometry. However, for channels with rms errors greater than 0.1K there is no significant dependence of the error on the viewing geometry. In terms of errors, results for RTIASI-4 and the previous version of the code, RTIASI-2, shows the much-improved accuracy achieved by use of the revised transmittance model for water vapour. Errors in the centre of the 1594 cm^{-1} water vapour band and in the 11 μm (900 cm^{-1}) window region have been reduced four-fold.

To simulate transmittances for the large values of the solar zenith angle in the solar term, a dedicated fast transmittance model has been developed for the shortwave region by introducing a revised set of predictors. Despite the fact that for the new model the regression coefficients have been obtained from the fit of line-by-line optical depths for a large range of 14 zenith angles, the accuracy of the model is comparable to the accuracy of the standard fast transmittance model used in RTIASI-4 for which regression coefficients have been obtained from the fit of line-by-line optical depths for a limited range of six zenith angles.

Finally, in presence of solar radiation and for a viewing geometry where the surface reflectance of the wind roughened water surface is maximum, transmittance errors result in radiance errors that for the bulk of the channels is typically less than 0.15 K and do not exceed 0.3 K. For the case when less solar radiance is reflected towards the detector (i.e. smaller reflectivity) smaller errors are obtained since the solar term depends linearly on the sun glint ratio.

Acknowledgements

We wish to tank T. Clough, AER, for having provided the software to generate the solar irradiance spectrum, D. Cunnold, Georgia Tech, for having assembled the dataset of MOZART CO profiles and C. Clerbaux, Service D'Aeronomie, for having provided the tropospheric profiles for CH_4. Discussions with T. McNally, J.N. Thépaut and P. Watts, all staff at ECMWF, were also valuable during the course of this work. Marco Matricardi is supported by EUMETSAT (contract EUM/CO/01/882/DK and EUM/CO/02/989/PS) through the IASI pre-launch definition studies.

References:

Apel, J. R., 1994, "An improved model of the ocean surface wave vector spectrum and its effects on radar backscatter", *J. Geophys. Res*., **99**, C8, pp 16269-16291.

Bischof, W., Borchers, R., Fabian, P., and Kruger, B.C., 1985, "Increased concentration and vertical distribution of carbon dioxide in the stratosphere", *Nature*, **316**, pp. 708-710.

Brasseur, G.P., Hauglustaine, S., Walters, S., Rasch, P.J., Müller, J.F., Granier, C., and Tie, X.X., 1998, "MOZART, a global chemical transport model for ozone and related chemical tracers. I. Model description", *J. Geophys. Res.,* **103**, pp 28265-28289.

Cayla, F., 1993, "IASI infrared interferometer for operations and research", in *High Spectral Resolution Infrared Remote Sensing for Earth's Weather and Climate Studies, NATO ASI Series 1*, Ed. A. Chedin, M. Chaine and N. Scott.

Chevallier, F., Chedin, A., Cheruy, N., and Morcrette, J.J., "TIGR-like atmospheric profile database for accurate radiative flux computation", *Q. J. R. Meteorol. Soc*., **126**, pp. 777-785.

Clough, S.A., Kneizys, F.X. and Davis, R.W., 1989, "Line shape and the water continuum", *Atmos. Res.,* **23**, pp. 229-241.

Clerbaux, C., Chazette, P., Hadji_Lazaro, J., Megie, G., Müller, J.-F. and Clough, S.A., 1998, "Remote sensing of CO, CH4 and O3 using a space-borne nadir-viewing interferometer", *J. Geophys. Res*., **103**, pp 18999-19013.

Cox, C. S., and W.H. Munk, 1954, "Measurement of the roughness of the sea surface from photographs of the sun's glitter", *J. Opt. Soc. Am*., **44**, pp. 838-850.

Cunnold, D., Georgia Tech, USA (personal communication, 2001)

Donelan, M. A., and Pierson, W. J., 1987, “ Radar scatter and equilibrium ranges in wind-generated waves with application to scatterometry”, *J. Geophys. Res*., **92**, pp 4971-5029.

Edwards, D.P., 1992, “GENLN2. A general line-by-line atmospheric transmittance and radiance model”, *NCAR Technical note* NCAR/TN-367+STR.

Fleming, H.E. and McMillin, L., 1977, “Atmospheric transmittance of an absorbing gas. 2. A computationally fast and accurate transmittance model for slant paths at different zenith angles”, *Appl. Opt*., **16**, pp. 1366-1370.

GLOBALVIEW-CO2: Cooperative atmospheric data integration project-carbon dioxide. CD-ROM, NOAA/CMDL, Boulder, Colorado. Also available on Internet via anonymous FTP to ftp.cmdl.noaa.gov, path:ccg/CO2/GLOBALVIEW, 1997.

Jackson, F.C., W.T. Walton, D.E. Hines, B.A. Walter, and C.Y. peng, 1992, “Sea surface mean square slope from Kμ-band backscatter data, *J. Geophys. Res*., **97**, pp 11411-11428.

Klaes, K.D., Buhler, Y., Wilson, H., and Wollenweber, F., 2000, “The EUMETSAT Polar System: mission and products”, *Proceedings of the 2000 EUMETSAT Meteorological Satellite Data User’s Conference*, Bologna, Italy, 29 May-2 June 2000.

Kurucz, R.L., 1992, “Synthetic infrared spectra”, in *Infrared Solar Physics, IAU Symposium 154*, edited by D.M. Rabin and J.T. Jefferies, Kluwer, Acad., Norwell, MA.

Hasselman, K., Barnet, T.P., Bouws, E., Carlson, H., Cartwright, D.E., Enke, K., Ewing, J.A., Gienapp, H., Hasselman, P., Kruseman, P., Meerburg, A., Muller, P., Olbers, D.J., Richter, K., Sell, W., and Walden, H., 1973, “Measurements of Wind Wave Growth and Swell Decay during the Joint North Sea Wave Project (JONSWAP) (Deutsches Hydrographisches Institut, Hamburg, Germany).

Marenco, A., Jonquieres, I., Gouget, H., and Nédélec, P., 1995, “ Experimental determination of meridional distribution and long term evolution of tropospheric ozone from large scale airborne campaigna (STRATOZ/TROPOZ) and Pic du Midi data series: Consequences on radiative forcing”, *Global Environmental Change*, edited by W.C. Wang and I.S.A. Isaksen, NATO ASI Ser., 32, pp 305-319.

Masuda, K., Takashima, T., and Takayama, T., 1988, “Emissivity of pure sea waters for the model sea surface in the infrared window regions”, *Remote Sens. Environ*., **24**, pp. 313-329.

Matricardi, M. and Saunders, R., 1999, “Fast radiative transfer model for simulation of infrared atmospheric sounding interferometer radiances”, *Applied Optics*, **38**, pp. 5679-5691.

Mhller, J.-F. and Brasseur, G., 1995, “IMAGES: A three-dimensional chemical transport modelo of the global troposphere”, *J. Geophys. Res*., **100**, pp 16445-16490.

Reber, C.A., Trevathan, C.E., McNeal, R.J., and Luther, M.R., 1993, “The Upper Atmosphere Research Satellite (UARS) Mission”, *J. Geophys. Res*., **98**, D6, pp 10643-10647.

Rizzi, R., Matricardi, M. and Miskolczi, F., 2001, "On the simulation of up-looking and down-looking high-resolution radiance spectra using two different radiative transfer models", Accepted for publication in *Applied Optics.*

Rothman, L.S., Rinsland, C.P., Goldman, A., Massie, S.T., Edwards, D.P., Flaud, J.-M., Perrin, A., Camy-Peyret, C., Dana, V., Mandin, J.-Y., Schroeder, J., McCann, A., Gamache, R.R., Watson, R.B., Yoshino, K., Chance, K.V., Jucks, K.W., Brown, L.R., Nemtchinov, V., and Varanasi, P., 1998, "The HITRAN molecular spectroscopic database and HAWKS (HITRAN Atmospheric Workstation): 1996 edition", *J. Quant. Spectrosc. Radiat. Transfer*, **60**, pp. 665-710.

Shaw, J. A., and J. H. Churnside, 1997, "Scanning-laser glint measurements of sea-surface slope statistics", *Appl. Optics*, **36**, No.18, pp. 4202-4213.

Tjemkes, S.A., Patterson, T., Rizzi, R., Shepard, M.W., Clough, S.A., Matricardi, M., Haigh, J., Hopfner, M., Payan, S., Trotsenko, A., Scott, N., Rayer, P., Taylor, J., Clerbaux, C., Strow, L.L., DeSouza-Machado, S., Tobin, D. and Knuteson, R., 2002, "The ISSWG Line-by-Line Inrecomparison Experiment". Accepted for publication in *J. Quant. Spectrosc. Radiat. Transfer*.

Young, I. R., 1993, "An estimate of the Geosat altimeter wind speed algorithm at high wind speeds", *J. Geophys. Res.,* **98**, pp 20275-20285.

Yoshimory, K., Kazuyoshi, I., and Ichioka, Y., 1994, "Thermal radiative and reflective characteristics of a wind-roughened water surface*", J. Opt. Soc. Am*., **11**, No. 27, pp. 1886-1893.

Yoshimory, K., Kazuyoshi, I., and Ichioka, Y., 1995, "Optical characteristics of a wind roughened water surface: a two dimensional theory", *Applied Optics*, **34**, No. 27, pp. 6236-6247.

Woollard, G.P., 1979, "The new gravity system- changes in international gravity base values and anomalies values", *Geophysics*, **44**, pp. 1352-1366.

Zeisse, C.R., 1995, "Radiance of the ocean horizon", *J. Opt. Soc. Am*. A, **12**, No. 9, pp. 2022-2030.